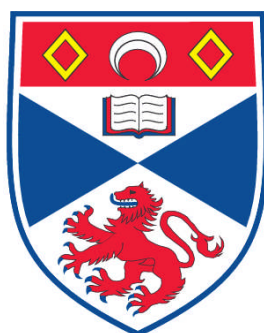


OPTICALLY GUIDED NEURONAL GROWTH

David John Carnegie

**A Thesis Submitted for the Degree of PhD
at the
University of St. Andrews**



2011

**Full metadata for this item is available in
Research@StAndrews:FullText
at:**

<http://research-repository.st-andrews.ac.uk/>

Please use this identifier to cite or link to this item:

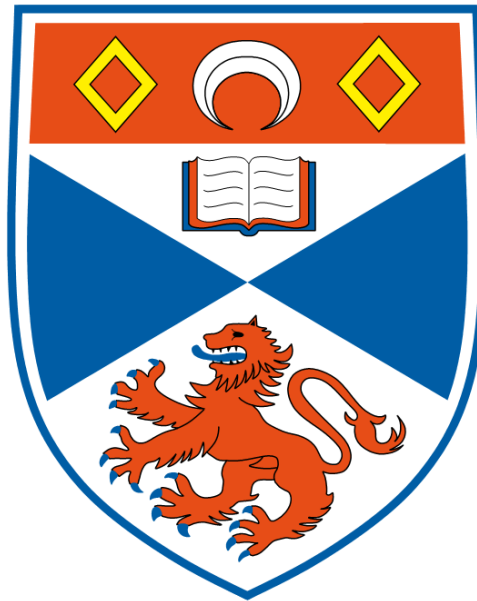
<http://hdl.handle.net/10023/1860>

This item is protected by original copyright

Optically Guided Neuronal Growth

David John Carnegie

A Thesis presented for the degree of
Doctor of Philosophy



Optical Trapping group
Department of Physics and Astronomy
University of St Andrews
UK
September 2010

Declaration

I, David John Carnegie, hereby certify that this thesis, which is approximately 48,000 words in length, has been written by me, that it is the record of work carried out by me and that it has not been submitted in any previous application for a higher degree. I was admitted as a candidate the degree of Doctor of Philosophy in September 2006; the higher study for which this a record was carried out in the University of St Andrews between 2006 and 2010.

Date..... Signature of candidate.....

I hereby certify that the candidate has fulfilled the conditions of the Resolution and Regulations appropriate for the degree of Doctor of Philosophy in the University St Andrews and that the candidate is qualified to submit this thesis in application for that degree.

Date..... Signature of supervisor.....

In submitting this thesis to the University of St Andrews I understand that I am giving permission for it to be made available for use in accordance with the regulations of the University Library for the time being in force, subject to any copyright vested in the work not being affected thereby. I also understand that the title and abstract will be published, and that a copy of the work may be made and supplied to any bona fide library or research worker, that my thesis will be electronically accessible for personal or research use unless exempt by award of an embargo as

requested below, and that the library has the right to migrate my thesis into new electronic forms as required to ensure continued access to the thesis. I have obtained any third-party copyright permissions that may be required in order to allow such access and migration, or have requested the appropriate embargo below.

The following is an agreed request by candidate and supervisor regarding the electronic publication of this thesis: Access to Printed copy and electronic publication of thesis through the University of St Andrews.

Date

Signature of candidate.....

Signature of supervisor.....

Dedicated to

Lara

*"Science is interesting, and if you don't agree you
can fuck off"*

Dr Alun Anderson

Editor in Chief, New Scientist magazine 2003

Acknowledgements

Two people who need to be thank immediately are my two supervisors, Professor Kishan Dholakia and Dr Frank Gunn-Moore. They have both shown extraordinary patience and support throughout my time here at St Andrews and I was very fortunate to have the opportunity to work with them on this project. I greatly appreciate all the hours they spent reading and rereading this thesis and helping me to get it to where it is now.

Were it not for the continuing support of Dr David Stevenson I doubt I would be writing this thesis. He has been a constant source of motivation and has made insightful suggestions at every avenue that took this project in directions no one else thought to go. He was an especially great help when it came to the biological aspects of this project (as well as the whisky aspects of which there were many).

Special mention must also go to Dr Jörg Baumgartl and Dr Tomas Čížmár for their vital support and expertise on spatial light modulators and their contribution to my 2009 publication.

Though I wish to thank everyone who helped me out over the years I would like to specifically mention some people who really stood out. Graham Milne was a great help in the beginning where he showed me how to get the best out of the LabVIEW software that proved vital to this project. Dave Stothard and Dave Walsh from the Terahertz group were both very gracious when it came to exchanges of computer technology and offered vital objective opinions on all the latest software. Special thanks also goes to Rob, Xanthi, Lani, Lissa, Doog, Andrew, Paul, Craig, Chris as well as everyone else in the W-Squad and anyone else whoever helped me on this project. To those of you who were fortunate enough to attend one of the infamous physics bonfire parties, it'll never be the same again.

I must also mention the people that exist outside my academic world which includes a very large and diverse group of friends, too numerous to list, who are now scattered around the globe. To everyone I've ever shared a pint, a dram or a pig with, thank you.

Publications

Peer reviewed publications

D. J. Carnegie, T. Čižmár, J. Baumgartl, F. J. Gunn-Moore and K. Dholakia, “Automated laser guidance of neuronal growth cones using a spatial light modulator,” *J. Biophotonics* **2**, 682-692 (2009).

D. J. Carnegie, D. J. Stevenson, M. Mazilu, F. J. Gunn-Moore, and K. Dholakia, “Guided neuronal growth using optical line traps,” *Opt. Express* **16**, 10507-10517 (2008).

D. J. Stevenson, D. J. Carnegie, B. Agate, F. J. Gunn-Moore and K. Dholakia, “Long-Term Cell Culture on a Microscope Stage: The Carrel Flask Revisited,” *Microscopy and Analysis* **22**(1), 9-11 (2008).

Other publications

D. J. Carnegie, F. J. Gunn-Moore and K. Dholakia, “Optically guided neuronal growth,” SU2P Symposium, University of Strathclyde, March 2010.

D. J. Carnegie, F. J. Gunn-Moore and K. Dholakia, “Optically guided neuronal growth,” Scottish Neuroscience Group, St Andrews, August 2009.

D. J. Carnegie, F. J. Gunn-Moore and K. Dholakia, “Optically guided neuronal growth,” European Conference on Biomedical Optics, Munich, June 2009.

D. J. Carnegie, D. J. Stevenson, F. J. Gunn-Moore and K. Dholakia, “Optically guided neuronal growth,” International School of Biophotonics, Hven, Sweden, July 2007.

D. J. Carnegie, D. J. Stevenson, T.K. Lake, B. Agate, V. Gárcés-Chávez, F. J. Gunn-Moore and K. Dholakia, “Optically guided neuronal growth,” Medical Photonics Workshop, St Andrews, January 2007.

D. J. Carnegie, D. J. Stevenson, T.K. Lake, B. Agate, V. Gárcés-Chávez, F. J. Gunn-Moore and K. Dholakia, “Optically guided neuronal growth at near infrared wavelengths,” Biophotonics: Technology and Applications, Institute of Physics, London, December 2006.

Publicity

“Lasers guide neuron growth,” article on Optics.org, July 2008

Abstract

In this thesis, experiments into artificially guiding neuronal growth cones using tightly focused lasers beams were performed and evaluated.

The experiments are performed by focusing a laser beam to the leading edge of a developing growth cone and attempting to change the direction of growth cone. These experiments were carried out using Gaussian, line and asymmetric line beam profiles. There was no noticeable change in the success rate with different beam profiles.

Following this, I assisted my colleague Dr Michael Mazilu in the construction of a mathematical model of filopodia in an optical field in order to help explain the mechanism for optically guided neuronal growth which suggests that optical trapping forces on filopodia are responsible.

Next, I set about implementing a system to automate the process of laser guided neuron growth by employing a spatial light modulator and a custom built computer program. This allowed the computer to track a developing growth cone and automatically adjust the position of the laser beam as the growth cone developed. This program was successfully employed to artificially grow neuronal growth cones towards a user inputted target point. The use of the spatial light modulator to beam

shape was also demonstrated with the use of a Bessel beam being used to guide neurons for the first time.

I also used a transgenic cell line of neurons to show for the first time that HSP70 is not involved in this phenomenon. This was accomplished by transfecting NG108's with a plasmid containing HSP70 promoter tagged GFP. Under enough thermal or mechanical stress, the cells would express HSP70 which would produce a detectable GFP signal. No GFP was detected in cells after being exposed to laser irradiation of a power higher than would normally be used to guide neurons.

Combined, these experiments show that the beam profile of the operating laser does not significantly affect the success of artificial growth and that the optical force on filopodia near the laser beam is likely to be the mechanism for this phenomenon. A possible heating effect of the laser has also been shown to not be strong enough to illicit a heat shock stress response from the cell. The demonstration of an automatic system which incorporates beam shaping has also been shown and such a system shows the potential to advance the investigation of artificial neuron growth using lasers.

Contents

| | |
|--|-------------|
| Declaration | ii |
| Acknowledgements | vi |
| Publications | viii |
| Abstract | x |
| Abbreviations | xv |
| 1 Introduction | 1 |
| 1.1 Preface | 1 |
| 1.2 Synopsis of thesis | 4 |
| 1.3 Biophotonics | 6 |
| 1.3.1 Optical trapping | 7 |
| 1.3.1.1 Principles | 7 |
| 1.3.1.2 Experimental setup | 13 |
| 1.3.1.3 Notable examples from the literature | 16 |
| 1.3.2 Laser considerations | 19 |
| 1.4 Neurons | 22 |
| 1.4.1 Introduction | 22 |
| 1.4.2 Basic structures | 24 |
| 1.4.2.1 The cytoskeleton | 25 |
| 1.4.2.2 Actin treadmilling | 28 |
| 1.4.2.3 Action potentials | 30 |
| 1.4.3 The growth cone | 34 |
| 1.4.3.1 Introduction | 34 |
| 1.4.4 Growth cone guidance | 37 |
| 1.4.4.1 Chemical cues | 37 |
| 1.4.4.2 Other cues | 43 |
| 1.5 Optically guided neuronal growth | 44 |
| 1.5.1 Discovery and first experiment | 44 |
| 1.5.2 Effect of beam shape | 45 |
| 1.5.3 Effect of wavelength | 47 |

| | | |
|----------|---|------------|
| 1.5.4 | Effect of pulsed operation compared to continuous wave | 50 |
| 2 | Using optical line traps for neuronal growth | 53 |
| 2.1 | Introduction | 53 |
| 2.1.1 | Cell culturing method | 56 |
| 2.1.2 | Experimental setup | 58 |
| 2.2 | Experimental procedure and results | 61 |
| 2.2.1 | Explanation of ‘Forward’ and ‘Reverse’ bias configurations | 62 |
| 2.2.2 | Description of laser application | 64 |
| 2.2.3 | Results | 66 |
| 2.3 | Mathematical model | 69 |
| 2.3.1 | The original approach by Ehrlicher et al | 70 |
| 2.3.2 | My filopodial approach | 72 |
| 2.4 | Conclusion and discussion | 81 |
| 3 | Development of an automated experimental setup | 84 |
| 3.1 | Introduction | 84 |
| 3.2 | Spatial Light Modulators | 85 |
| 3.2.1 | Introduction to Spatial Light Modulators | 85 |
| 3.2.2 | Fourier optics and Spatial Light Modulators | 86 |
| 3.2.3 | Principle of operation | 90 |
| 3.2.4 | Beam aberration correction using SLMs | 94 |
| 3.2.5 | Comparison to Acousto-Optic Deflectors | 95 |
| 3.3 | Spatial Light Modulators for neuron growth | 97 |
| 3.3.1 | Optical train | 97 |
| 3.3.2 | Introduction to LabVIEW | 100 |
| 3.3.3 | Shape detection using LabVIEW | 101 |
| 3.3.4 | Application of program | 108 |
| 3.4 | Conclusion | 117 |
| 4 | Investigations into the biochemistry of optically guided neuronal growth | 119 |
| 4.1 | Introduction | 119 |
| 4.2 | HSP-70 as an indicator for laser induced cell stress | 121 |
| 4.2.1 | Introduction | 121 |
| 4.2.2 | Plasmid construction | 122 |
| 4.2.2.1 | Heat Shock Protein | 122 |
| 4.2.2.2 | Green fluorescent protein | 125 |
| 4.2.2.3 | HSP70-GFP | 128 |
| 4.2.2.4 | Plasmid construction and transfection | 130 |
| 4.2.3 | Experimental procedure | 132 |
| 4.2.3.1 | Controls | 132 |
| 4.2.3.2 | Main experiment | 134 |
| 4.2.4 | Results | 135 |

| | | |
|----------|---|------------|
| 4.2.5 | Conclusion and discussion of heat shock experiments | 139 |
| 4.3 | Chemical pathway inhibition | 140 |
| 4.3.1 | Introduction | 140 |
| 4.3.2 | Introduction to chemical pathways | 142 |
| 4.3.2.1 | The mitogen-activated protein kinases | 142 |
| 4.3.2.2 | Phosphatidylinositol 3-kinases | 144 |
| 4.3.3 | Inhibitors used | 147 |
| 4.3.3.1 | UO126 | 147 |
| 4.3.3.2 | LY294002 | 148 |
| 4.3.4 | Experimental procedure and results | 149 |
| 4.3.4.1 | Results | 152 |
| 4.3.5 | Conclusion and discussion of protein inhibition experiments | 156 |
| 5 | Conclusions and discussion | 159 |
| | Bibliography | 166 |
| | Appendix | 185 |
| 5.1 | Appendix 1: Data in Table 2.1 | 185 |
| 5.2 | Appendix 2: Mathematica code | 186 |

Abbreviations

ADP - Adenosine Diphosphate

AOD - Acousto-Optic Deflector

ARP - Actin Related Protein

ATP - Adenosine Triphosphate

BAEC - Bovine Aortic Endothelial Cell

BFP - Blue Fluorescent Protein

CAM - Cell Adhesion Molecule

CCD - Charge Coupled Device

CDC42 - Cell Division Control Protein 42

CHO - Chinese Hamster Ovary

CO₂ - Carbon Dioxide

COM - Centre of Mass

CRT - Cathode Ray Tube

CW - Continuous Wave

DCC - Deleted in Colorectal Carcinoma

DIC - Differential Interference Contrast

DMEM - Dulbecco's Modified Eagle Medium

DMSO - Dimethylsulphoxide

DNA - Deoxyribonucleic Acid

DRG - Dorsal Root Ganglia

EGFP - Enhanced Green Fluorescent Protein

EM - Electromagnetic

ER - Endoplasmic Reticulum

ERK - Extracellular Signal-Regulated Kinase

FACS - Fluorescence-Activate Cell Sorting

FCS - Foetal Calf Serum

FGF - Fibroblast Growth Factor

FITC - Fluorescein Isothiocyanate

FRET - Förster Resonance Energy Transfer

FT - Fourier Transform

GFP - Green Fluorescent Protein

HASMC - Human Aortic Smooth Muscle Cell

HOT - Holographic Optical Tweezers

HSE - Heat Shock Promoter Element

HSF - Heat Shock Factor

HSP - Heat Shock Protein

HSP70 - Heat Shock Protein 70

HSPB1 - Heat Shock Protein Binding Factor 1

IR - Infrared

LC - Liquid Crystal

LCD - Liquid Crystal Display

MAPK - Mitogen-Activated Protein Kinase

MEK1 - Mitogen-Activated Protein Kinase Kinase

MT - Microtubule

NA - Numerical Aperture

Nd:YAG - Neodymium-doped Yttrium Aluminium Garnet

NGF - Nerve Growth Factor

NIR - Near Infrared

NRK - Normal Rat Kidney

N-WASP - Neural Wiskott-Aldrich Syndrome Protein

PAK - p21 Protein-Activated Kinase

PC - Personal Computer

PI3K - Phosphoinositide 3-Kinase

QPD - Quadrant Photodiode

RAC - Ras-Related C3 Botulinum Toxin Substrate

ROI - Region of Interest

RNA - Ribonucleic Acid

SAM - Surface Adhesion Molecule

SLM - Spatial Light Modulator

SPM - Single Point Mutation

Ti:Sapph - Titanium-doped Sapphire

TP - Target Point

UNC5 - Uncoordinated Locomotion-5

UV - Ultra Violet

VI - Virtual Instrument

Chapter 1

Introduction

1.1 Preface

When Albert Einstein published *Zur Quantentheorie der Strahlung* in 1917 [1], he set physicists on a quest to develop a source of coherent monochromatic light that is now theoretically possible thanks to his work. However, it was not until over 40 years later that the first laser was demonstrated to the world by Theodore Maiman in 1960 [2].

Originally, the laser was almost ridiculed as a “solution looking for a problem” but since then several entirely new fields of physics have emerged based around the laser and exploiting it for scientific and technological gain. In the beginning of the 21st century the laser is now ubiquitous and there is almost no aspect of industry that has not been touched by it. Telecommunications, spectroscopy, defence, computing and medicine have all been through massive revolutions in the last 50 years because of this new device.

Another one of the great technological innovations from an understanding of Einstein's quantum theory of light was the invention of 'optical tweezers' in 1986 by Arthur Ashkin [3]. Using a focused laser beam it is possible to transfer sufficient amounts of momentum from the photons to small particles to confine them spatially in three dimensions. Ashkin immediately saw the biological potential of such an invention and the following year published a paper describing the optical trapping and manipulation of viruses and bacteria [4]. However, for this work he used an Argon laser operating at 514 nm which is a wavelength that is harmful for cells and so, later in the same year, Ashkin published another paper again showing the trapping and manipulation of cells but using a Nd:YAG laser of wavelength 1064 nm which is less harmful to biological cells [5].

A direct offshoot of the field of photonics, Biophotonics is concerned with biological applications of photonic devices. The term now includes all areas of research investigating the interaction between biological materials and photons. Most of the research in this field has been confined to the ultra-violet, visible and infra-red regions of the electromagnetic spectrum because of the availability of laser sources in those regions.

Examples of research in Biophotonics includes fluorescent cellular microscopy, laser assisted nanosurgery, optical transfection and optical manipulation of cells. In this thesis I will discuss my experiments into optically guided neuronal growth which can be considered a form of optical manipulation. Optically guided neuronal growth is the term for the discovery that a focused laser beam can influence the growth of

a developing neurite and can manipulate the direction of their growth.

The study into artificial neuron growth is important because of the many diseases and afflictions in humans that are attributed to damaged neuronal circuitry. Some fish have the ability to regenerate their spinal neurons and regain motor control of their limbs after trauma which would leave a mammal otherwise paralyzed [6], so the repair of spinal tissue is at least possible and has been demonstrated in nature. Any technology which can artificially grow neuronal structures has the possibility of becoming the basis for a treatment into diseases and ailments which are specifically caused by neuronal growth problems. An additional benefit of using optical methods for this is the sterility that comes with a non-contact technique. No physical contact is needed and so any procedure is intrinsically sterile which is an important consideration in practical medicine.

There is also keen interest in the possibility of building circuits and logic gates using neurons [7]. Any technique that could manipulate the circuitry of neurons could therefore be of use in this endeavor

Though more extensive research will be needed before any of the experiments discussed in this thesis could lead to practical medical or technological fruits, the growing interdisciplinary collaborations between physicists and biologists ensure that this research will continue.

1.2 Synopsis of thesis

This thesis is constituted of five chapters. This first chapter is written as a brief introduction to the field of Biophotonics and specifically to optically guided neuronal growth. Covered in this chapter will be examples of Biophotonics research and its importance as well as the background science necessary to understand my experiments into guiding neurons with light. The brief history of experiments by other research groups into this phenomenon will also be covered.

Chapter 2 is the first experimental chapter and will deal with my experiments into the effect different beam profiles have on artificial neuronal growth. I will detail my experimental setup that was used to create the Gaussian and line beams that were employed as well as discuss the results of these experiments. I will also describe the mathematical model I assisted in building with my colleague Dr Michael Mazilu using Mathematica 5.2 (Wolfram). This model builds on previous work by Ehrlicher et al and I will discuss the importance it has to my observations. The implications of these results with regard to some of the other literature on optically guided neuronal growth, will also be discussed.

In Chapter 3, I describe a series of experiments and developments that led to the creation of an automated system for optically guided neuronal growth. This will involve a discussion on the principles of the spatial light modulator (SLM) as well as a brief review of its use throughout the Biophotonics literature. I will also go into a detailed description of the LabVIEW (National Instruments) program that was written for this purpose including specifics on how images are processed to

extract edge information for real time tracking. Finally, within the this chapter, I will show the results demonstrating that this system works and also show how the beam shaping capabilities of the SLM mean that this system could form the ideal platform for a more in depth and comprehensive study into this phenomenon.

Chapter 4 is the final experimental chapter and deals with my investigations into the biochemistry of laser guided neuron growth. This chapter is split into two sections, one investigating the possibility of laser induced thermal effects using HSP70 promoter GFP tagged transgenic cell lines and the other detailing experiments into chemical pathway inhibition. Previous work on laser induced thermal stress in cells has shown that HSP70 can be up regulated, but there are also examples in the literature that show that the thermal effects experienced by neurons during a typical laser guided neuron growth experiment are marginal. My experiments set out to determine if the laser radiation used in these experiments is indeed activating a heat shock response in these cells which could plausibly explain why they react to focused laser light. This section will include some specific background details on HSP70 and GFP as well as some examples of their use in the literature. Cellular responses to stimuli are governed by complex biochemical pathways and it is plausible that a laser beam as used for neuron growth experiments could be interfering with this machinery and be responsible for the neurons response to focused laser light. In order to test this hypothesis I reviewed the literature on chemical pathway inhibition in neuronal growth cones and chose to inhibit two key proteins (separately) to see if optically guided neuronal growth was still possible under these conditions. The

proteins chosen for inhibition were mitogen activated protein kinase kinase (MEK1) and phosphatidylinositol-3 kinase (PI3K) which have been shown in the literature to be vital for viability of growth cones in neuronal cells. With these proteins inhibited, growth cones in the NG-108 cell line were adversely affected and even collapsed, despite the presence of a laser beam used for artificial growth. This suggests that these pathways are a pre-requisite for optically guided neuronal growth and that the laser does not sufficiently affect the biochemistry of the cell to affect its response to certain chemical inhibitors.

1.3 Biophotonics

For the purposes of understanding this thesis it will be useful to review the background science on optical trapping and neuronal growth without which my experiments would not be possible.

Biophotonics is a combination of words biology and photonics and has become a general term used to describe experiments and technology that deal with the interaction of photons and biological matter. The field of Biophotonics is very diverse and includes technologies and techniques such as photoporation, optical cell sorting, nanoparticle injection, optical coherence tomography, photo dynamic therapy and diffuse optical tomography. A complete review of Biophotonics is beyond the scope of this thesis and the examples listed are only to give an idea of the size and diversity of the field.

As already mentioned, the invention of the laser spurred a revolution in many

branches of science including medicine and biology. The invention of the optical tweezers further cemented the demonstrably important role physics could play in the biology lab. Discussed here is the basic principles behind the optical tweezers and some notable examples of its use from the literature as well a mention of the various laser sources used in these applications. Also discussed are some recent advances in the field of Biophotonics including photoporation, optical cell sorting and nanoparticle injection systems.

1.3.1 Optical trapping

1.3.1.1 Principles

The fundamental principle behind optical tweezers is the ability of light to carry and transfer momentum. Planck hypothesized in 1901 that the energy of any system that absorbs or emits light of frequency ν must do so in discrete energy levels of $E = h\nu$ [8]. In 1905 Einstein showed Planck's hypothesis to be correct experimentally and that light does act as a particle [9].

The photon, later shown to be an elementary particle, was capable of transferring discrete amounts of energy as well as, because of mass-energy equivalence, discrete amounts of momentum between absorbing targets. The momentum carried by a photon is related to its frequency and is given by the formula $p = h\nu/c$. So a particle that absorbs a photon will experience a change in momentum due to the conservation of momentum. For example, a photon of wavelength $\lambda = 1064$ nm will have a momentum equal to $6.231 \times 10^{-28} \text{ kg m s}^{-1}$. If one wished to use a stream

of these photons to exert a constant force of 1 newton on an absorbing object then one would need 1.605×10^{27} of these photons transferring their momentum every second which would be equivalent to a power of ~ 300 MW. What this means is that it would be impractical to use the momentum of photons to exert macroscopic forces, but for a microscopic object which weighs on the order of picograms then only a force of $F = mg \simeq 10^{-11}$ N would be required to counteract the weight of this particle, which is equivalent to a photon power of ~ 3 mW.

Ashkin was the first to show that this radiation pressure could be used to accelerate and confine microscopic particles in 1970 [10]. He observed that one laser could accelerate particles along its optical axis and then showed that two directly opposing beams could confine the particles (i.e. the radiation pressure from each was balanced in the middle). It was another 16 years before he demonstrated the first single beam optical tweezers [3] which is only made possible by what was termed ‘negative’ radiation pressure. In the Mie regime (where particle size is \gg the wavelength of the laser light) a ray optics approximation, shown in Figure 1.1, is sufficient to describe the optical forces.

More precisely, the forces in the Mie regime due to the optical gradient and the scattering can be described by equations 1.1 and 1.2 respectively [11].

$$F_{grad} = \frac{nP}{c} \left(R \sin 2\theta + \frac{T^2[\sin(2\theta - 2\phi) + R \sin 2\theta]}{1 + R^2 + 2R \sin 2\phi} \right) \quad (1.1)$$

$$F_{scat} = \frac{nP}{c} \left(1 + R \cos 2\theta + \frac{T^2[\cos(2\theta - 2\phi) + R \cos 2\theta]}{1 + R^2 + 2R \sin 2\phi} \right) \quad (1.2)$$

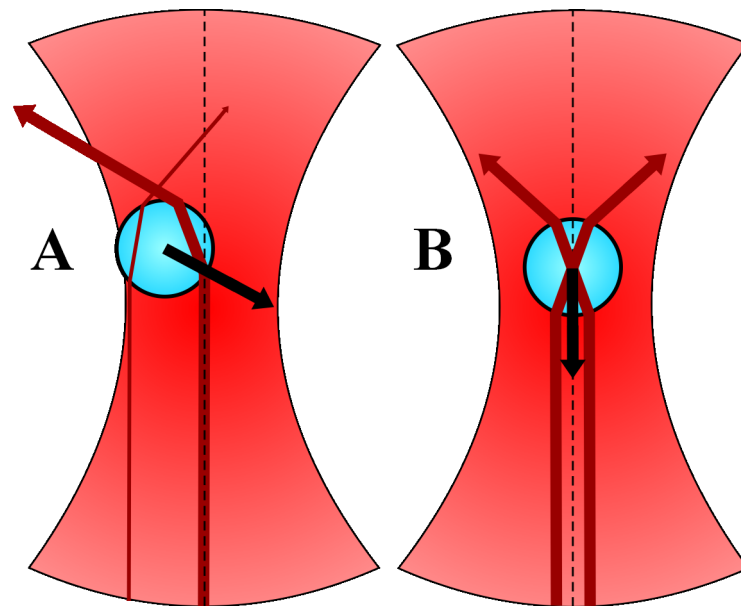


Figure 1.1: Diagram showing how ray optics can explain 3D particle trapping in the Mie regime due to a single laser beam. A focused laser beam (propagating upwards) is incident on a particle of high refractive index. In (A) the particle is slightly off-centre and two ray traces from the laser are shown propagating through the particle and refracting as they do (red arrows). The thicker line represents a larger force/intensity and the resultant force in (A) due to these forces (black arrow) is towards the centre of the beam. In (B) the particle has now moved to the centre of the beam where the lateral forces are now balanced. The resultant force this time is down towards the laser beam and where this force is balanced by the scattering force (not shown) due to some photons reflecting off the particle, is where the particle will be confined. The optical trap forms a potential well.

where n is the refractive index of the surrounding medium, θ is the angle of incidence of the photon upon the particle, ϕ is the angle of refraction, R is the reflection coefficient, T is the transmission coefficient, P is the incident power and c is the speed of light. In order for axial trapping, F_{grad} must be greater than F_{scat} . These equations are essentially derived from the geometry of the ray optics and the particle as shown by Ashkin in 1992 [11]. It is interesting to note that these equations do not depend upon the radius of the particle, however this is because the equations are neglecting the force due to gravity and the Brownian motion due to thermal energy. Since mass (and thus the force due to gravity) varies as the cube of the radius, larger particles become harder to trap and, conversely, since Brownian motion varies inversely as the cube of the radius, smaller particles find it easier to escape optical potential wells. Between these two extremes is a window of size (from about 18 nm to hundreds of microns) where optical tweezing forces dominate which fortunately falls into the size range of cellular and molecular biology.

For situations where the particle size is much larger than the wavelength (Mie regime) of the photon, the ray optics model of photons refracting through the particle and imparting momentum is perfectly adequate but this model breaks down for situations where the particle size is much less than the incident wavelength (Rayleigh regime). In this situation we can no longer consider photons travelling through the object and must instead model the system based on the electric field of the laser beam and the dielectric properties of the particle. In the presence of an electric field, a dipole will be induced on a dielectric particle which will act to oppose the electric

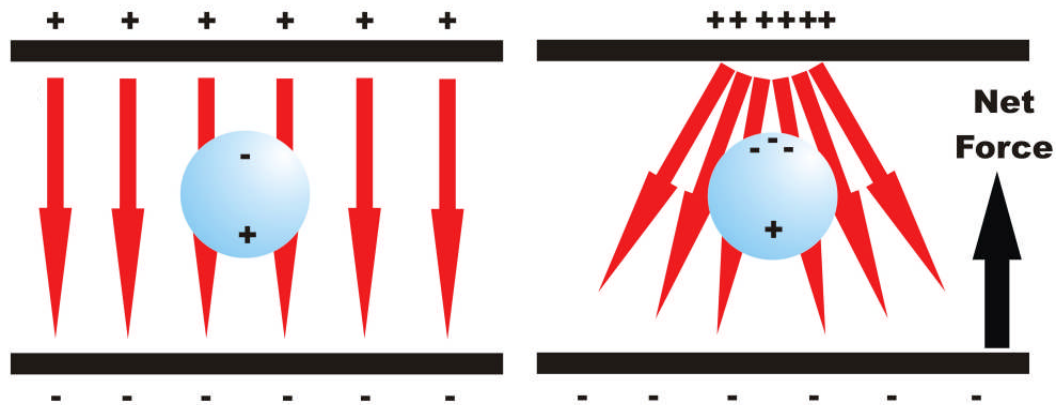


Figure 1.2: Diagram of a dielectric particle in an electric field. On the left the field is uniform and there is no net force on the particle. On the right, there is a field gradient which leads to a charge imbalance on the particle which results in a net force towards the most intense region of the electric field. Image reproduced from [12].

field. If this field is uniform then there is no net force, but if the electric field has a gradient, then there is a charge imbalance which leads to a net force towards the most intense region of the electric field (i.e. the beam centre). Shown in Figure 1.2 is a diagram to illustrate this.

As in the Mie regime, there is also a scattering force that counters the gradient force in the Rayleigh regime. Whereas the scattering force in the Mie regime was attributed to the absorption and re-emission of light (reflection) imparting momentum on the particle, in the Rayleigh regime, the scattering force can be attributed to the absorption and re-emission of light *by the dipole* induced in the particle.

The gradient force on a dielectric particle in an electric field can be shown to be described by equation 1.3 [3, 13, 14] and the scattering force by equation 1.4 [3, 14]

$$F_{grad}(r) = \frac{1}{2}n\alpha\nabla I(r) \quad (1.3)$$

$$F_{scat}(r) = \frac{8\pi^4}{3\lambda^4\varepsilon^2n^3c}\alpha^2I(r) \quad (1.4)$$

where $I(r)$ is the incident intensity, λ is the wavelength of the incident light, ε is the permittivity of the particle and α is the polarisability of the particle given by the Clausius-Mossotti equation

$$\alpha = 4\pi\varepsilon a^3n^2\left(\frac{m^2-1}{m^2+2}\right) \quad (1.5)$$

where n is the refractive index of the surrounding medium, a is the radius of the particle and m is the effective refractive index which is the ratio of the refractive index of the particle to that of the surrounding medium. Notably there is a dependency on the radius of the particle in F_{grad} which implies that larger particles are easier to trap than smaller ones. However, since F_{scat} also varies as the radius (but to the power of 6 due to the dependence on α^2 which itself depends on a^3) then the scattering forces increase faster than the gradient forces and large particles actually become harder to trap at large radii (of course this model breaks down at particle sizes of $r \gg \lambda$). In addition to F_{grad} being greater than F_{scat} for trapping, we must also consider the significant Brownian motion of particles in this size regime. In order to trap a particle successfully we need the potential due to the optical force at the beam centre to be larger than the thermal energy $k_B T$ of the particle so that the Boltzmann factor $\exp[-U(r)/k_B T]$ is less than 1 where $U(r) = \frac{1}{2}n\alpha E(r)^2$ is the potential of the gradient force (which is derived by integrating Equation 1.3 over r). A factor of $U \geq 10k_B T$ at the trap centre is ideal for good trapping [3]. As particle

size decreases, so does the polarisability and thus the trapping potential due to the optical force, to date the smallest particle successfully trapped by a single laser beam has been a gold nanoparticle of radius 18 nm but this required a huge laser power (>800 mW) and the trap was not stable over periods longer than a minute [15].

The computational mathematics of modelling Rayleigh particles in an optical field has spurred a considerable amount of research in and of itself [3, 13, 14, 16, 17] and the results of this research will be applied later in Chapter 2 to help model the behaviour of cytosolic actin in the presence of an optical field.

However, when the dimensions of the trapping particle are on the same scale as the wavelength of the laser (roughly $0.1\lambda - 10\lambda$), it is in an intermediate range between the Rayleigh and Mie regimes. For particles in this range neither the ray optic or dipole approach is valid and a much more rigorous development of electromagnetic (EM) theory must be used. Several of these concepts have been extended to arbitrary shapes such as spheroids and are referred to as ‘generalized Lorenz–Mie theories’ [18–22]. In practice, particles in this regime are still readily trapped.

1.3.1.2 Experimental setup

Fundamentally, all that is needed to construct optical tweezers is a laser beam and a high quality microscope objective to focus the beam down to a sufficiently small spot. Shown in Figure 1.3 is an example of a typical optical tweezers setup incorporated into an experimental microscope.

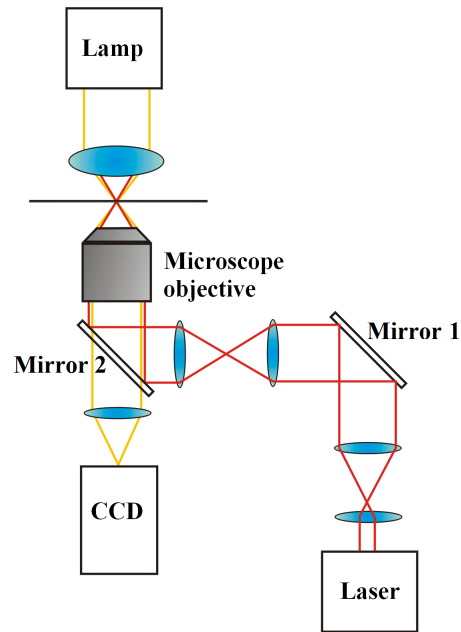


Figure 1.3: *Simplified diagram of a generic optical tweezers setup. Essentially it is a microscope that has a laser beam ported into the back aperture of the objective which focuses the laser down to a microscopic spot in the sample plane. The laser beam is first expanded to the same width as the back aperture by a two lens system and then image on to the back aperture by another two lens system. Mirror 1 can be used as a steering mirror. Mirror 2 is a dichroic which reflects the wavelength of the laser light but transmits at other wavelengths allowing the CCD to capture images. Without the laser this system would operate exactly as a standard transmission microscope with a lamp providing illumination through a condensing lens before being captured by the objective lens and transmitted to a CCD (or eyepiece).*

Typically a laser operating in the TEM_{00} mode will be collimated and passed through a two lens system to increase its beam width to match that of the back aperture of the microscope objective, such as the lenses immediately after the AODs in Figure 1.3. The filling of the back aperture is necessary to obtain a diffraction limited beam waist at the focus, an under filled aperture will result in a large beam waist and thus a reduced axial trapping power, whereas an overfilled aperture will result in loss of power [23]. After being expanded by this lens system the beam is usually imaged through another two lens system such that the final lens is one focal length away from the objective. This produces a conjugate plane with the back

aperture of the microscope, which means if a steering mirror is placed here, then spatial translation in the focal plane is possible without altering the flux through the back aperture. A graphical explanation of this is shown in Figure 1.4.

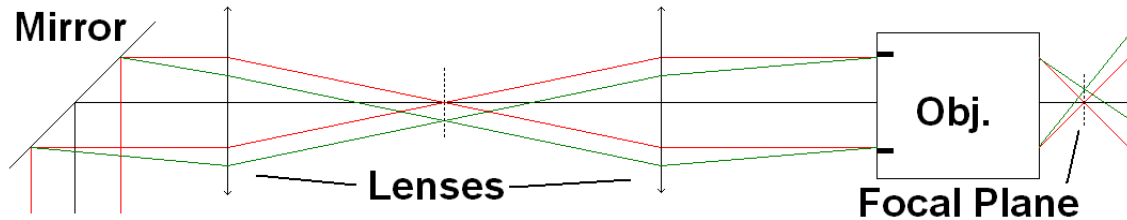


Figure 1.4: *Illustration of the operation of a steering placed at the conjugate plane of the microscope back aperture. The red lines represent an unsteered beam first being reflected off the mirror (far left) and then travelling left to right through the lens system and finally to a focus after passing through the objective (far right). The dashed lines indicate focal planes and the black line running down the centre is the optical axis. The green lines show a possible path for the beam if the mirror had been rotated slightly. Notice how it focuses in the same plane but at a different point from the unsteered beam and how the flux through the back aperture remains unchanged.*

This steering mirror can be fitted with a piezoelectric device or a galvanometer so that it can be rotated automatically allowing precise control of the beam location at focus. Alternatively, the mirror can be replaced with a reflecting spatial light modulator (SLM) to allow much more precise beam control and complex shaping options. These devices are becoming much more common in optical setups and I will elaborate more on their operation in Chapter 3.

Optical tweezers, such as those described here, can be said to form the basis of the ever expanding ‘optical toolkit’. This toolkit includes optical equivalents for most household tools such as optical scissors (used to cut molecules) [24], optical stretchers (used to mechanically deform cells) [25], optical spanners (used to impart torque) [26], optical sieves (used to filter cells based on size) [27] and an optical hammer (used to inject gold particles into cells) [28].

1.3.1.3 Notable examples from the literature

As previously mentioned, research in this field has been ongoing since Ashkin's original work in 1986 and it would not be unfair to say that most of the applied work has come from using the optical tweezers to study biological processes.

At the molecular scale, a great example of such work is that of Svoboda et al who in 1993 used optical tweezers to measure the individual 8 nm steps taken by the kinesin molecule [29]. This was made possible by the attachment of optically tweezable silica beads, carrying single molecules of kinesin, and then depositing these beads onto microtubules.

Kinesins are a class of motor proteins found in eukaryotic cells that travel along the cytoskeletal microtubules and can transport other cytosolic proteins around the cell. The nature of the molecule (shown in Figure 1.5) suggested that it moves along the microtubule in discrete steps [30]. To do the experiment, Svoboda et al placed kinesin coated silica beads into a solution containing ATP and microtubules (microtubules are visible under DIC microscopy). They then trapped a bead and positioned it over a microtubule and, using a technique known as optical trapping interferometry, were able to measure minute but discrete changes in the displacement of the bead from the centre of the trap. These displacements could only have been due to the kinesin molecule trying to pull the bead along the microtubule and so they could observe the individual 8 nm steps that the kinesin was making along the microtubule.

Optical trapping interferometry works by having the trapping beam split into

two beams of orthogonal linear polarisation states. These beams are both focussed through the objective down to overlapping diffraction limited spots laterally separated by ~ 250 nm but functioning together as a single optical trap. The bead introduces a relative retardation between the two polarisation states and so when the beams are recombined by the condenser they interfere and create an elliptical polarisation state. This elliptical polarisation state is separated by a quarter wave plate back into two orthogonal linear polarisation states. The difference in intensity between these two beams is detected by two photodiodes and a normalising differential amplifier. If the bead is exactly between the two traps then the relative intensity will be zero, however, if the bead is slightly displaced from this point then an intensity difference can be detected and for small distances (< 150 nm) this difference scales linearly with displacement. Because the same beam is also trapping the bead, then a restoring force will be felt by the bead when it moves out of the beam centre. For small displacements this force scales linearly with displacement. So, with trapping power known, and the displacement of the bead from the trap measurable, it becomes possible to measure any force that is acting to move the bead from the trap centre. In the experiment described, this force comes from the kinesin molecule trying to move the bead along a microtubule.

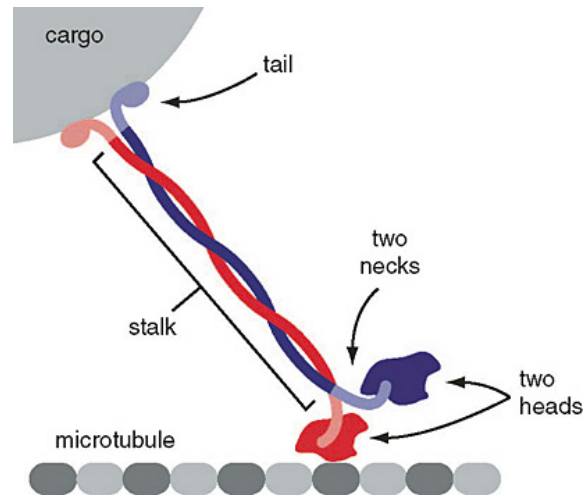


Figure 1.5: Diagram of a kinesin molecule carrying cargo along a microtubule. The kinesin itself is composed of two chains (red and blue) the heads of which are alternatively switched 'on' and 'off' by converting ATP to ADP and vice versa. When 'on' the head is attached to microtubule and the structure of the molecule is such that the off head will be in front where by it will be switched 'on' and attach to the microtubule at which point the rear head will switch 'off' and detach and move ahead to the next step and the process begins again. This implies that the kinesin will move along the microtubule in small discrete steps. Image reproduced from [31]

So by measuring the displacement using photodiodes it becomes possible to also determine the accompanying restoring force. In a similar experiment in 1995 the same researchers were able to measure the force exerted by a single molecule of *Escherichia coli* RNA polymerase during transcription (14 piconewtons) [32]. Ten years later, the same group then did the experiment again and were able to measure the individual steps the RNA polymerase took as it moved along the DNA it was translating. The step size they measured was 0.37 ± 0.06 nm, a distance which they note is comparable to a single base pair [33].

In 2000, Wuite et al measured the force required to stretch both double stranded DNA (dsDNA) and single stranded DNA (ssDNA). Using two beads linked together by the DNA, with one bead held stationary in a pipette and the other in a force measuring optical trap, they could slowly stretch the two beads apart and measure

the force required to achieve this. It was shown that ~ 6 pN of tension is enough to stretch dsDNA and ssDNA to double their lengths [34,35]. A similar experiment in 2006 by Matsumoto and Olson attempted to measure the twisting modulus of DNA [36].

Optical tweezers have also found application at the cellular scale. Indeed it was Ashkin who first used optical tweezers to trap and move bacteria and viruses in 1987 [4]. Optical tweezers have also been used to study sperm motility in primates [37,38]. By using a trapping laser of known force König et al were able to accurately determine the swimming force of the sperm [37] and Nascimento et al then used the same technique to quantify the motility of sperm and compare it to the ‘speed of progression’ (SOP) score, which is a commonly used measure of fertility in medicine, determined by sperm motility experts. They found that the forces measured by optical trapping provided valuable quantitative information to assess sperm motility [38]. The ability of optical tweezers to move cells is also being applied to the field of *in vitro* fertilisation [39, 40].

1.3.2 Laser considerations

The practical wavelength range of commercially available laser sources covers roughly 157 nm (F_2 excimer laser, pulsed) to about 10.6 μm (CO_2 gas laser, cw), though some molecular gas lasers have been demonstrated to operate at up to 699 μm [41].

For optical tweezing and related biological applications, visible light wavelengths are convenient to use because existing optics (such as high N.A. microscope objec-

tives) are designed to work in this range. Although recently, some manufacturers have begun to make objectives which are designed to operate efficiently at UV and NIR wavelengths (e.g. the Nikon UV 100x Objective which can operate achromatically down to 248 nm).

For biologically specific applications, it is also important to consider the potential harm caused by the wavelength (and not just power) of the laser. A good example is that of DNA which is very sensitive to photodamage from UV light (peaks at 260 nm). When UV light is incident on the molecule it causes cross-linking between adjacent cytosine and thymine bases creating pyrimidine dimers (as well as creating free radicals) [42]. Pyrimidine dimers are mutagenic and are the primary cause of skin cancer in humans [43].

Ashkin himself was aware of this when he published his first work on trapping bacteria [4]. In that work he used an Argon laser of wavelength 514 nm which he noted was very effective at killing the bacteria he was attempting to trap (which led him to coin the term “optocution”). He then published a similar experiment in the same year trapping bacteria with the much less harmful NIR wavelength of a neodymium-doped yttrium aluminium garnet (Nd:YAG) laser at 1064 nm and demonstrated the ability to trap and manipulate them without killing them [5]. Why this wavelength is less damaging than 514 nm is because cells and bacteria are comparatively more transparent in the NIR range, which in turn is because many biological chromophores absorb strongly in the visible region but not in the NIR region. However, there is only a small window here because water begins to

absorb strongly at increasing IR wavelengths [44].

This has led to the NIR being one of the most commonly used wavelength for optical trapping. Diode laser sources have also recently begun to be used extensively because of their cheap cost and high output powers. The mode-locked widely tunable titanium-doped sapphire (Ti:sapphire) laser (which can tune over a range ~ 700 -1050 nm) is also a commonly used laser in optical tweezing setups, especially in research and applications that are wavelength dependent and/or require a pulsed operation.

Despite being the most commonly used wavelength range for optical trapping, certain wavelengths of NIR can also be harmful. For example, a study by Neuman et al in 1999 attempted to measure the photodamage caused to *Escherichia coli* over the wavelength range of 780-970 nm using a tunable Ti:sapphire laser [45]. They found that photodamage is minimised at 830 and 970 nm but reaches a maximum at 870 and 930 nm. This result agrees quite well with a previous study done on Chinese hamster ovary (CHO-K1) cells over the same wavelength range suggesting it is a general trend not specific to any one lifeform. [46].

Other plausible mechanisms for why some wavelengths are more toxic than others include localised heating [47] and multiphoton absorption [48, 49].

Localised heating will occur to a degree for all powers and wavelengths. Where there are absorption peaks, for example in the spectrum of water, then there will be a higher degree of heating. Heating can of course be harmful to cells and this will be explored further in Chapter 4.

Multiphoton absorption is when two or more photons arrive at the same time

and are essentially absorbed as one photon equal to half the wavelength (double the frequency) of the incident photons. The chances of two or more photons arriving at the same time is increased by a higher photon density (i.e. beam power) and can be a particular problem (or benefit depending on the context) for pulsed lasers. For example, a mode-locked Ti:sapphire can operate over a range of ~ 700 - 1050 nm which corresponds to two and three photon absorption wavelengths in the visible and UV regions respectively which covers the UV range where photodamage is typically higher than that of visible and NIR wavelengths.

Biophotonics is a continuously growing field of science and its technologies are important tools in single cell analysis and surgery as well as complex molecular biology studies. With the ever decreasing costs and increasing quality of lasers, the potential applications and technologies developed from Biophotonics is set to increase.

1.4 Neurons

1.4.1 Introduction

Cells have already been mentioned in this thesis but without any explanation of exactly what they are or how they operate and it will be useful to briefly cover an introduction to the basic biology here.

All known cell types share some basic features: they are all protected by a phospholipid membrane and they all contain DNA and the necessary machinery to replicate and translate it. Figure 1.6 is a diagram of the basic structure of a typical

eukaryotic cell.

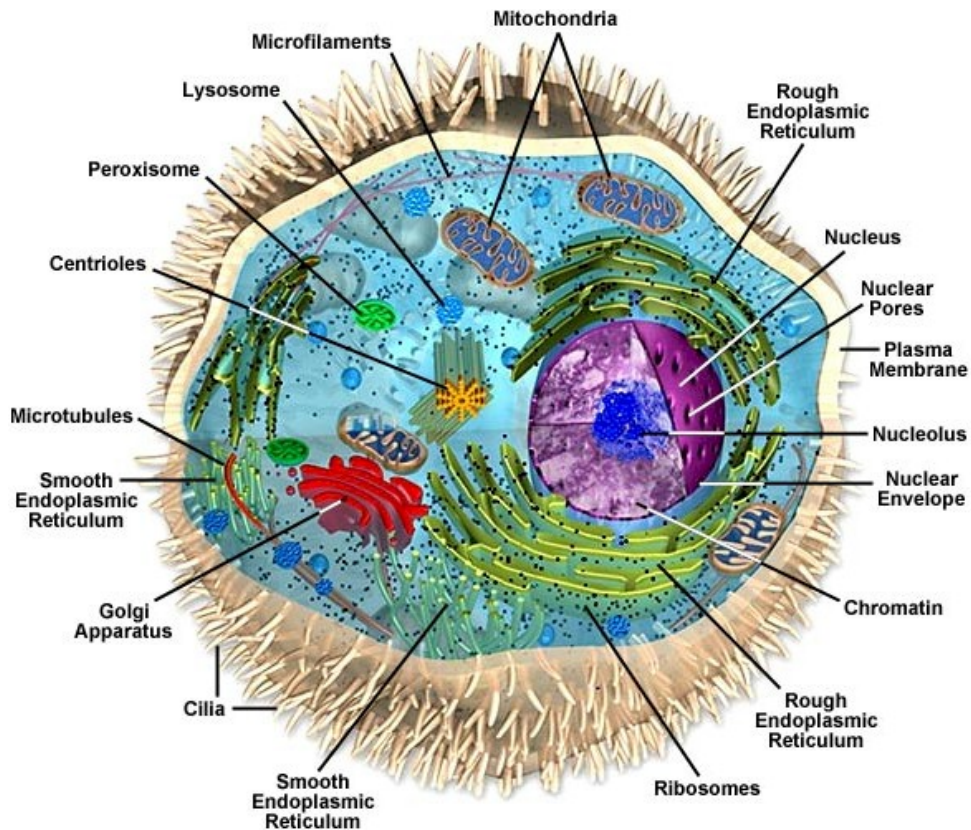


Figure 1.6: *Diagram of a typical eukaryotic cell. Notable structures are the plasma membrane protecting the cell from the exterior world, the nucleus that contains the DNA of the cell and the organelles such as mitochondria which provide energy for the cell. On the far left of the diagram is a small section of microtubules. Microtubules (not shown clearly in this diagram) form part of the cytoskeleton of the cell (along with actin and other molecules) and are used to transport chemicals around the cell. The cytoskeleton plays a very important role in the development of neurons. Image reproduced from [50].*

The main difference between eukaryotes and prokaryotes is that eukaryotes have organelles such mitochondria and a nucleus. Mitochondria have their own DNA and as such are able to replicate independently of the host cell. They are also responsible for producing adenosine triphosphate (ATP) for the host cell.

The nucleus of the cell consists of another phospholipid membrane that separates the cell's chromosomal DNA from the cytosolic medium of the cell. The nuclear membrane contains a vast array of pores that allow very specific molecules

to enter and exit. When the cell divides, the nuclear membrane completely dissolves and then reforms as two separate nuclei, one for each daughter cell.

1.4.2 Basic structures

Neurons are eukaryotic cells found only in lifeforms that belong to the clade Eumetazoa (a subkingdom of Animalia that excludes sponges and other simple animal life). Neurons are the primary cells that form the nervous system of animals and can be subdivided into specialist roles such as sensory neurons or motor neurons depending on where they are in the body and what function they carry out. The nervous system is a network of these neurons which is used to control or coordinate all the other organs of the animal via the transmission of electrical signals through the neuronal circuitry.

Figure 1.7 is a diagram of a typical neuronal cell. A defining characteristic of all neuronal cells is the axon. This structure begins as a protrusion from the cell body that grows and elongates into a long thin wire. In the human body, the longest axons extend from the base of the spine to the periphery of the big toe which is about a metre in length [51]. Also shown in this diagram is the myelin sheath that is provided by Schwann cells wrapping themselves around the axon. Myelin sheaths are only found in lifeforms belonging to the Gnathostomata infraphylum (vertebrates with jaws) and is an ingenious evolutionary mechanism that increases the speed of nerve conduction [52]. Cephalopods (which do not belong to Gnathostomata) have unmyelinated nerves and have evolved fast nerve conduction by increasing the

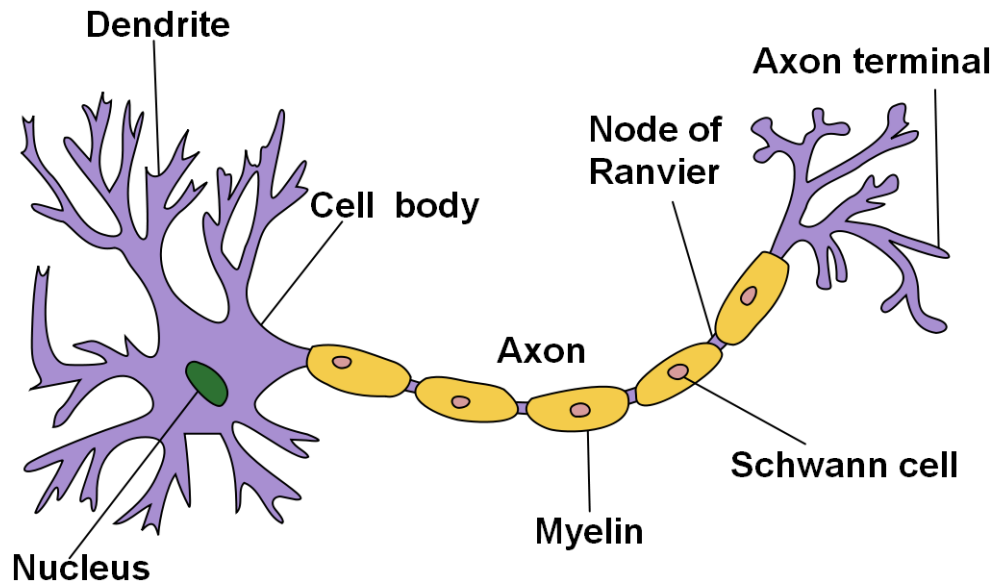


Figure 1.7: *Diagram of a typical developed neuronal cell. The cell body is much like that of the Eukaryote shown in Figure 1.6 containing the nucleus and other organelles necessary for its operation. Also shown in this diagram are main structures of neurons, the axon and the dendrites as well as the myelin sheath formed from Schwann cells. Dendrites transmit signals to the soma (cell body) whilst axons transmit signals away from the soma Image reproduced from [54].*

diameter of their axons. So much so, that the squid giant axon can be up to 1 mm in diameter and thus can be experimented on macroscopically as was shown by Hodgkin and Huxley in their 1952 work [53] which won them the Nobel prize for physiology in 1963.

1.4.2.1 The cytoskeleton

All cells have a structural system known as the cytoskeleton which is composed of a series of molecule structures that control and maintain the morphology of the cell. The cytoskeleton consists of three main components: microtubules, intermediate filaments and actin filaments. Microtubules are the largest of the three structures and are polymer filaments composed of a series of dimers made up of 55 kDa proteins known as α - and β -tubulin [55]. A diagram of a microtubule can be seen in Figure

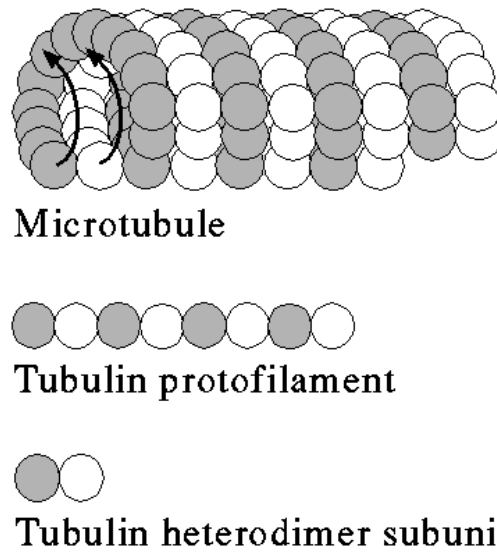


Figure 1.8: *Diagram of a microtubule showing how the two tubulin dimers link to form the polymer. The diameter of a microtubule is approximately 25 nm with a tubulin dimer measuring approximately 8 nm [55]. Image reproduced from [56].*

1.8. Microtubules (MT's) form a complex network throughout the cell and play a key role in the development of axons in neurons. They act as highways for chemicals and organelles to be transported around the cell in molecular vehicles such dynein and kinesin as mentioned above in section 1.3.1.3.

By contrast, actin filaments are much smaller than microtubules. They are composed of actin monomers (G-actin) which are 42 kDa proteins approximately 3 nm in size which polymerise to form an actin filament (F-actin) about 7 nm in diameter [57]. A diagram of an actin filament is shown in Figure 1.9.

Actin performs several vital purposes in cells such as cytokinesis and is the primary structure involved in muscle contraction. In cytokinetics, the actin filaments are very dynamic structures with monomers being continually adding on at one end and dissolved at the other in a process known as treadmilling [58], which is very important for understanding growth cone dynamics and will be discussed in more

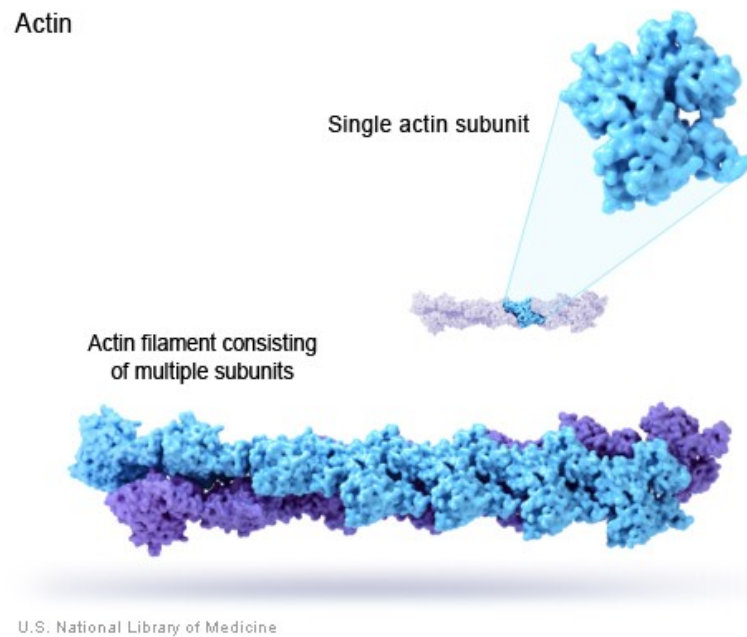


Figure 1.9: *Diagram of actin filament. The filament (f-actin) is composed of monomers of globulus actin (g-actin) in a helical structure. They are coloured differently here to show the helix but there is no difference between the molecules. Image reproduced from the U.S. National Library of Medicine.*

detail in the next subsection.

Actin polymerisation is the primary process that drives cell motility. To move across a substrate, cells use structures called filopodia (or pseudopodia) which are essentially membrane wrapped bundles of actin filaments that extend out of the of the cell body and adhere to the substrate. For example, filopodial growth is stimulated when an animal is wounded and fibroblasts move to close the wound [59]. Filopodia are also the primary machinery involved in the development of neuronal axons which will be discussed in more detail in section 1.4.3 and 1.5. Filopodia are also the subject of a mathematical model in chapter 2.3. Shown in Figure 1.10 is a fluorescent image of a cell stained with actin-GFP in which individual filopodia are visible. Actin will be revisited in Chapter 2 where I will discuss its role in modelling optically guided neuronal growth.

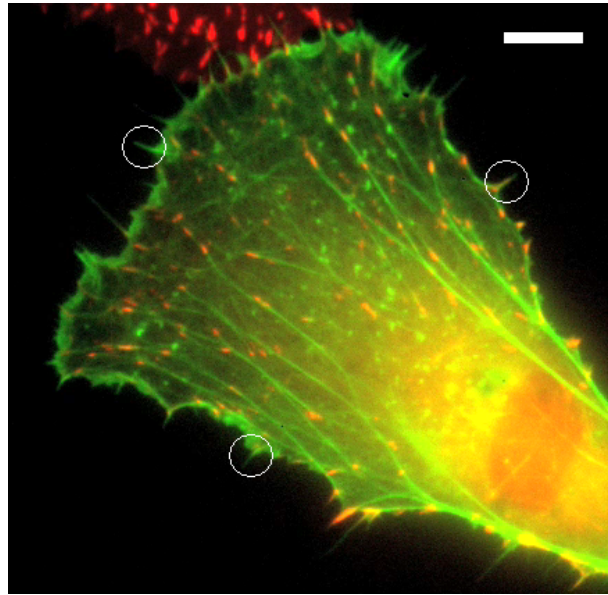


Figure 1.10: *Fluorescent image of a goldfish fibroblast tagged with actin-GFP. The network structure of the actin filaments is visible in the cell body, but also visible are the filopodia protruding from the edge of the membrane. I have marked out some obvious ones with white circles but there are many visible. This cell is also stained with rhodamine tagged vinculin which is the red colour visible. Scale bar is 10 microns. Image reproduced from [60].*

Intermediate filaments are a family of related proteins which form filaments with an average diameter of $\sim 10 \mu\text{m}$. Unlike actin and microtubules, there are several types of intermediate filament which can be subdivided into six types based on structural similarity. A discussion of intermediate filaments is beyond the scope of this thesis but for an extensive review see Fuchs et al [61].

1.4.2.2 Actin treadmilling

Treadmilling is the term given to the dynamic process of actin polymerisation and depolymerisation that takes place in the cell. Essentially, it is when one end of the filament grows (more molecules are added on to it, extending it) whilst the other end shrinks (molecules come away from it) which, even though the individual molecules in the filament may be stationary, gives the impression that the filament is moving.

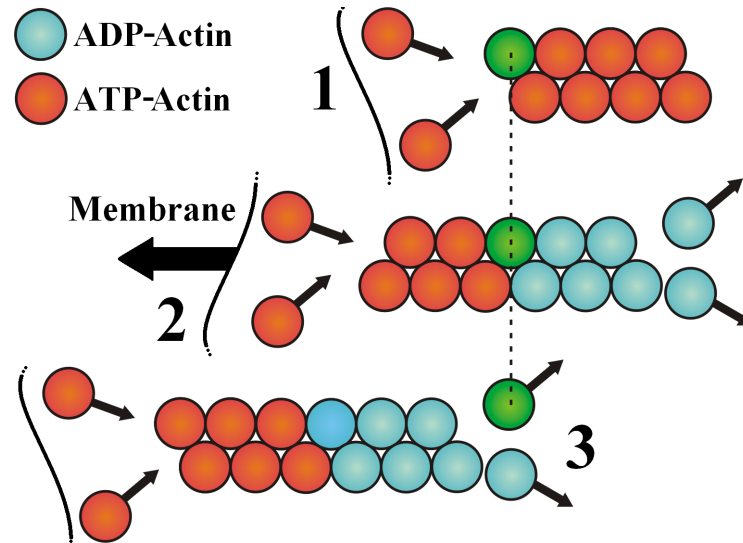


Figure 1.11: *Diagram of the actin treadmilling process advancing a cell membrane. Red spheres represent ATP-actin and blue spheres represent ADP-actin. The green sphere is used as a reference sphere to illustrate how a filament seems to move forward whilst the monomers remain stationary. Proceeding from the top: 1. ATP-actin bind together to form a filament. 2. As the filament grows the, the membrane is advanced and the actin at the end will dephosphorylate to ADP-actin. This end of the filament can depolymerise into ADP-actin monomers which can then be phosphorylated back into ATP-actin (not shown). 3. ATP-actin continues to polymerise onto the ATP end and the membrane continues to advance.*

Since actin can be linked to the extra cellular matrix (ECM) via integrins (e.g. laminin or fibronectin), then the treadmilling can affect the motion of the whole cell relative to the ECM [62]. A simplified diagram of how actin monomers can form a treadmilling filament is shown in Figure 1.11.

Treadmilling also occurs in microtubules since they can also be bound to the ECM by transmembrane proteins. The treadmilling of actin is particularly important in the growth cone of developing axons because it is what drives the motion of the growth cone. A chemical guidance cue (discussed in section 1.4.4) can affect this treadmilling which will change the way the growth cone moves e.g. towards or away from the source of the cue. Any process which affects cell motility will be having an effect on the treadmilling process. For example, a chemical stimulus

which reduces the availability of ATP, such as an ATPase, will result in a reduction of actin polymerisation since ATP is needed for actin to polymerise.

A common protein which increases the polymerisation of actin by increasing the number of nucleation sites for actin is the ARP2/3 (actin related proteins 2/3) complex [63]. Any stimulus which increases the presence of ARP2/3 in an area will also increase the polymerisation of actin in that area. Netrin-1 is an example of such a stimulus and this is discussed in section 1.4.4.1. A diagram of filopodia and ARP2/3 advancing the membrane is shown in Figure 1.12.

1.4.2.3 Action potentials

The function of neurons in metazoa is to provide the circuitry for the transmission of electrical signals throughout the body. The axons are essentially wires which transit these electrical signals to other neurons (or to muscles in the case of neuromuscular junctions)

These electrical signals are known as action potentials and the axons conduct them in a single direction, away from the cell body and toward the axon terminal, where it can either be transmitted to another neuron via a synapse junction or to a muscle cell via a neuromuscular junction.

Synapses can be formed between axons and dendrites (axodendritic), axons and other axons (axoaxonic), axons and other cell bodies (axosomatic) and even between dendrites (dendrodendritic). Whilst most neurons have only one axon, they can have many dendrites (up to 10,000 [64]). Thus a neuron can have many inputs, but usually only one output.

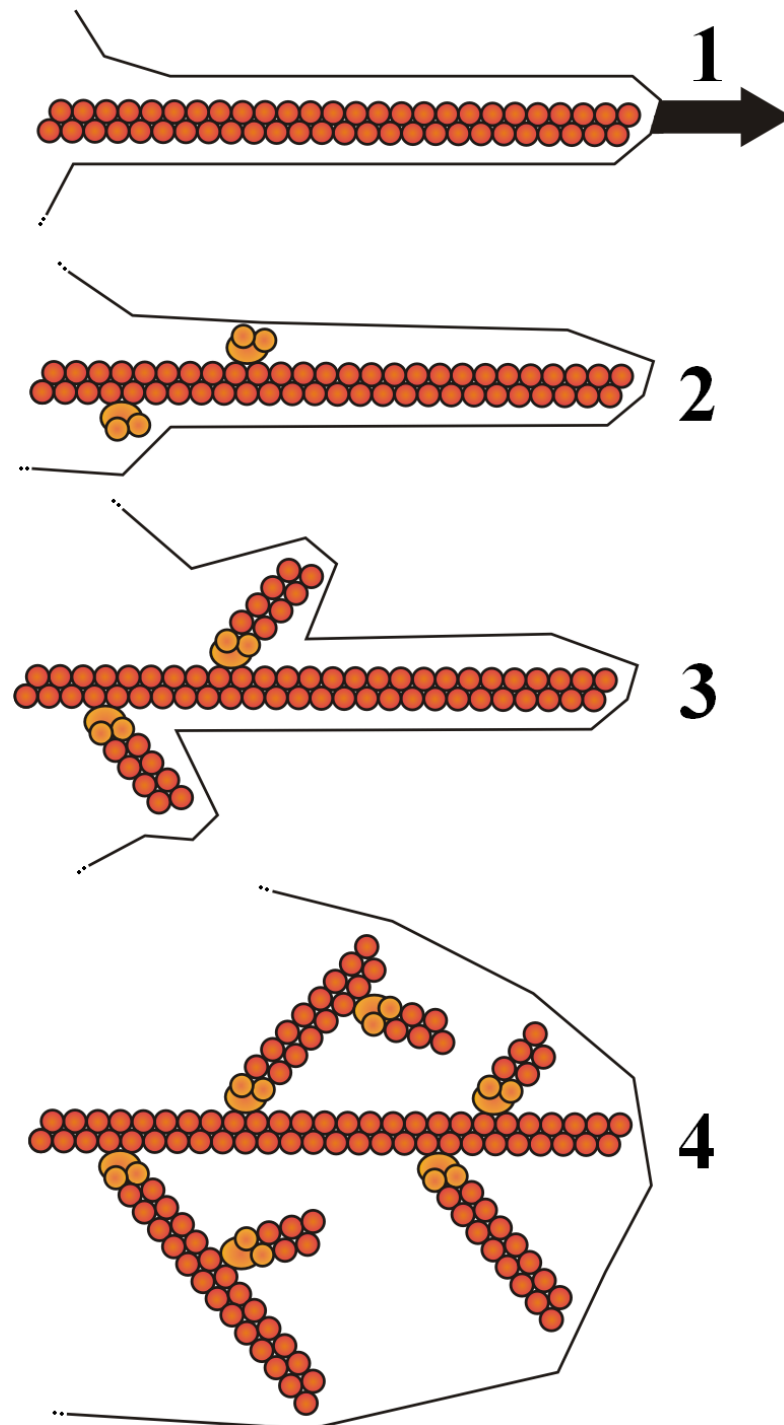


Figure 1.12: *Simplified diagram of how a cell membrane advances. Red spheres represent actin and the orange complex represents the ARP2/3 complex. Proceeding from the top: 1. A bundle of actin filaments polymerise and push the membrane forward producing a protrusion known as a filopodia (for simplicity only a single actin filament is shown in this figure). 2. ARP2/3 complexes attach to these filaments and create nucleation sites for new filaments. 3. Actin polymerises onto the fresh nucleation sites and pushes the membrane out further. 4. Steps 2 and 3 continue until a mesh of actin filaments exist and the membrane has been advanced wholly. In reality, several filopodia will be advancing side by side and the meshes they produce will overlap giving the impression of a continuous advancing membrane front. If there is no ARP2/3 available then the original filopodia will eventually depolymerise without providing nucleation points and the membrane will not advance.*

An action potential is triggered when the neuron is subject to enough stimulation to ‘fire’ an electrical signal. The potential across the membrane of a typical neuron is maintained at around -70 mV by the cell pumping sodium (Na^+) and potassium (K^+) ions in and out. This potential is known as the resting potential. The cell actively works (uses ATP) to pump these ions against the electrical gradient to setup the membrane potential. Neurons are stimulated by environmental changes that alter this membrane potential. Opening potassium channels further decreases the membrane potential (hyperpolarises) whilst opening sodium channels depolarise the neuron. If these stimuli are small enough, the cell will quickly act to return to the resting potential within a few milliseconds. However, if the depolarising stimulus is sufficiently strong, a threshold is crossed which triggers a positive feedback event whereby more sodium flow into the cell causes more sodium flow into the cell. This quickly completely depolarises the neuron and briefly reverses the polarity of the membrane potential. Once the sodium channels have been fully opened the cell begins to recover to the resting potential by pumping out the sodium again. This entire sequence takes only a few milliseconds. This short burst of electrical activity is the action potential, and it immediately begins to propagate down the axon.

The action potential is an all or nothing event. Either the stimulus is sufficient to cause the positive feedback cascade, or it isn’t. The action potential is digital in that it is either fully on or fully off without any inbetween levels.

The stimulation which can cause a neuron to fire can come from other other neurons or from external factors. In the case of photoreceptors in the retina, single pho-

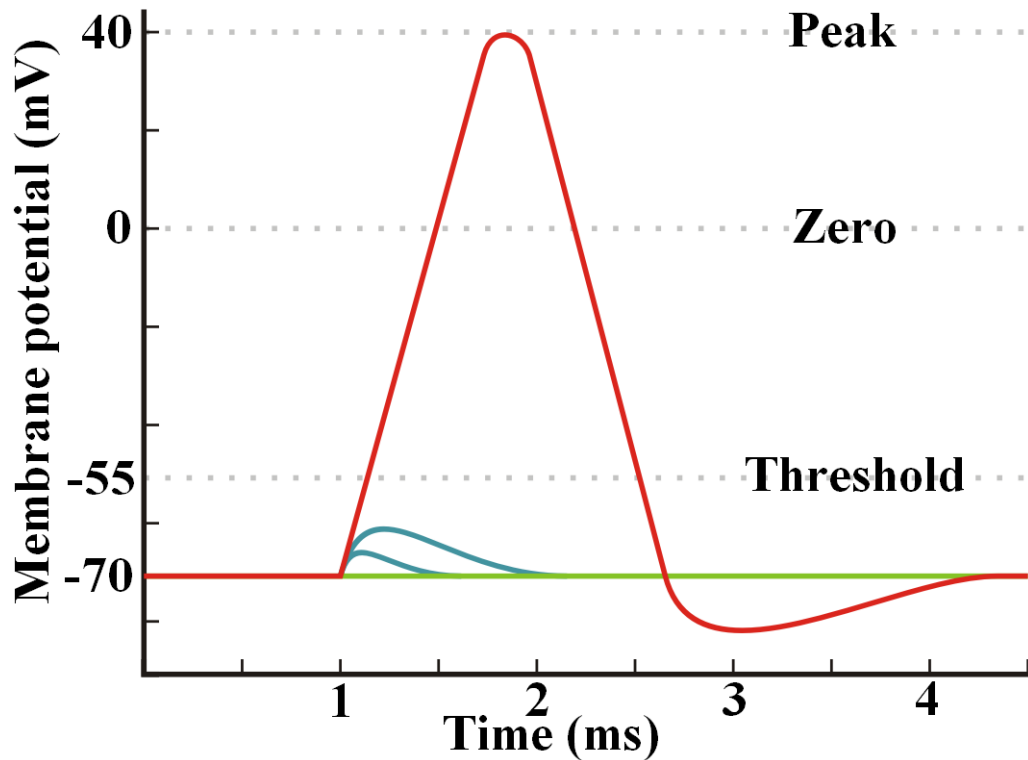


Figure 1.13: *Simplified diagram of how the membrane potential changes during an action potential. The green line represents a neuron that is not perturbed over the time frame, blue lines represent stimulations that were insufficient to trigger an action potential and the red line represents a sufficiently strong stimulus that triggers an action potential. The cell membrane has a resting potential of -70 mV compared to the extra cellular medium. In order for a stimulus to successfully trigger an action potential it must breach a threshold voltage in order for positive feedback to accelerate the depolarisation. The blue lines fall short of this threshold (which is around -55 mV) and so the membrane potential recovers without the neuron firing. The stimulus for the red line need only be sufficient to get the potential above -55 mV for the cell's own feedback mechanism to take effect and hyperpolarise the membrane to a peak potential of around 40 mV. This pulse will propagate down the membrane of the cell via the Na^+ and K^+ ion gates along it opening in succession. Once the peak potential has been reached the membrane begins to recover and will overshoot the resting potential slightly before returning to it.*

tons of light can trigger an action potential [65]. In the case of other neurons, when an action potential reaches a synapse, the presynaptic membrane releases vesicles of neurotransmitters which trigger neuroreceptors on the postsynaptic membrane which causes sodium channels to open and depolarise the postsynaptic cell which can trigger another action potential. Generally, neurons have several inputs and only one output and it takes several inputs arriving at the same time to sufficiently depolarise the postsynaptic cell to transmit the action potential. In this way neurons can be thought to act as logic AND gates.

Action potentials have been shown to effect the development of growth cones by changing intracellular levels of calcium ions (Ca^{2+}) [66]. In particular, the influx of calcium ions into the growth cone has been shown to collapse the growth cone by disrupting the actin filaments within it [67]. It has also been shown that the turning effect on a growth cone by Netrin-1 (discussed in section 1.4.4.1) can be completely negated by the removal of extracellular calcium ions [68].

Pulsed femtosecond lasers have been demonstrated to be capable of triggering action potentials in neurons. This has been attributed to a multiphoton effect and is not possible under cw irradiation [69].

1.4.3 The growth cone

1.4.3.1 Introduction

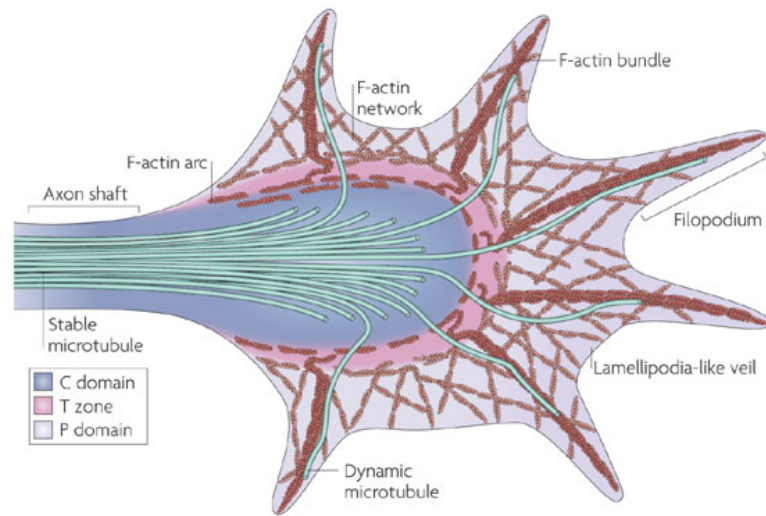
Neurogenesis, the creation of neurons from stem cells, is most active during development and, until very recently, was thought to be impossible in adults [70].

A freshly created neuron structurally resembles a fibroblast initially and has none of the archetypal neuronal features shown in Figure 1.7 such as an axon or dendrites. However, the production of the axon begins as soon as this neuron differentiates and a structure called the growth cone begins to protrude from the cell body [71].

The growth cone is a highly motile path-finding structure that forms the tip of a developing axon. It consists of a flat area known as the lamellipodium which is structurally made up by a mesh of actin filaments. The filopodia extend as spiny protrusions from the lamellipodia and are made up of bundles of parallel actin filaments. The whole structure is connected to the cell body by a series of parallel microtubules feeding it resources and removing waste. Shown in Figure 1.14 is a diagram of a growth cone showing these structures. Figure 1.15 is an electron microscope image of a developing growth cone. Visible is the flat lamellipodium from which the filopodia protrude. The advancement of the growth cone is driven by actin polymerisation at the leading edge [72].

Growth cones are important because they exist to connect developing axons to the correct places in the body to ensure that the animal is born with a functional nervous system. Because there are so many permutations of possible nervous system structures and that only a few of them will result in a healthy animal, a complex system of guiding the growth cones to ensure they reach their correct targets has evolved. This system is mostly based on chemical signal detection.

All around the membrane of the growth cone are various molecular binding proteins that act as sensors and feedback into the actin polymerising machinery



Nature Reviews | Molecular Cell Biology

Figure 1.14: *Diagram of neuronal growth cone. The microtubule network is shown as green and the actin as red. As shown, the filopodia are bundles of actin filaments that protrude away from the growth cone in search of substrate to attach to. The axon being dragged by the advancing growth cone consists almost entirely of parallel microtubules. Image from [73].*

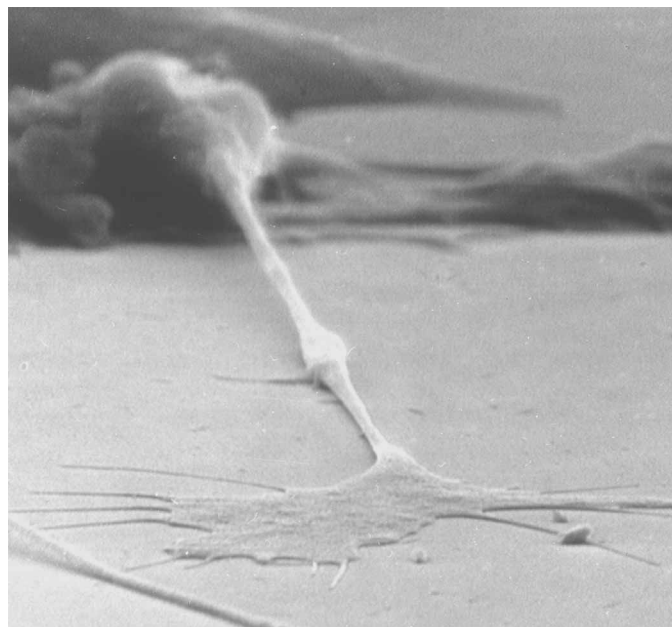


Figure 1.15: *Image of the growth cone of a mammalian sensory neuron with an electron microscope. The growth cone is a very flat structure (only a couple of microns in height) compared to the cell body (visible in the background). The large flat area is the lamellipodium and the thin spiny protrusions from it are the filopodia. Image taken by Ken Balazovich of the Tosney lab at the University of Miami.*

to affect the direction of growth [74]. Chemical cues secreted throughout the body direct the developing axons to their correct targets. Once a growth cone has reached and bound to its target it will cease growing and become a synapse connecting it to the other cell [75].

The actual cues that growth cones respond to has been the subject of intense research for many years [76–79] and a comprehensive review of this work is beyond the scope of this thesis. However, a brief review of work which specifically uses these chemical cues to artificially guide developing axons is necessary since this can be related to optically guided neuronal growth.

1.4.4 Growth cone guidance

1.4.4.1 Chemical cues

The use of lasers to guide axons is a relatively recent innovation, previously our knowledge on how growth cones are controlled has come from studies using chemical gradients and scaffolds.

The justification for using chemicals is easily understandable since this is exactly how the axons develop *in vivo* and by exerting control over which chemicals a developing axon is exposed to, it should be possible to exert control over its direction of growth. Shown in Figure 1.16 is a diagram of how a growth cone would respond to an added chemical gradient.

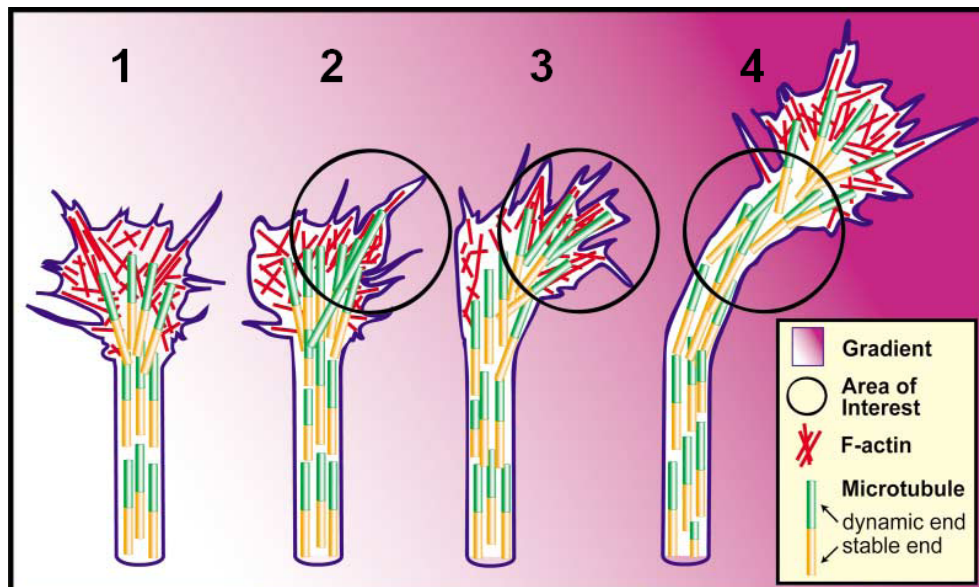


Figure 1.16: *Diagram of a growth cone turning in the presence of an attractive chemical gradient (pink=high concentration, white=low concentration). The diagram is a sequence proceeding from 1-4. 1. The growth cone before the gradient is introduced with a F-actin network making up the lamellipodia and filopodia and with a MT bundle in the shaft. 2. When a chemoattractant is detected, F-actin selectively polymerizes on the side of the growth cone toward the attractant, forming increased numbers of filopodia and lamellipodia. This bias of actin polymerization to one side of the growth cone causes less polymerization on the opposite side, favoring shrinkage/retraction of lamellipodia and filopodia. 3. Numbers and size of F-actin bundles increase and are stabilized by actin-bundling proteins and linkages to the substrate. 4. When the growth cone is pointing directly towards the chemoattractant, no one side of the growth is favoured over the other and F-actin polymerisation on both sides is stabilised. Image and caption reproduced from [80] but edited for the purposes of this thesis.*

There are many chemical factors that can control neuronal growth cones. These chemical signals can be both attractive or repulsive to growth cones. Shown in Table 1.1 is a list of such factors.

These cues can be subdivided based on their operation. Netrins, semaphorins and Slit are diffusible secreted proteins whilst cadherin is a cell adhesion molecule (CAM) and laminin is a secreted surface adhesion molecule (SAM).

Netrins are a class of molecules identified as being involved in axon guidance and are genetically homologous across the Eumetazoa [87]. Netrin-1 has been used to

| Environmental cue | Effect | Target | References |
|-------------------|-----------------------------------|--------------------|------------|
| Netrins | Attractive/repulsive [#] | DCC/UNC5 receptor | [81,82] |
| Semaphorins | Mostly repulsive ^{##} | Multiple receptors | [81,83] |
| Ephrins | Attractive/repulsive | Eph A/B receptor | [81,84] |
| Laminin | Adhesive | Integrin receptor | [82] |
| Cadherin | Adhesive | Other cadherins | [79,85] |
| Slit | Repulsive | Robo receptor | [81,86] |

Table 1.1: List of well known chemical cues involved in growth cone guidance. [#] depending on what receptor is being activated, ^{##} semaphorin 3A is attractive. This list is not exhaustive.

artificially guide the developing axon of a spinal neuron from *Xenopus laevis* [88] and shown in Figure 1.17 is an axon turning towards a source of Netrin-1. Netrins are bifunctional in that they can act as either chemoattractants or chemorepellants depending on which surface protein it binds to, for example Netrin-1 acts as an attractant when binding to the DCC (deleted in colorectal carcinoma) receptor but as a repellent when binding to the UNC5 (uncoordinated locomotion-5) receptor [89]. Structurally, Netrins are similar to laminin which is an important surface adhesion molecule (SAM) [77].

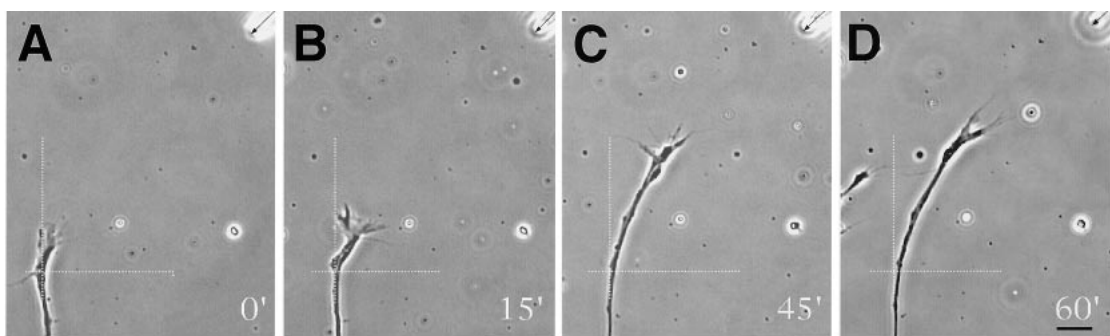


Figure 1.17: Time lapse image sequence of a *Xenopus laevis* spinal neuron turning towards a diffusing source of Netrin-1. Sequence progresses from A to D and the time in minutes is shown in the bottom right corner of each frame. The arrow in the top right shows the location of the Netrin-1 source and, as can be seen, the neuron is growing towards it. The scale bar is 10 μm , the number in the lower right corner is the time in minutes. Image reproduced from [88].

Semaphorins are another group of chemical guidance cues that have been in-

investigated for axon guidance. Semaphorins make up the largest group of guidance cues consisting of at least 30 members [90]. They were originally thought to act as moderators of axon repulsion *in vitro* [91,92] and *in vivo* [93–95] but they can act as chemoattractants as well [96]. Shown in Figure 1.18 is a series of images of a *Xenopus* spinal neuron reacting to the presence of Sema3A normally and then in presence of a protein (truncated Plexin-A1) that blocks the repulsive effects of Sema3A.

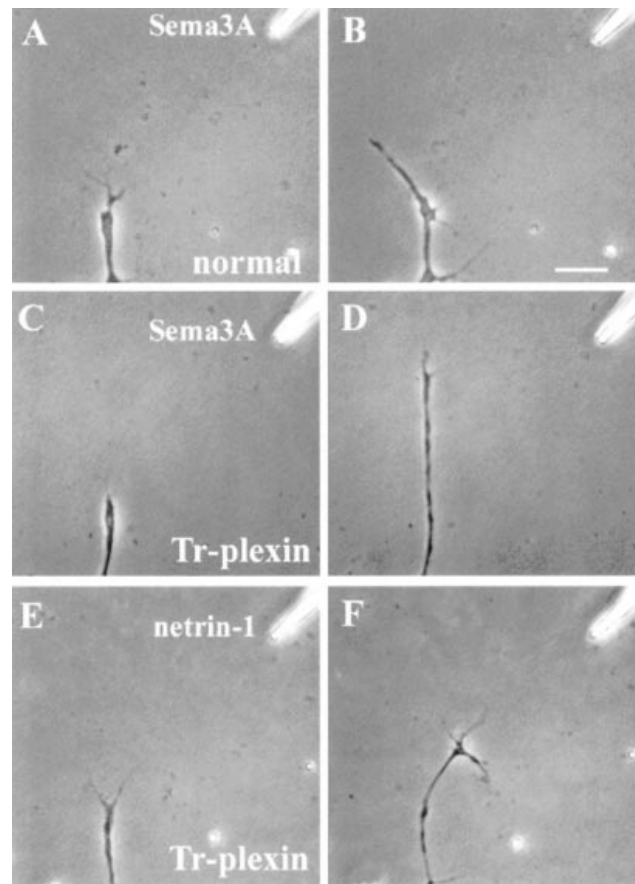


Figure 1.18: A control spinal neuron exposed to a gradient of Sema3A emanating from a pipette (A) is repelled away over a period of 1 hr (B). In contrast, a GFP-expressing spinal neuron from an embryo injected with mRNA for the truncated plexin-A1 construct (C) is not affected after 1 hr by Sema3A (D). A similar neuron (E) shows a normal attractive response to netrin-1 after 1 hr (F). Image and caption reproduced from [97].

Netrins and (some) Semaphorins are long range guidance cues because they are secreted by other cells and diffuse over long distances to attract (or repel) growth

cones. Other cues can be contact only such as transmembrane Semaphorins, Cadherins and laminins.

Cadherins are a family of homophilic transmembrane CAM's that are known to play an important role in synapse formation [98]. N-Cadherin has specifically been shown to affect the cytoskeleton in the growth cone by interaction with the FGF (Fibroblast Growth Factor) receptor [85].

Laminins are a well known group of extracellular matrix (ECM) glycoproteins that are common to the tissues of all metazoans [99]. Laminin is known to affect cell adhesion by activating surface integrins and it is important for axon development and it has been used successfully to guide axons [100,101]. In 2005 a group of scientists were able to print patterns of laminin on to a substrate for tissue culturing PC-12 cells (a neuronal cell line) [102]. Shown in Figure 1.19 is a image from their paper showing how the neurons would only grow along the parts of the substrate that contain laminin and were thus favourable for growth. Laminin is commonly used as a substrate treatment for the culturing of cells *in vitro* [103] and has been used to successfully culture difficult stem cell lines [104].

All of these chemical cues affect the cytoskeleton of the growth cone. This happens because the receptors these proteins bind to trigger specific chemical activity within the cell via complex metabolic pathways which ultimately results in a cytoskeletal response. For example, Netrin-1 binds to the DCC receptor which then rapidly activates several proteins including CDC42 (cell division control protein 42), RAC1 (Ras-related C3 botulinum toxin substrate 1), PAK1 (p21 protein activated

kinase 1) and N-WASP (neural Wiskott-Aldrich syndrome protein) which all form a complex around the DCC receptor. The N-WASP in this complex associates with the ARP2/3 (actin related protein 2/3) complex which promotes the nucleation of F-actin, thus DCC essentially creates a transmembrane bridge between Netrin-1 and the actin cytoskeleton [105].

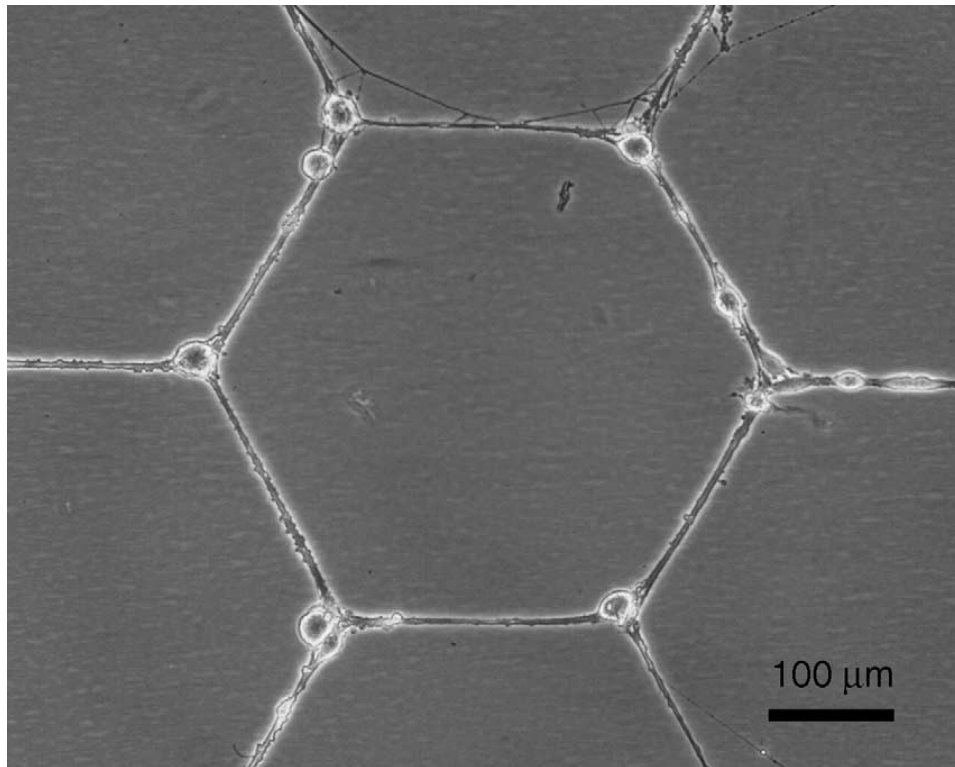


Figure 1.19: *PC-12 cells grown on a substrate containing a hexagonal pattern of laminin. As can be seen the cells and their axons are only growing on the laminin coated parts of the substrate. Image reproduced from [102].*

This discussion on the use of chemicals to artificially control the growth of neurites is by no means exhaustive. As mentioned before, research in this direction has been proceeding for several decades and there is no way to appropriately collate all the results of this research into a suitable section for this thesis.

1.4.4.2 Other cues

Chemical signals are not the only stimuli that has been shown to effect growth cone guidance. The definition of ‘other’ here is essentially anything that isn’t chemical and this definition includes interactions with light, electric fields and scaffolds.

The observation that electrical fields could first influence cell growth was in a 1920 publication by Ingvar et al [106] who reported that a DC electric field could direct the outgrowth of the central nervous system of a developing chick embryo. Since then electric fields have been shown to be involved in processes such as wound closing and tissue regeneration [107]. The presence of a constant electric field has also been shown to effect growth cone turning [107–109].

It has been demonstrated comprehensively that electrical fields can have a profound effect on the motility of cells. In a 1995 publication, Erskine et al subjected *Xenopus* spinal neurons to constant DC electric fields and reported that the growth cones would turn towards the cathodes in fields as low as 10 mV/mm [108, 109]. It has since been shown that growth cones can also turn towards the anode depending on the electrical properties of the substrate the cells are adhering to [110]. It has also been reported that growth cones grow about eight times faster towards the cathode than the anode [111]. The mechanism for this behaviour is still not entirely clear but the authors of these studies suggest that perturbation to extracellular calcium ion levels which are already known to affect the cytoskeleton of the growth cone [108].

Other cues such as scaffolds, though technically acting through chemicals signalling, coated with molecules (e.g. laminin) to promote the adhesion of growth

cones have been manufactured to be used in the control of axon growth and have a potential medical use in nerve regeneration [112].

Investigations into the interaction of growth cones with light is the purpose of the thesis. In the next section I will detail the previous experiments of this field of research and how this leads up to my experiments.

1.5 Optically guided neuronal growth

In this section I will review the previous literature on the use a focused laser beam to influence the growth cone of a developing neurite.

1.5.1 Discovery and first experiment

The first mention of light having a motile effect on mammalian cells was reported in 1991 by G. Albrecht-Buehler [113]. In that work, an infrared light source in the range of 800-900 nm was focused down to a spot on a microscope slide containing 3T3 fibroblasts. It was observed that these cells extended filopodia towards the light source. This was not done using a laser and the total power in the 7 μm diameter light spot was estimated to be only 170 pW. However this work demonstrated the proof of concept that concentrated light could be used as a mechanical cellular influence, and so it follows that a laser used as the source of this light may also be used in the same way and with all the benefits that come with using a laser (e.g. controllable spot size, greater range of power density and wavelength)

The first experiment to report an effect of laser irradiation on a neuronal growth

cone was by Ehrlicher et al in 2002 [114]. In this study the researchers subjected cultures of NG-108 and PC-12 (mouse/rat neuroblastomas) cells to a focused $2\ \mu\text{m}$ diameter spot from a Ti:sapphire (800 nm) laser at powers upto 120 mW. They reported that in 80% of experiments (35 out of 44) they could change the direction of the advancing growth cone and that the rate of growth increased from an average of $7\pm 3\ \mu\text{m}/\text{h}$ to $37.5\pm 22.5\ \mu\text{m}/\text{h}$. Shown in Figure 1.20 is an image sequence showing two typical successful experiments. They reported successful growth in 35 out of 44 experiments

Notably, they also attempted to model the mechanism of the growth cone behaviour as a laser induced increased flow of actin monomers towards the edge of the growth cone where the laser was positioned. This, they presumed, would increase the polymerisation of F-actin and thus increase the extension of the growth cone towards the laser. Their model model predicted a weak effect but enough, to explain the effect and the increased rate of growth [114]. Their model forms the basis for one used in my 2008 publication [115] and will discussed in more detail in Chapter 2.

1.5.2 Effect of beam shape

The next publication in this field was in 2005 by Mohanty et al [116]. This paper reported the successful employment of line optical tweezers to guide the growth cones of N15-115 cells (an immortalised mouse neuroblastoma cell line). They focused the light from a Nd:YAG operating at 1064 nm and power 120 mW through a cylindrical

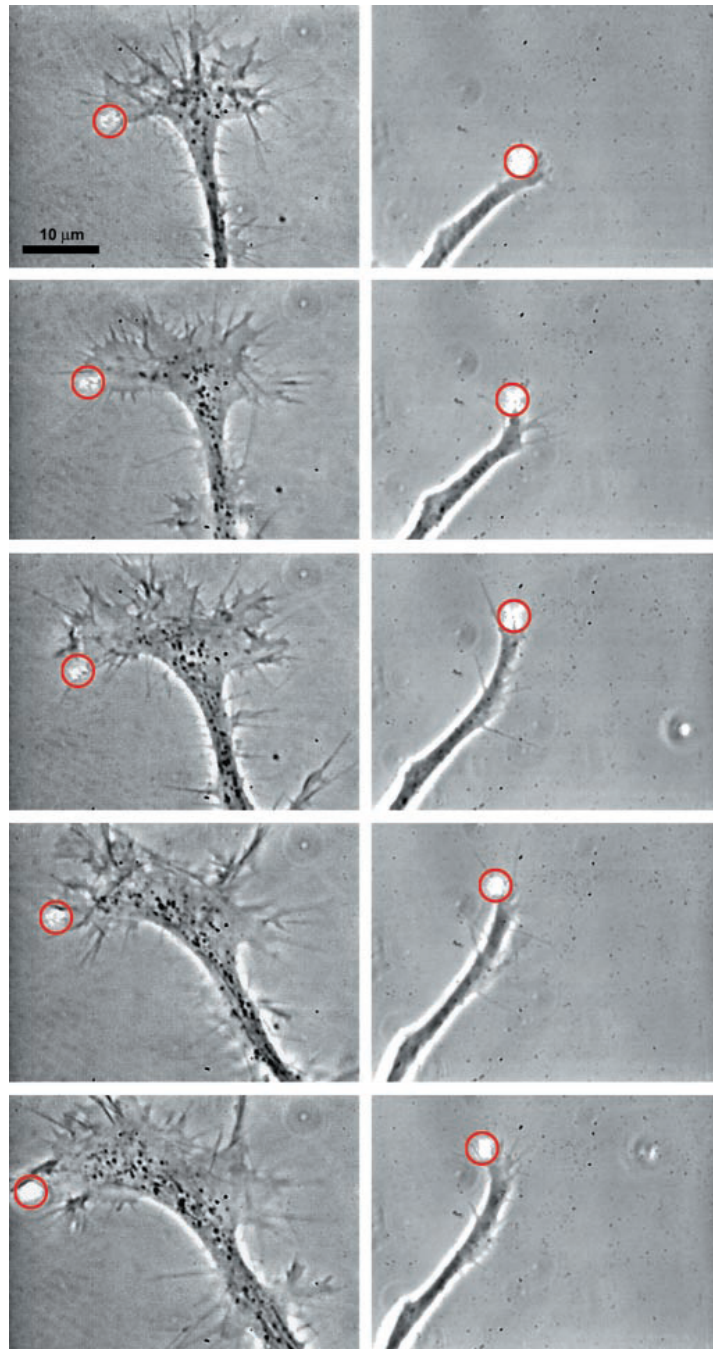


Figure 1.20: Time sequences of optically guided turns of neurons and optically enhanced neuronal growth. Optically induced turns are shown for a time period of 40 min (Left) and 20 min (Right). The time interval between successive pictures is 10 min (Left) and 5 min (Right). The power of the laser spot is 100mW(Left) and 60mW(Right), and a red circle indicates the position of the laser spot. Optical control was achieved for extensive flat growth cones (Left) as well as for small, tube-like growth cones (Right). Before the laser altered the direction of the growth cone, the nerve was growing upward (Left) or to the right side (Right). The growth direction changes on the order of 90° under optical guidance. Note that the apparent change growth direction appears to be smaller because the axon straightens into the new direction. Image and caption reproduced from [114].

lens to achieve their asymmetrical line profile of dimensions $1 \times 40 \mu\text{m}$. They also reported the ability to create a new growth cone by aiming the laser at the cell body of their neuronal cell which has not been repeated by any other study.

This paper also attempted to model the behaviour of the growth cone as a laser induced increase in the flow of actin. However, where this model differed from the one put forward by Ehrlicher et al was in the mechanism of the actin flow. Ehrlicher reported that their beam was not sufficient to optically tweeze the actin, but was enough to influence the flow of actin [114] whereas Mohanty et al specifically claim that their line trap works as a “sling shot” which is sufficient to propel the actin monomers away from the centre of their beam. Figure 1.21 is the diagram they published to illustrate this effect. They also reported the inability of a symmetric line profile to affect neuron growth.

Mohanty et al also carried out the experiments at room temperature ($25 \text{ }^\circ\text{C}$) as opposed to $37 \text{ }^\circ\text{C}$ which is the optimal temperature for the cell line they were using. While this may not have had any adverse effect on their experiments it is an important consideration since they suggest that temperature rises may be a possible mechanism. Chapter 2 of this thesis will contain more discussion on the Mohanty “sling shot” model presented here.

1.5.3 Effect of wavelength

The two previous studies were both carried out using different cell lines and different laser sources. In 2006, Stevenson et al published a study that compared the two laser

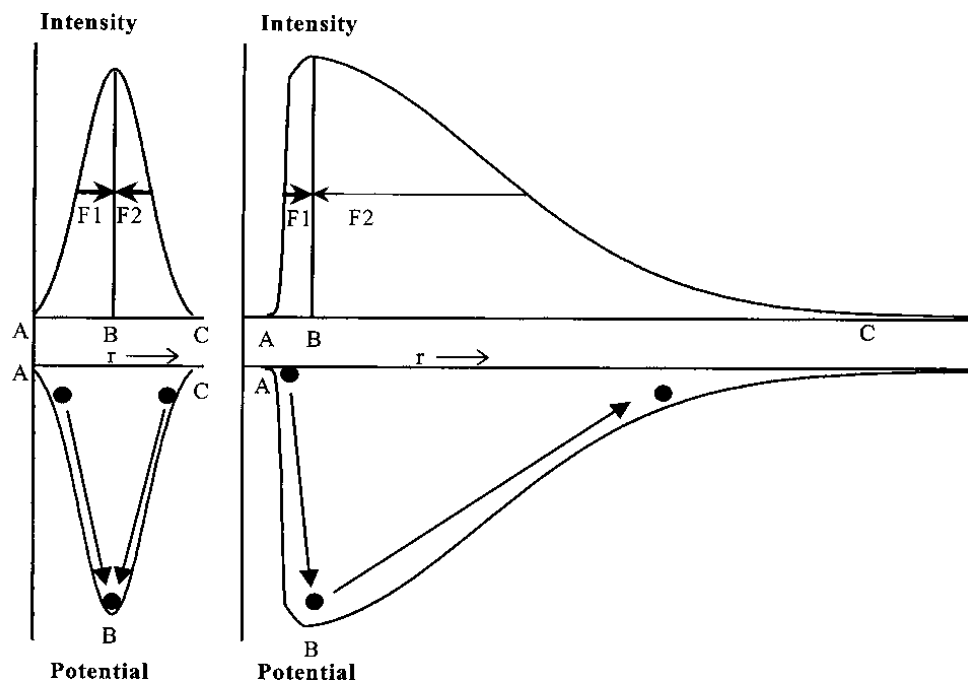


Figure 1.21: Illustration of “sling shot” effect on actin monomers due to asymmetrical line tweezers. Left is a potential well diagram for a Gaussian beam showing a particle entering from side A and C and reaching equilibrium at the beam centre, position B. On the right the same diagram but for an asymmetrical line trap showing a particle entering from side A and moving to the beam centre, B, before being “sling-shotted” out of the potential well towards C. It was not mentioned what would happen to particles entering the line trap at edge C. Image reproduced from [116].

sources on the same cell line [117]. They performed their studies on the NG-108 cell line at the optimal temperature of 37 °C and reported that light of 780 nm (9-25 mW) was just as effective at eliciting a response as light of 1064 nm (8-22 mW). They also attempted neuron growth using a violet diode laser of 405 nm but this did not induce successful growth cone guidance.

The researchers also attempted to calculate the possible temperature increase due to the presence of the IR laser spot which was achieved using a dual beam method pioneered by Mao et al in 2005 [118]. They first brought a 660 nm laser diode beam to focus through a 60x objective and used it to trap a 2 μm silica bead. They measured the maximum average lateral trapping velocity of the particle as a function of beam power (from 13 to 36 mW) and used this to calculate the ratio of the Q-value of the laser to the viscosity of the surrounding media. They then focussed a 15 mW beam from the 780 nm diode laser and brought it to focus in the same plane but laterally shifted 5 μm away from the 660 nm trap. With the 780 nm beam present, they repeated their measurements of the maximum average lateral trapping velocity of the silica as a function of beam power from the 660 nm laser. They could then calculate the fractional change in the ratio of the Q-value to the viscosity and could therefore calculate the change in viscosity due to the presence of the 780 nm laser. Because viscosity is a function of temperature this then meant that a change in temperature could be calculated. Stevenson et al reported a temperature of 25 °C in the presence of the 660 nm beam alone and 26.4 ± 1.5 °C when the 780 nm beam was present. Repeating procedure with the 1064 nm laser in place of the 780

nm laser (and at the same power of 15 mW) the authors reported a temperature of 28.1 ± 2.3 °C.

This shows that the heating effect is greater at 1064 nm than at 780 nm which is expected given the absorption spectrum of water. A previous study reported that the temperature rise in a cell due the presence of a focused 1064 nm laser is $\sim 1.15 \pm 0.25$ °C/100 mW [119].

These three studies form the starting point for my experiments into optically guided neuronal growth. Of particular interest was the “sling-shot” model of actin flow proposed by Mohanty et al as well as the use of line optical tweezers. The next chapter details the execution of my experiments in comparing line tweezers of different configurations which led to the development of new mathematical model for the behaviour of actin in an optical field.

However, it is worth detailing one more study into optically guided neuronal growth that was published after I had concluded the optical line trap work in 2008.

1.5.4 Effect of pulsed operation compared to continuous wave

So far, all previous experiments into optically guided neuronal growth have used continuous wave (cw) laser beams. In 2008, Mathew et al conducted a study comparing the effect of a femtosecond pulsed laser to a continuous wave beam of the same wavelength. What is particularly interesting about their experiment is that the laser beam was focused a distance >15 μm away from the edge of the growth cone. All previous studies have worked by focusing the laser directly onto the growth

cone.

For their pulsed laser they used a mode locked Ti:sapphire operating at 800 nm with a pulse duration of 150 fs at a repetition rate of 76 MHz. The same laser was then switched to cw mode used for the cw experiments. Both beams were operated at a power of 3 mW (average power for the pulsed beam) which is the lowest power ever reported for use in neuronal growth experiments.

The cell culture they used is also of note because they are the first group to report the use of primary cells. Primary cells are those taken directly from an animal and not from an immortalised cell line. The cells they used were harvested from the cerebral cortex of CD1 mouse embryos at 15 days gestation. Experiments were performed on a heated microscope stage to keep the samples at the optimal temperature of 37 °C.

They showed that the cw laser was incapable of attracting growth cones when focused at a distance $>15 \mu\text{m}$. This is in good agreement with previous studies which only reported success for beams focused onto the growth cone. However, when they switched the laser into femtosecond operation, they reported that growth cones became attracted and grew towards the beam. This is the only study so far to show a difference between cw and pulsed light and suggests a new mechanism for optically guided neuronal growth.

There seem to be several plausible mechanisms implied by this observation. The authors put forward a few suggestions including that the production of shockwaves created by the pulses could result in growth cone attraction, or that the large electric

field of the pulses could be felt on the distant cells and manifest as an attractive response.

One mechanism they did not consider was a two-photon absorption effect on a molecule(s) present in the medium. A compound that underwent a chemical change as a result of the laser would diffuse from the laser spot in a similar fashion to how Netrin-1 or Sema3A is diffused from a pipette by previous chemically induced neuron growth studies [88,89,91,96]. The diffuse chemical(s) could plausibly be detected by the receptors on the growth cone which could result in a chemoattractant pathway being activated.

Chapter 2

Using optical line traps for neuronal growth

2.1 Introduction

In this chapter I describe experiments using line profile laser beams for use in optically guiding neuronal growth cones. The motivation for this work stems from a study in 2005 by Mohanty et al [116] which had claimed that asymmetric line optical tweezers could be used to bias the direction of growing neurons as well as generate new proto-axon protrusions (as also discussed in Chapter 1.5.2).

Up until 2005, only Gaussian profiled laser beams had been used to induce optically guided neuronal growth. The study by Mohanty et al was the first to begin investigating the effect different beam configurations had on this phenomenon and investigations continuing down this path have yielded interesting publications and promising explanations for the phenomenon.

The explanation given by Mohanty et al for these observations was that an asymmetric line profile acted like a “sling shot” and accelerated monomers of actin along the major axis of the beam profile. In their experiments they observed that when the direction of the ‘bias’ in their line profile was oriented outwards from the the cell membrane, then the neuron would grow along the line of the beam.

Specifically, they reported that under the influence of an asymmetrical laser beam of dimensions 1 x 40 μm and average power 120 mW neuronal growth cones could be guided at rates of upto 32 ± 6 $\mu\text{m}/\text{h}$. This compared to an observed rate of 1 ± 1 $\mu\text{m}/\text{h}$ for unexposed growth cones. The growth rate of the exposed growth cone is similar to the 37.5 ± 22.5 $\mu\text{m}/\text{h}$ growth rate that Ehrlicher et al reported in 2002 [114]. They repeated the experiment using a symmetrical line profile and reported that this did not work. This study also reported the first observation of a laser inducing a new protrusion from the cell body and is the only publication to report so to date.

If the “sling shot” mechanism hypothesised by Mohanty et al is accurate, then when the bias of the line is oriented inwards to the cell, the cell membrane should retract, since actin monomers should be prevented from reaching nucleation sites at the leading edge and polymerising into filaments (see Figure 1.11, without any actin at the leading edge the membrane will not advance). Though the authors suggested this, they did not investigate it by experiment. A deeper explanation of what is meant by the ‘bias’ of the line profile is included in the next section.

The experiments I carried out were designed to test the “sling shot” hypothesis

by comparing the effect of different asymmetric line profile beams to a symmetric line profile control. If there was a noticeable difference in the ability of these beam configurations to induce guidance in neuronal growth cones then the “sling shot” mechanism would be plausible and worthy of further investigation.

For this work the asymmetric line optical tweezers were generated using a cylindrical lens system similar to that employed by Mohanty et al [116,120]. However, this asymmetrical beam was used in two configurations corresponding to whether the neuron should be attracted or repelled by the laser. It was observed that the growth cones would align with the major axis of the beam and grow towards the centre (defined here as the most intense region of the beam) regardless of the orientation of the beam profile. The beam was also configured to have a symmetrical intensity profile (i.e. biased in no direction) and this beam configuration was used as a control to investigate whether the neurons would respond to a line optical tweezers without an asymmetrical profile intensity.

My results showed that there was no significant statistical difference in bias for any configuration of asymmetric beam or indeed for a symmetric line profile [115]. The behaviour of the growth cones in the various beam configurations was then explained by the use of a detailed mathematical model which was originally constructed by Dr Michael Mazilu using Mathematica 5.2 (Wolfram) [115] and was built on earlier work done by Ehrlicher et al [114]. This model was subsequently redeveloped and reconstructed with the raw computer code being included as an appendix to this thesis. This chapter begins with a brief introduction to the cell

culturing methods used in these experiments and then details the experimental setup and results using different optical line traps and concludes with a discussion on the importance of these results.

2.1.1 Cell culturing method

Experimenting on biological cells is often delicate work and most cells require several fairly strict environmental conditions to be met to ensure they remain healthy and do not die for the duration of experiment. Almost all mammalian cells require a stable temperature of 37 °C and pH of 7.2 - 7.4. To this end, cells were grown in fixed temperature incubators which keep an atmosphere of 5% Carbon Dioxide (CO₂) to regulate the pH. Under these conditions cells move, grow and reproduce and to do this they require chemicals they can metabolise and consume. In the body of a typical mammal such requirements are met by the animal's circulatory system but in the laboratory the conditions can be sufficiently mimicked using a complex chemical medium, the bulk of which is derived from animal products.

This medium will contain an energy source such as glucose and/or citrate as well as several complex growth hormones, salts and chemicals that are commonly harvested from fetal stage calves or horses. An antibiotic is added to the medium to protect against contamination from undesirable lifeforms such as bacteria, yeast and other cells. Cell media are highly engineered solutions with several variations dependent on the cell line which is being cultured.

For this work I used a cell line known as NG-108-15 (referred to from now on as

NG-108) since they had been shown to be ideal for these types of experiments [114]. These cells were originally harvested from a mouse/rat neuroblastoma in the 1970's and were subsequently immortalised. Normally in mammals, cells are programmed to die when they reach a certain age, or when they divide a certain number of times, or when they find themselves in a part of the body they are not supposed to be in. This programmed suicide command is known as apoptosis and is vital to ensure the continued health of the host organism. Cells that have lost the apoptotic pathway through mutation or damage can become immortalised and grow out of control and form tumours, and this is commonly known as cancer.

NG-108's were cultured in Dulbecco's Modified Eagle's Medium (DMEM) (Sigma Aldrich UK) supplemented with 10% fetal calf serum (FCS) (Invitrogen, UK) and antibiotics (Sigma, UK) comprising of 18 units/ml of penicillin, 18 $\mu\text{g}/\text{ml}$ of streptomycin, and also 1.8 mM of L-Glutamine, in a humidified atmosphere of 5% CO_2 at 37 °C. The cells were cultured in a temperature controlled incubator at 37 °C and 5% CO_2 . At least 12 hours before experimentation the cells are plated onto a modified carrel flask [121](See Figure 2.1) or a sterile 35 mm petri dish. Previously, the petri dishes or flasks have been coated with a solution of 500 μl Optimem (Invitrogen, UK) 40 μl of laminin (L2020 Sigma, UK) and then hermetically sealed and left in the incubator for at least 12 hours. This allows the laminin to form a coating on the surface and the remaining solution is removed by pipette. Laminin coatings are used to create a favourable surface for the cells to grow on. 4 hours before experimentation the concentration of FCS in the medium is reduced to 1%.

This has the effect of encouraging the cells to differentiate which produces active growth cones [122]. The experimental dishes are hermetically sealed and placed onto a heated microscope stage for the experiments. These conditions ensure that the cells can remain healthy for a couple of days but experiments seldom lasted longer than 6 hours.

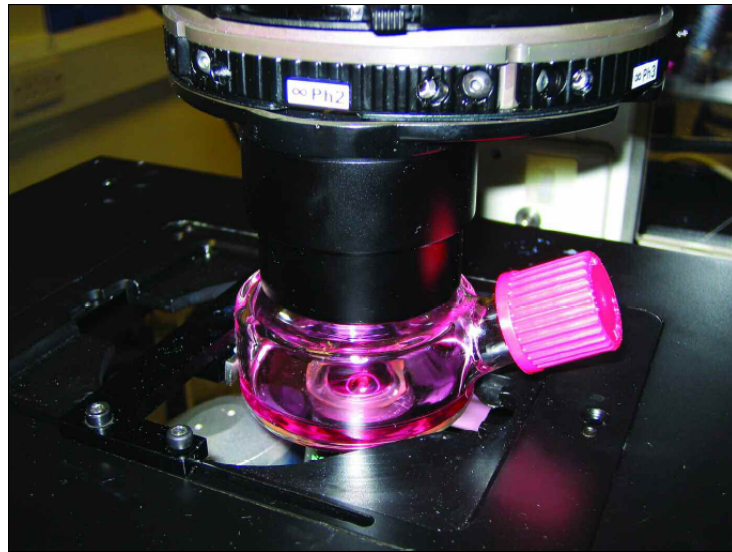


Figure 2.1: *Modified Carrel Flask with cells loaded in and sitting in experimental setup. This design also helped to solve a technical challenge in the latter part of chapter 4.*

2.1.2 Experimental setup

Figure 2.2 is a diagram of the optical train for this experiment. An approximately 1 mm Gaussian beam from a 1064 nm Nd:YAG laser (Photonics Innovation Centre) was expanded to approximately 6 mm in diameter using a 4f telescope consisting of a 50 mm and a 300 mm spherical lens. This telescope increased the beam width to approximately the same dimension as the back aperture of the microscope objective (Nikon phase contrast 60X Oil, 1.4 numerical aperture). The procedure for generating line tweezers was based on a technique used by Dasgupta et al [120] whereby

the incoming expanded Gaussian beam is focused through a 4f system consisting of a cylindrical lens of focal length 100 mm and then a spherical lens of focal length 100 mm, and then imaged on to the back aperture of the microscope objective. Essentially these lenses serve to elongate the beam in a single dimension before it is focused down through the objective. This creates a line profile at the sample plane of approximate dimensions $1\ \mu\text{m} \times 60\ \mu\text{m}$. To create the asymmetry in the intensity profile, the beam was partially truncated by a beam block at the second focus of the cylindrical lens resulting in an asymmetric beam of approximate dimensions $1\ \mu\text{m} \times 45\ \mu\text{m}$ at the focus plane (See Figure 2.2). This contrasts to the Dasgupta technique wherein they created the asymmetry by deflecting the line profile slightly off axis so that the objective itself truncated the beam.

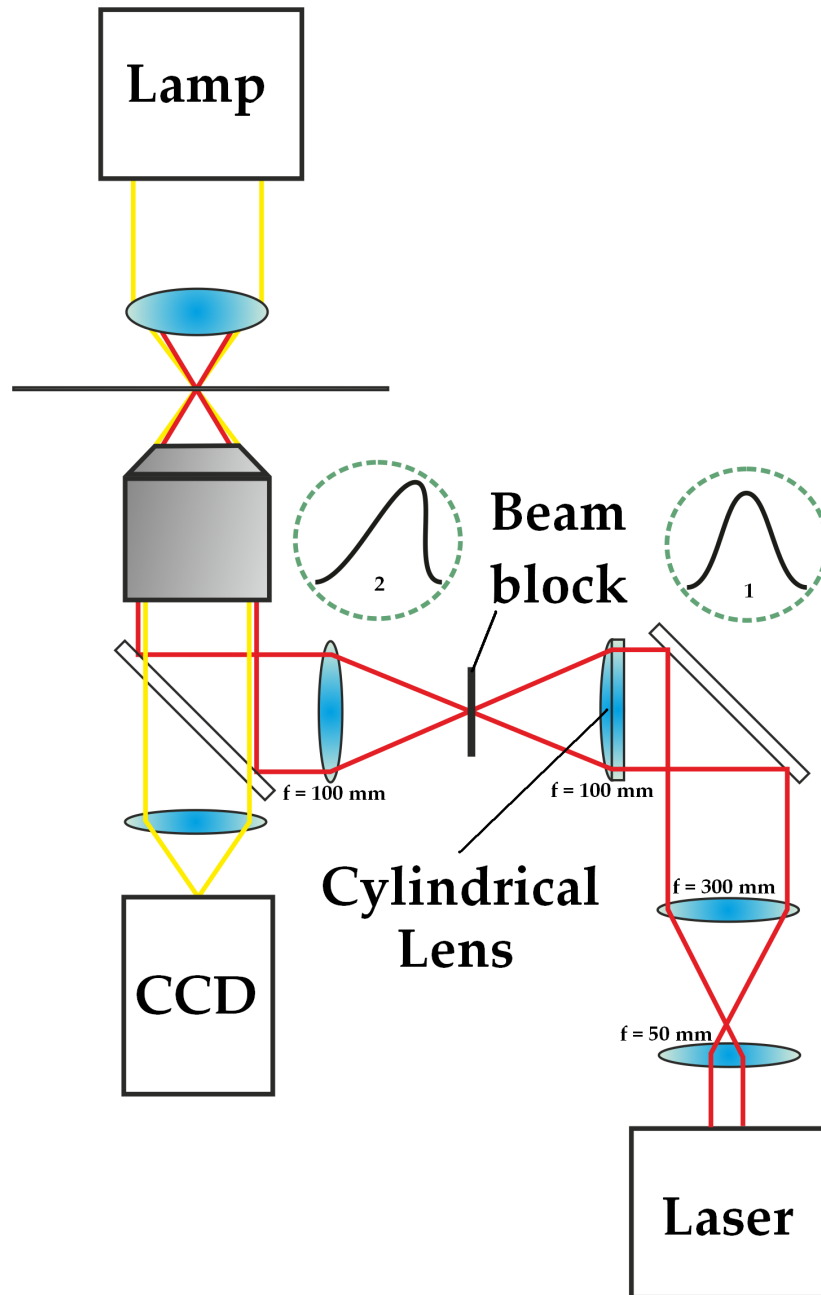


Figure 2.2: Diagram of experimental setup. The beam is expanded to 7 mm and then focused through a cylindrical lens. This elongates the beam in a single dimension resulting in a line shape that is then focused onto the back aperture of the objective. This results in a line shape at the focal plane. Also shown in this diagram is the method for creating asymmetry in the profile of the beam. This involves placing a beam block at the focus of the cylindrical lens and truncates part of the line shape (in this diagram the major axis of the line profile is perpendicular to the plane). This changes the overall length of the line and the intensity distribution along it. The change in the intensity distribution of the beam as it passes through the cylindrical lens and beam block is illustrated by a simple intensity plot in the green circles. Before the beam is Gaussian (circle 1) and afterwards becomes elongated and asymmetric (circle 2) in one dimension. These profiles are also illustrated in a contour plot in Figure 2.3 For symmetric intensity profile experiments two beam blocks at either side of the line were used.

Notably, the line was deliberately focused through the center of the objective to avoid effects resulting from the intense radiation pressure of focusing the center of the beam through the edge of the objective's back aperture (this effectively makes the objective itself the beam block; a method used in previous setups [116,120,123]). The symmetric line trap used as a control for the experiments was created by using a second beam block at the other side of the line to keep the major axis the same as the asymmetric line. The sample plane was imaged through a final mirror before the objective and onto a CCD camera (Watec, WAT-902DM). Images were captured on a PC using a custom program built on LabVIEW 8.2 (National Instruments). The microscope itself (Nikon Te-2000) was encased in a perspex box with a heating element to create a constant ambient temperature of 37 °C inside the box. The objective was also wrapped with a few turns of copper wire and a small current is applied in order to heat the objective upto 37 °C.

2.2 Experimental procedure and results

I will describe the different beam profiles that were used in this investigation and then detail the results of each configuration. Shown in Figure 2.3 is a diagram of the beam profiles rendered using Mathematica 5.2. The diagram shows how the line trap beam can be thought of as a Gaussian profile that has been elongated in a single dimension, it also shows the intensity profile of an asymmetric line trap compared to a symmetrically profiled line trap. I will briefly explain the terms 'forward' and 'reverse' bias before detailing the results of this investigation.

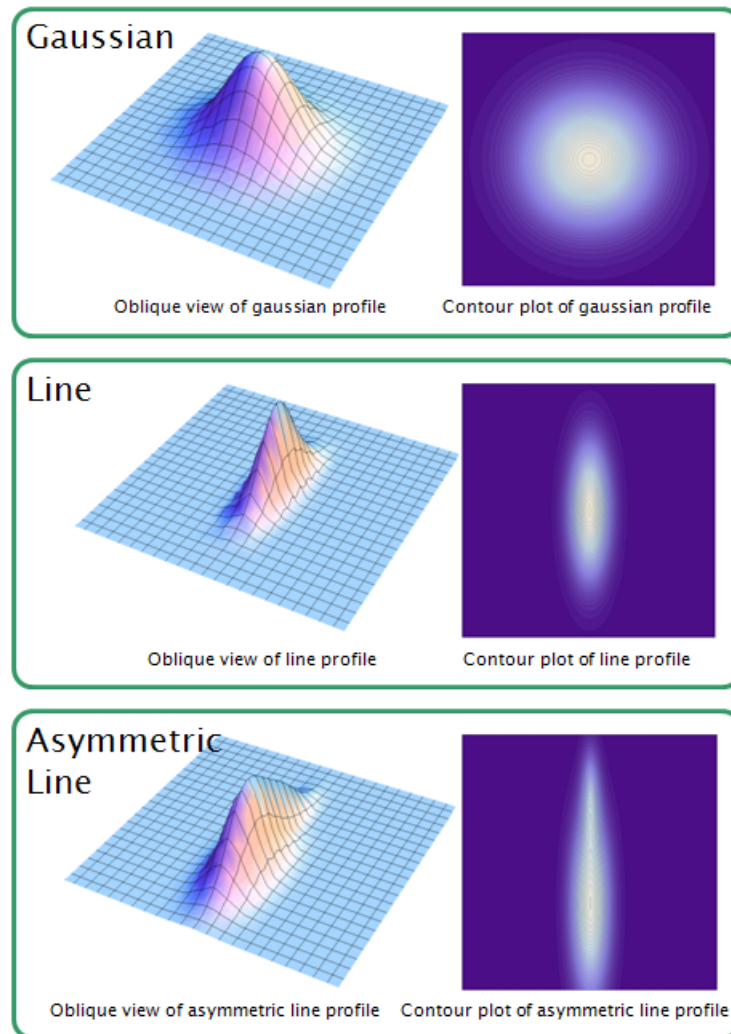


Figure 2.3: Diagram showing the intensity profiles of the different beam configurations used in this experiment and a Gaussian profile for comparison (not to scale). Left: Oblique view, Right: Contour plot.

2.2.1 Explanation of ‘Forward’ and ‘Reverse’ bias configurations

As can be seen from Figure 2.3 the asymmetric profile has the most intense region of the beam displaced from the spatial centre of the beam. In terms of a potential well, what we have is a steep slope opposite a gentle slope. In the study by Mohanty et al [116], it was asserted that microparticles entering the line trap from the steep end would gain so much kinetic energy from the high optical gradient that they

would be catapulted out along the gentle gradient in a “sling-shot” like process. The reason for this assertion was to link it to the previous work by Ehrlicher et al [114] who built a mathematical model based on actin monomers in an optical trap.

Actin, as described in Chapter 1, is the essential molecule involved in a developing growth cone, and the theory that Ehrlicher et al had previously reported was that the optical forces of the Gaussian beam were pooling actin monomers towards the centre of the beam where it was presumed to be polymerising into actin filaments and thus the growth cone advanced in this direction [114]. Mohanty et al used their microparticle “sling-shot” concept to imply that actin was being “sling-shotted”, and this was therefore why the line trap could bias the direction of neuronal growth (the actin was only flowing in one direction, from the steep optical gradient to the gentle optical gradient and then beyond). In the Mohanty et al experiments, they positioned the steep part of their line tweezers onto the cell membrane (with the shallow end pointing away from the cell) and claimed that the cell then grew along the major axis from steep end to shallow end because of this “sling-shot” effect. This configuration was investigated in our study and we termed it ‘forward bias’ (i.e. this beam would bias the cell to grow forward).

If, however, we accept the premise of the Mohanty ‘sling-shot’ model, then presumably if we rotated the beam 180 degrees around the axis perpendicular to the plane (i.e. place the steep end of the line trap at the edge of the membrane but have it pointing into the cell instead of out of it) then the actin monomers should flow away from the membrane edge, leading to a depletion of actin at the leading edge,

which presumably would lead to a lack of developing actin filaments at this edge ultimately resulting in this edge retracting. This retarding configuration we termed ‘reverse bias’. A diagram of these two configurations can be seen in Figure 2.4.

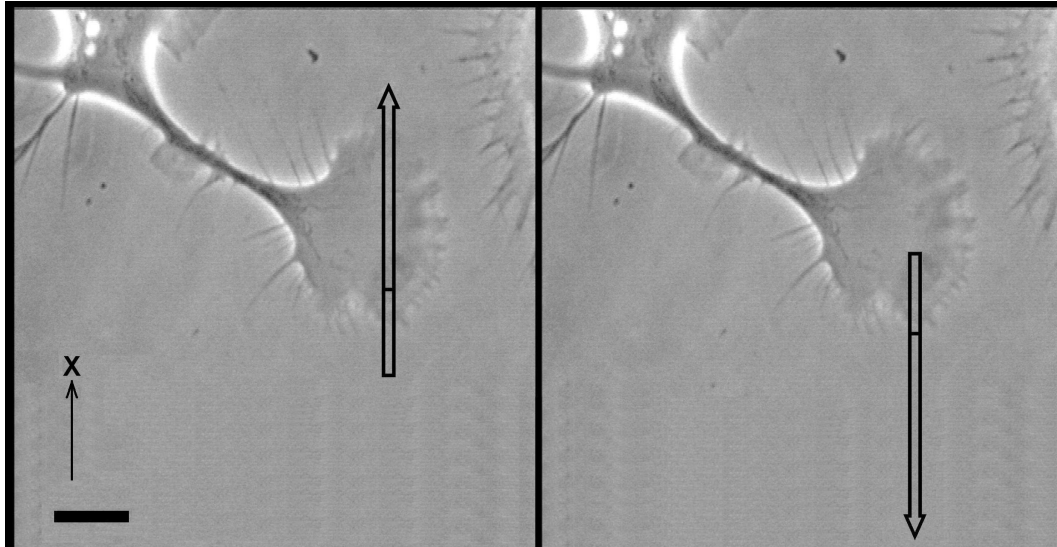


Figure 2.4: *Illustration of ‘forward’ (right) and ‘reverse’ (left) bias beam configurations. A growth cone is shown with an arrow which represents the position and orientation of an asymmetrical line trap. The line dividing the arrow in two marks the location of the deepest part of the potential well and the arrow points in the direction that the Mohanty ‘sling slot’ model predicts the neuron should grow in. For example, the left configuration would be expected to retard the growth along the x direction whilst the right configuration would be expected to encourage growth along the $-x$ direction. The scale bar is $10\ \mu\text{m}$.*

2.2.2 Description of laser application

Using the beam in the forward bias configuration (i.e. the same configuration Mohanty et al used [116]) I conducted experiments designed to facilitate optically guided neuronal growth. This was done first by using the microscope to scan manually the sample chamber for an active growth cone. This growth cone was then monitored for at least 5 minutes to determine if it was actively growing. Cells that were not observed to be actively growing before application of the laser beam were not experimented upon. If it was active, then the laser beam was applied such that the major

axis of the line trap was always orientated along the direction of desired growth (not the initial direction the neurite was growing in, but at an angle $\geq 20^\circ$ from this direction) and that the edge of the growth cone was always illuminated by the part of line with the steepest optical gradient. This configuration was maintained by manually adjusting the position of the beam as the neurite grew and developed. If the active growth cone was observed to align and grow along the major axis of the line trap (which involves a directional change of at least 20°) it was considered a successful result. If after ten minutes of irradiation the growth cone, which was previously determined to have been active, either did not respond or retracted, it was considered an unsuccessful result. Successfully guided growth cones tended to continue growing for about 20-30 minutes with laser application, though after this time they began to stall and sometimes retract though this was consistent with previous optically guided neuronal growth experiments [114, 116, 117].

For the reverse bias configuration, since the theory implied by Mohanty et al was that actin monomers would be accelerated along the major axis of the line profile from the steep gradient and out through the shallow gradient, then by placing the beam so that the actin flow would be predicted to be repelled from the leading edge, should retard growth (as shown in Figure 2.4). This configuration was applied using the same procedure as outlined in the last paragraph. The procedure was also carried out for a line trap with no bias in its profile i.e. a symmetric intensity profile as seen in Figure 2.3 (Line).

Measurements taken included whether or not the growth cone was successfully

guided by the laser, and the properties of this growth including the rate of growth (measured by taking an average of the distance travelled in successive frames over the period of irradiation) and the change in the initial direction the neurite was growing (as measured by comparing the angular difference between the neurite in the frame immediately preceding laser application and the frame immediately succeeding laser application).

2.2.3 Results

Shown in Table 2.1 are the numerical results from this investigation for the different beam configurations.

| Bias | Forward (n=34) | Reverse (n=38) | None (n=37) |
|--|----------------|----------------|--------------|
| Guidance | 8 (24%)* | 8 (21%)* | 7 (19%)* |
| Avg. growth rate ($\mu\text{m}/\text{h}$) | 65 ± 11 | 78 ± 9 | 111 ± 11 |
| Growth rate range ($\mu\text{m}/\text{h}$) | 27-123 | 46-122 | 51-136 |
| Avg. direction change | 26 ± 9^0 | 19 ± 4^0 | 20 ± 5^0 |
| Greatest direction change | 76^0 | 38^0 | 40^0 |

Table 2.1: Results of different line trap configurations. * Non significant difference between these beam configurations (Mann-Whitney test, $p < 0.05$). Averages are $\pm \text{SEM}$ (standard error from mean). The full set of data used to construct this table is included in the appendix to this thesis.

What is evident from the results in table 2.1 is that all the beam configurations show approximately the same rate of success and similar growth properties (rate, direction change). Indeed, in configurations that were designed to retard growth (reverse bias) as implied by the “sling-shot” model, we have established that growth actually increases with similar efficiency as a growth promoting configuration (forward bias) of the beam. These results strongly suggest that the “sling shot” concept is flawed and a more exact model is needed to explain the behaviour of growth cones

under laser irradiation.

For direct comparison, I have singled out one example of successful guided growth for both a forward, and a reverse, bias configuration and show them side by side in Figure 2.5. This figure is an image sequence showing the stages of the developing growth cone at 5 minute intervals. Due to the changing field of view it was necessary to include an outline of the shape and position of the neurite in the previous frame. As can be seen, the growth cone is attracted to the laser and advances and changes direction accordingly. Of note is the reverse bias configuration (right side of Figure 2.5) where it can be seen that growth cone advances against the supposed direction of actin flow according the Mohanty ‘sling-shot’ model. If the ‘sling-shot’ model were accurate then the growth cone would be expected to be repelled towards the bottom of the image but, crucially, I observed the opposite.

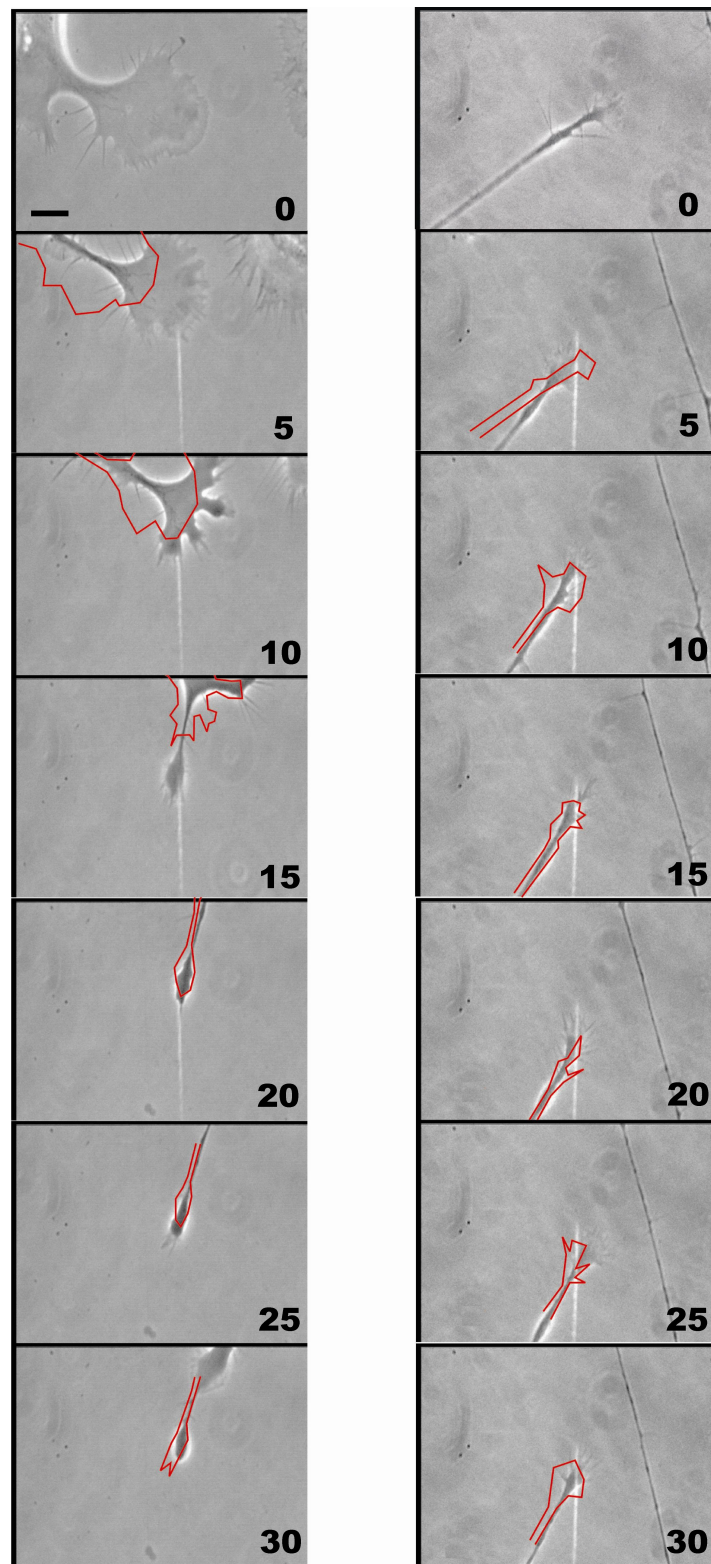


Figure 2.5: Image sequence showing successful guidance for a forward (left) and a reverse bias (right) configured line trap. Images flow from top to bottom and successive frames are separated by 5 minutes. The total elapsed time is shown in the bottom right hand corner of each image. The position of the neurite in the previous frame is shown in the current frame as a red outline. Of note is that in the first two frames of the left sequence some microtubules are visibly moving towards the point of laser irradiation. The scale bar is 10 μm .

2.3 Mathematical model

Since the Mohanty “sling-shot” model was incapable of explaining my results, a new approach was necessary. To this end I assisted my colleague Dr Michael Mazilu in developing a new model to help explain the behaviour we observed. Since I did not think that the actin monomers were being sufficiently influenced by the optical forces of the beam (as the previous literature had suggested [114,116]) and additionally my observations of growth cones under the influence of line traps had cast serious doubt on the “sling-shot” model of actin flow, I therefore decided to focus the investigation on another hypothesis that attempted to explain the phenomenon of optically guided neuronal growth. Specifically, it was proposed that actin filaments were the principle mechanism behind the optical guidance. As mentioned in the previous chapter, actin filaments are the principle mechanism behind cell growth and motility [58]. Actin filaments are attached to the substrate via transmembrane CAM’s and ankyrin linker proteins. The polymerisation of actin monomers at the leading growing edge of the cell drives the filament to advance the membrane [72]. These filaments protrude quite visibly from membrane and Dr Mazilu and myself supposed that when these filaments first begin to protrude (and, crucially, before they affix themselves) they would be susceptible to any optical forces present at that time. Unknown to us at the time, this mechanism had already been proposed in the literature [124], but it was never followed up with an investigation. Since we were building our model on the previous work of Ehrlicher et al [114], their approach will be discussed in more detail.

2.3.1 The original approach by Ehrlicher et al

The explanation proposed by Ehrlicher et al in 2002 [114] modelled the optical forces on a single actin monomer. First, they modelled actin monomers as dielectric spheres of radius $a_{\text{act}} = 3$ nm and refractive index $n_{\text{act}} = 1.59$ [125–127]. Then they proceeded to calculate the dipole potential on their model monomer due to the presence of a focused laser beam, working from equation 2.1 originally derived by Harada and Asakura [14]:

$$F(r)_{\text{dipole}} = \langle |p| \nabla |E(r, t)| \rangle_{\text{timeaverage}} = \frac{1}{4} \alpha \nabla |E(r)|^2 = \frac{\alpha \nabla I(r)}{2n_{\text{cyt}} \varepsilon_0 c} \quad (2.1)$$

Where $p = \alpha E$ is the dipole moment, α is the polarisability of the actin monomer and $n_{\text{cyt}} = 1.37$ is the refractive index the cytoplasm [128], ε_0 is the vacuum permittivity and c is the speed of light in a vacuum. $I(r)$ represents the Gaussian intensity profile of their laser beam. This equation is the time average of Equation 1.3 from Chapter 1.

Integrating this equation over r gives the dipole potential:

$$U(r) = \frac{\alpha I(r)}{2n_{\text{cyt}} \varepsilon_0 c} \quad (2.2)$$

In order to solve this equation they needed to calculate α and they did this using the Clausius-Mossotti equation (equation 2.3) for dielectric particles as described by Rohrbach and Stelzer [129]:

$$\alpha = 4\pi\epsilon_0 a_{act}^3 n_{water}^2 \frac{(m^2 - 1)}{(m^2 + 2)} \quad (2.3)$$

Where $n_{water} = 1.33$ is the refractive index of water and $m = n_{act}/n_{water}$ (it is unknown why they have used the refractive of the cytoplasm for Equation 2.1 but used the refractive index for water here). Solving this equation yields a polarisability of $\alpha \approx 6.5 \times 10^{-37} Cm^2/V$ which, with their Ti:sapphire laser ($\lambda = 800$ nm) of beam power 60 mW and a beam radius at focus of 1.5 μm , subsequently yields a dipole potential at the centre of the laser beam of $U = 1.5 \times 10^{-24} J = 3.6 \times 10^{-4} k_B T$ where k_B is Boltzmann's constant and $T = 310$ K is temperature of the cell in Kelvin. As evident, the potential well is about 4 orders of magnitude less than the thermal energy $k_B T$ and is thus unable to satisfy the Boltzmann factor $\exp[-U/k_B T] \ll 1$ which means this beam is too weak to optically 'trap' actin microspheres as their Brownian motion is more than enough to overcome this force (Ashkin suggests that a factor of $U \geq 10k_B T$ is needed for a good trap [3]). This is in contrast to the claim by Mohanty et al [116] that a similarly powerful laser beam can not only trap but actually 'sling-shot' actin monomers. However, Ehrlicher et al theorise that this optical force could increase the diffusion of actin monomers toward the centre of the beam and that this increased diffusion is responsible for increased polymerisation of actin monomers at the beam site and thus explains why the growth cone advances towards the laser beam. Indeed they estimated the drift velocity of actin monomers towards the beam by approximating $F(r)_{dipole}$ to be constant over all r with the value of $F(r)_{dipole}$ at half the beam radius and then using equation 2.4:

$$v_{drift} = F_{dipole}/\xi \quad (2.4)$$

Where $\xi = k_B T/D$ and $D \approx 2.5 \times 10^{-11} m^2/s$ is the estimated diffusion coefficient for an actin monomer [130]. Using this equation, Ehrlicher et al predicted a drift velocity of 26 $\mu m/h$ for actin monomers which, they note, is very close to the growth rate they reported for successfully guided growth cones of $37.5 \pm 22.5 \mu m/h$ under the influence of their laser.

2.3.2 My filopodial approach

The Ehrlicher approach seems at first to be a satisfying explanation of this phenomenon. However, it predicts a very weak optical effect and despite a good explanation in terms of drift velocity, it does not explain the growth rates I observed on the same cell type of upto 130 $\mu m/h$ nor does it explain the observation that filopodia can align themselves with the beam as they protruded from the membrane [115].

However the initial premise of modeling actin as a dielectric sphere appeared reasonable and so we decided to build upon this and model the optical forces on the large actin filaments that protrude from the membrane (also known as filopodia). This intuitively seemed sensible as polarisability increases with molecular size and thus these filaments will experience a much deeper potential well when compared to monomers for similar beam powers.

Initially we used the derivation for the time-averaged total force on a dielectric sphere in an electromagnetic field developed by Chaumet and Nieto-Vesperinas [16]

(equation 2.5) as opposed to the one developed by Harada and Asakura [14] which was used by Ehrlicher et al. This was because the Chaumet derivation took into account the absorptive and radiative scattering forces that are necessarily exerted on microparticles in an electromagnetic field whereas the Harada and Asakura equation only considers the gradient force.

$$\langle \mathbf{F}_i \rangle_{timeaverage} = \frac{\varepsilon_o n_{water}^2}{2} Re(\alpha \mathbf{E}_j \partial_i \mathbf{E}_j^*) \quad (2.5)$$

Where the star stands for the complex conjugate and where we implied summation over repeating indices. We then calculate the polarisability α_0 by first using the Clausius-Mossotti equation (equation 2.3) like before but then, crucially, we correct this for the radiative reaction term (described by Draine [131]) giving the true polarisability, α , in equation 2.6.

$$\alpha = \frac{6\pi\alpha_0}{6\pi - in_{water}^3 k_0^3 \alpha_0} \quad (2.6)$$

Where $k_0 = 2\pi/\lambda$ is the vacuum wave-vector and i is the imaginary unit. We then sum this new equation for the dipole force on a dielectric microparticle over an entire filopodia using Mathematica 5.2 (Wolfram). Before we do that however we must build up what a filopodia is structurally. Consulting the literature [132–134] we assumed that an individual actin filament consists of actin dimers in helical arrangement with a 74 nm pitch containing 14 dimers as shown in figure 2.6. A filopodium consists of a bundle of approximately 20-30 of these filaments in parallel, and is upto 2 μm in length as well as a membrane sheath and associated transmembrane

proteins. For our model filopodia we focused entirely on the actin filaments since they are the main component of a filopodia and we specifically considered 25 actin filaments separated from each other by 10 nm in a 5 x 5 lattice and 2 μm in length. This structure consisted of approximately 19,000 individual actin monomers. To complete our model, we fixed the filopodia at one end (to mimic the part of the filopodia that is in the cell membrane) and left the other end free to rotate around this pivot as it would in response to stimuli in nature.

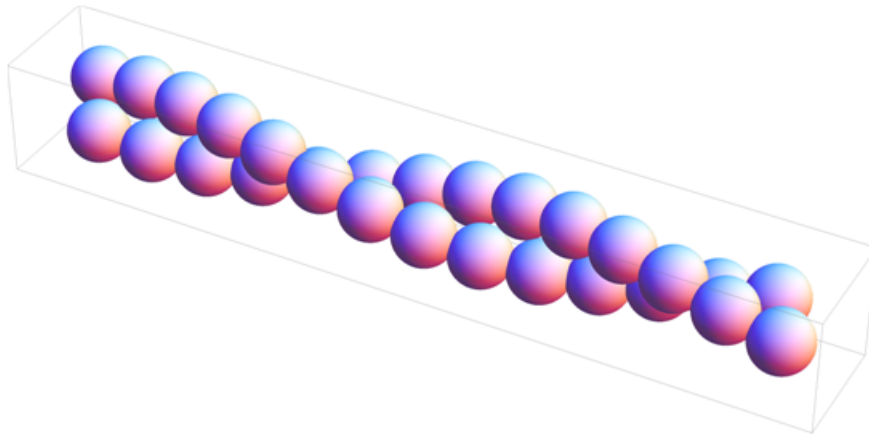


Figure 2.6: *Diagram of our actin filament model rendered using Mathematica 5.2 (Wolfram). Each sphere is modelled as having a radius of 3 nm*

With our structure complete, we summed the optical force for two different beam configurations (a Gaussian and a line profile) over the entire structure as if the focused beam was incident upon the far end of our filopodia model. As the filopodia were free to rotate, we plotted the optical torque on the structure as a function of the angle the filopodia makes with respect to the centre of the beam. Figures 2.7 and 2.8 show the optical torque due to a Gaussian beam and a Line profile beam respectively.

What is immediately noticeable is that the shape of the curve in Figure 2.7 is

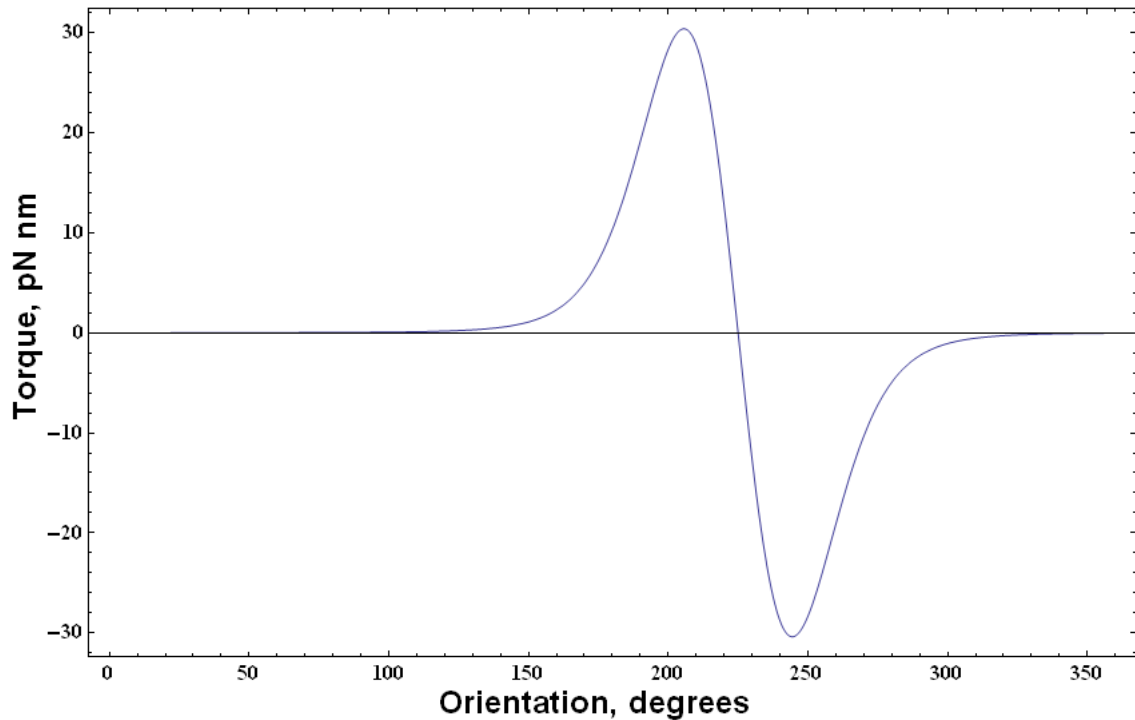


Figure 2.7: *Plot showing how the torque (measured in piconewton nanometres) on the filopodia due to the optical force varies as the filopodia is rotated through a full 360 degrees with respect to the centre of a Gaussian beam of diameter $1.5 \mu\text{m}$ and power 20 mW .*

the gradient of a Gaussian curve. Since the optical potential well in this case is of a Gaussian nature it is expected that the force (or its rotational equivalent of torque in this case) would follow that of the gradient of a Gaussian because the derivative of the potential with respect to displacement is the force as a function of displacement (or its rotational equivalent of angle in this case). What this curve shows is that there are two orientations where the torques are balanced (the two points where the curve crosses the x-axis) which is exactly what we would expect since these two orientations correspond to the filopodia pointing directly towards and away from the beam centre. However, the orientation pointing away from the beam centre is only metastable (analogous to a clock pendulum pointing straight up for example) and in practice, only the orientation point directly toward the beam

centre will be stable. This means that the filopodia will experience a significant optical torque and will seek to align itself to point towards the centre of the beam at which point the torques will balance. Any deviation from the centre point will result in a restoring torque entirely equivalent to the restoring optical force felt by dielectric microparticles in optical tweezers. The Gaussian beam modelled for this curve was a diameter $1.5\ \mu\text{m}$ and a power $20\ \text{mW}$ which are typical values for these experiments [117]. It is important to note that the initial orientation of the filopodia (zero degrees on the plot) was pointing left along the horizontal and that the beam is positioned $0.25\ \mu\text{m}$ below and parallel to the filopodia (this is why the stationary points are not exactly 0 and 180 degrees). This was done so as to simulate a general case of a filopodia being in the presence of a beam and to deliberately avoid the special case where the filopodia begins in the exact centre of the beam.

Figure 2.8 is the same plot of torque as a function of orientation but for a line laser beam profile of dimensions $1\ \mu\text{m}$ by $45\ \mu\text{m}$ and a total power of $70\ \text{mW}$. The curve is of the same shape of that in Figure 2.7 but with two periods. As before the filopodia is initially pointing left along the horizontal (zero degrees) and the beam position is $0.25\ \mu\text{m}$ below and parallel to the filopodia. The reason that there are two stable points and not one is due to the shape of the filopodia and the shape of the beam. There are only two ways a rod-like structure can sit in a long thin valley: either parallel or anti-parallel. If the beam were positioned along the horizontal with the filopodia and extended slightly behind the filopodia (as it was in our experiments) then the two stationary points would be at exactly 0 and 180 degrees. If the beam

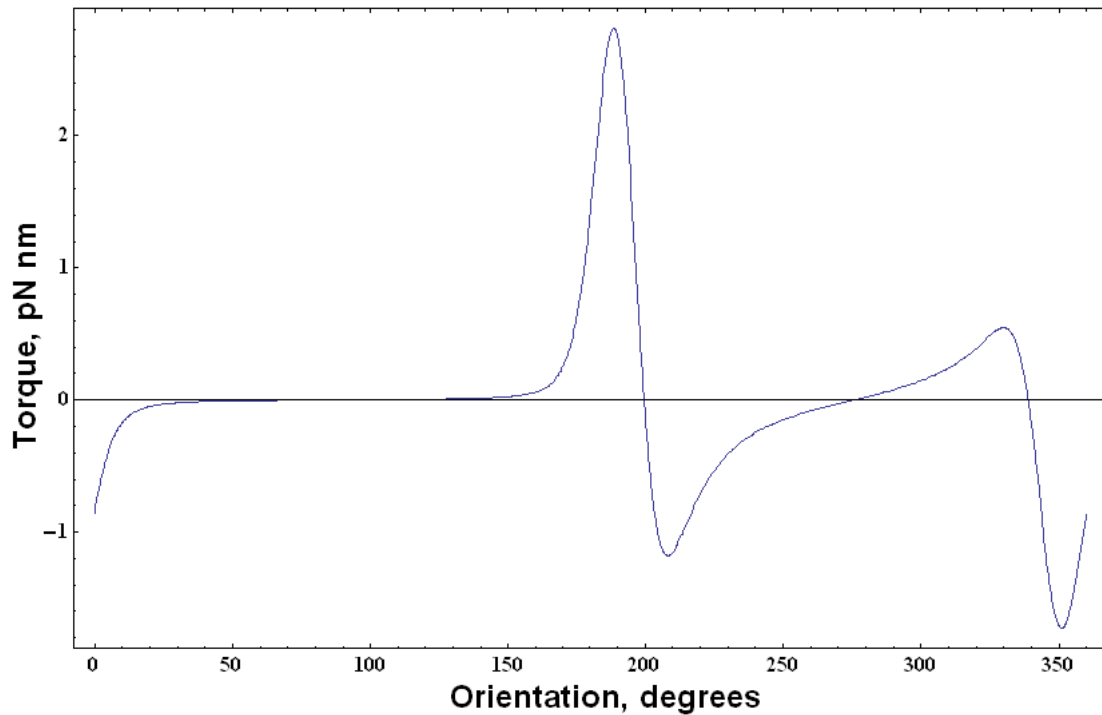


Figure 2.8: *Plot showing how the torque (measured in piconewton nanometres) on the filopodia due to the optical force varies as the filopodia is rotated through a full 360 degrees with respect to the centre of the line profile beam of dimensions $1\ \mu\text{m}$ by $45\ \mu\text{m}$ and power $70\ \text{mW}$.*

were positioned perpendicular to the filopodia then the behaviour would be similar to that of a Gaussian with only a single stationary point (pointing towards the beam centre), but this configuration was not used in my experiments. Since our model aims to demonstrate a general case, the beam was positioned parallel to the filopodia but with a slight vertical displacement, which is why the two stationary points are not separated by exactly 180 degrees. This is an explanation for the observations I made on the effects of forward and reverse biased beam configurations, since this indicates that the filopodia would align themselves to the major axis of the beam, regardless of whether they are pointing towards or away from the deepest part of the optical well. In fact, of the two available stationary points, the one pointing more towards the deepest part of the beam will have stronger restoring torques, than the

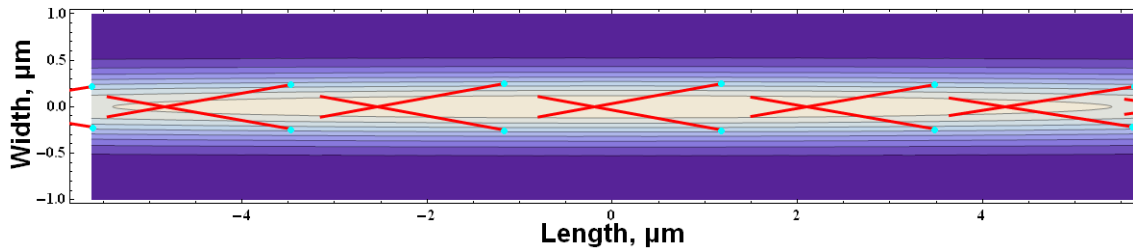


Figure 2.9: *Diagram illustrating the equilibrium positions for filopodia (red lines) originally pointing left with respect to a fixed pivot point (blue dots) under the influence of an line profile laser beam (purple contrast plot).*

other one, implying that in cases where the deepest part of the beam was outside the cell membrane (i.e. the reverse bias configuration) then the optical torques would be stronger. This would imply that the effect of the filopodia lining up would be slightly stronger than the other case (although it must be stated that I've seen no observational evidence for this). This is essentially the exact opposite of what the Mohanty 'sling-shot' model predicted.

Another way to represent this is seen in Figure 2.9. In this figure Mathematica has been used to illustrate how several of our filopodia will rotate in the presence of a line profiled laser. Our model filopodia are represented as red lines with a blue dot at one end to represent the fixed pivot point. They are shown overlain a contrast plot of the laser intensity profile and are shown in their final position (where the torques are balanced) after beginning in their initial position pointing left along the horizontal. As can be seen, they have all orientated themselves to point into the well, and none of them have reversed direction to point towards the deepest part of the well (the centre of the beam in the diagram).

With a new model of what is physically happening to filopodial structures under the influence of a laser beam I can therefore explain all of the observational data I

have gathered during these experiments. The reason there is no statistical difference between any of the line profile configurations is because they all exert the same effect on the filopodia, namely that of inducing an unbalanced torque until the structure lines up with the major axis of the line profile and, crucially, this is regardless of any asymmetry in the beam. This explanation is further supported with observational evidence of filopodia rotating to bring themselves in line with an applied laser beam as seen in Figure 2.10.

For comparison to the Ehrlicher approach I have also calculated the maximum depth of the optical potential for both beams. The line profile beam has a maximum optical potential depth of $U = 1.66 \times 10^{-21} J = 0.39 k_B T$ and the maximum potential of the Gaussian beam is $U = 6.09 \times 10^{-20} J = 14.24 k_B T$ for $T = 310\text{K}$. As can be seen, these values are much larger than the value originally calculated by Ehrlicher et al ($U = 1.5 \times 10^{-24} J = 3.6 \times 10^{-4} k_B T$) [114] and, in the case of the Gaussian beam, is high enough to satisfy $\exp[-U/k_B T] \ll 1$ and $U \geq 10 k_B T$. Which means our model predicts that there is sufficient optical force to truly optically trap the filopodia, with the Gaussian beam exerting a stronger pull than the line profile.

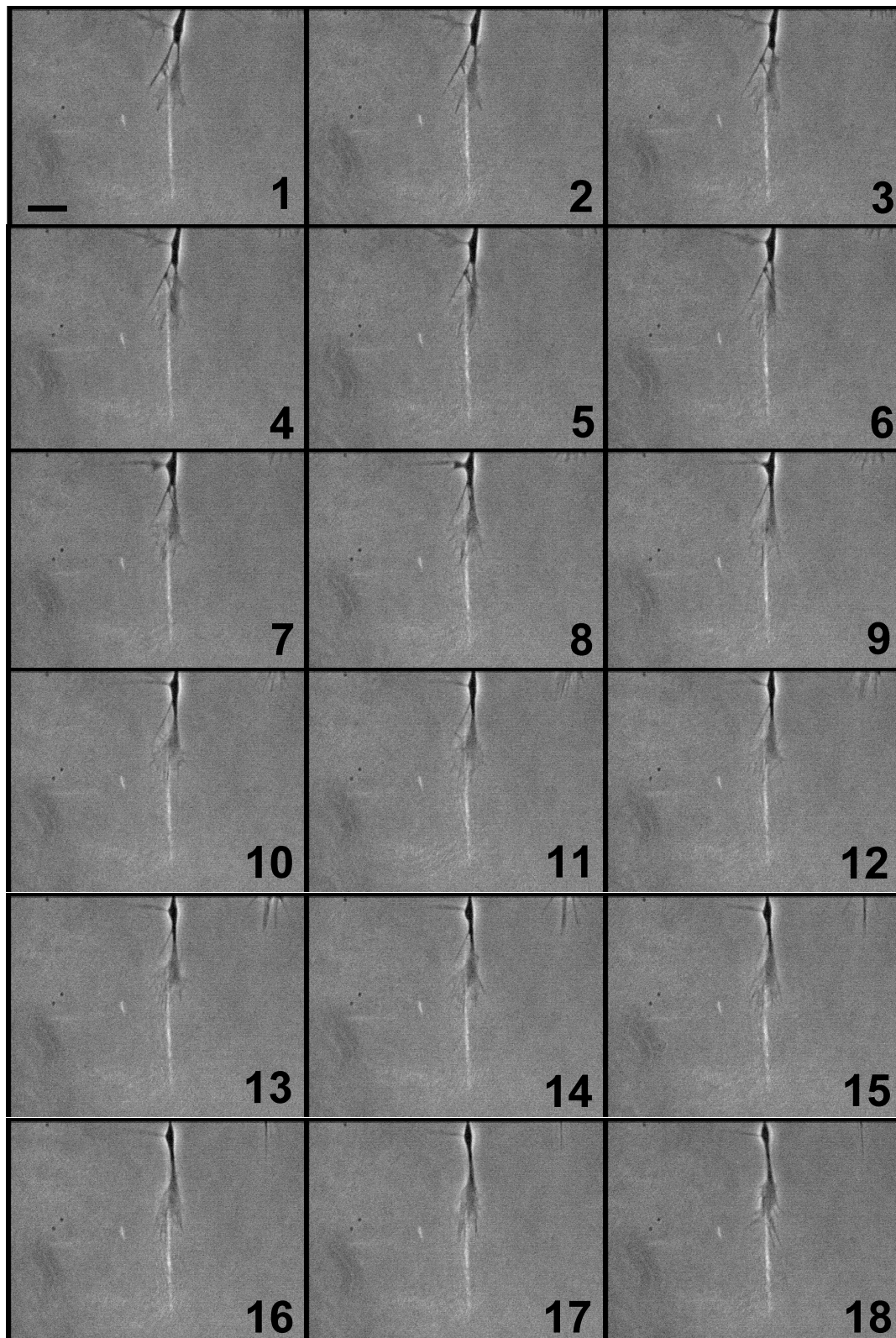


Figure 2.10: Image sequence showing individual filopodia orientating themselves in the presence of a line profile laser beam. The frames are 25 seconds apart and flow from left to right top to bottom. Scale bar is 10 μm .

2.4 Conclusion and discussion

In this chapter, I have explained the use of optical line profiles in neuron growth studies and presented data comparing them with the more widely used Gaussian profile. A previous study by Mohanty et al [116] had suggested that line profiles offer a greater degree of control over Gaussian beams and this provided the started point for my experiments.

As the data in Table 2.1 shows, there is no statistical difference between different configurations of line intensity profiles for neuronal growth as implied by Mohanty et al. The work published by Mohanty et al suggested that this should not be possible since the asymmetry in the beam profile was providing a bias to the flow of actin. It is also important to note that the experiments carried out by Mohanty et al were performed at room temperature (~ 25 °C) on mammalian N15-115 cells which should be kept at 37 °C. This could result in a temperature dependent effect which may have influenced their results in a way the authors did not account for.

Therefore, my experiments detailed in this chapter were the first to investigate the effects of asymmetrical line profile beams on optically guided neuronal growth using appropriate controls and experimental conditions. Under these conditions, there is no discernible effect on the neuron due to the bias of the beam profile (forward or reverse).

The mechanism suggested by Mohanty et al was based upon an interesting approach of describing optical wells as “sling-shots” for actin monomers. This itself is based upon the earlier work of Ehrlicher et al [114] who developed a model of actin

monomers flowing towards the site of irradiation due to optical tweezing effects. However, the Ehrlicher model only predicted an optical potential of $3.6 \times 10^{-4} k_B T$ i.e. low enough so that Brownian motion would easily overcome the force of the trap.

Therefore a new approach was needed to better explain how optically guided neuronal growth worked and to explain the observations in Table 2.1. To this end I have recreated the model here that was originally developed by my colleague Dr Michael Mazilu with my assistance for the original publication of this work. Our approach shows a much stronger effect when we think in terms of whole filopodial structures instead of individual actin monomers. Our model was applied to both Gaussian and line profile beams with the expected result of one stationary point for a Gaussian beam but two stationary points for the line configuration as shown in Figures 2.7 and 2.8. This predicts that filopodia will fall into their nearest stationary point whether or not this happens to be pointing towards or away from the deepest part of the optical well as seen in Figure 2.9. This explains why there is no significant difference between forward and reverse bias line profile beam configurations. This model also explains observations that appear to show filopodia aligning themselves with the major axis of the line profile as seen in Figure 2.10. Our model also shows that filopodia will experience a much deeper potential well than individual actin monomers. Our model calculates a maximum optical potential of $U = 1.66 \times 10^{-21} J = 0.39 k_B T$ for the line profile beam and $U = 6.09 \times 10^{-20} J = 14.24 k_B T$ for the Gaussian beam.

To do a direct comparison with the Ehrlicher approach I recalculated the potential for the slightly more powerful Gaussian beam that they modelled in their calculation (60 mW compared to our 20 mW) and this nets a value of $U = 1.83 \times 10^{-19} = 42.78 k_B T$ which is more than 5 orders of magnitude larger than their calculated potential of $U = 1.5 \times 10^{-24} J = 3.6 \times 10^{-4} k_B T$ and, crucially, is more than the thermal energy $k_B T$ at room temperature. This shows that the model predicts optical forces strong enough for actual trapping and not just a biased diffusion as was originally predicted by Ehrlicher et al. The approach of using bundles of actin filaments as the main structure involved in optically guided neuronal growth has successfully explained the observations I have made and suggests that the primary mechanism for this phenomenon is optical trapping of filopodia.

It is worth reiterating that our model of 25 actin filaments in a bundle is not a filopodia in the real world. A real filopodia does contain roughly this number of filaments in roughly the pattern we've described, but there are other components such as a plasma membrane sheath and various transmembrane and linking proteins. Although the actin filaments are the main component, a more exact model could be devised by taking into account all the components that form a real filopodia.

Chapter 3

Development of an automated experimental setup

3.1 Introduction

In this chapter I will describe how I automated the process of optically guided neuron growth. This was achieved through a combination of novel hardware and software such that it was possible to automatically steer a laser beam on to a defined position on a developing growth cone to induce its guidance towards a user-inputted target point.

Previously, the necessary steering adjustments needed in these experiments had been done manually. This could either be done by appropriately tilting a steering mirror in the conjugate plane of the microscope objective or by translating the sample stage on the microscope along the x and y axes. Since a developing growth cone can move at over 100 microns per hour across the field of view it was necessary to continuously

adjust the beam position to keep up with the leading edge which was operationally difficult since a typical successfully guided growth cone can grow uninterrupted for up to 30 minutes (after which time laser guided growth stops). The development of a system which can do this manual task automatically was therefore desirable.

In 2005, software developed by Stuhrmann et al [135] using LabVIEW was shown to detect the edges of developing growth cones and then, using an Acousto-Optic Deflector (AOD), this information was used to steer a laser beam in the appropriate position to induce successful guidance.

Using similar principles, and beginning with their software as a model, I developed a LabVIEW program to work on a setup which was designed to make use of a Spatial Light Modulator (SLM) instead of an AOD for the beam steering and beam shaping. I will detail the use of the SLM to induce neuronal guidance using a Gaussian beam, a line profile beam and a Bessel beam that culminated in my 2009 publication “Automated laser guidance of neuronal growth cones using a spatial light modulator” [136]. Included in this chapter will be a discussion on the merits of using a SLM over an AOD and the theory behind both as well as a detailed description of operation of the LabVIEW program and a discussion of it’s capability.

3.2 Spatial Light Modulators

3.2.1 Introduction to Spatial Light Modulators

Strictly speaking, a spatial light modulator (SLM) is anything that applies a spatially varying modulation on an incoming beam of light. In this respect, an overhead

projector transparency is an example of an intensity varying spatial light modulator. In the last few decades, commercial SLMs have been commonly found in display projectors in the form of small liquid crystal displays (LCD) with resolutions comparable to PC monitors. In the field of optical trapping, SLM's are used to modulate the intensity and/or the phase of an incoming laser beam and can be used to create what is known as holographic optical tweezers (HOT) by operating in the Fourier image plane.

The first example of a SLM being used to create optical traps (the first HOT setup) was by Reicherter et al in 1999 [137] which they accomplished by harvesting a LCD from a display projector and incorporating it into the Fourier plane of a standard optical tweezers setup. They were able to create three independent optical traps by programming the SLM LCD to display an appropriate hologram. They also demonstrated the ability of SLMs to beam shape by creating TEM_{01} beam shapes (doughnut shaped) from an incident Gaussian (TEM_{00}) beam which they used to optical tweeze polystyrene microparticles. By 2002, Curtis et al [138] had demonstrated full dynamic control of beam shaping in three dimensions. Before proceeding it will be useful to understand the theory behind the holograms which allow SLMs to create holographic optical tweezers.

3.2.2 Fourier optics and Spatial Light Modulators

Lenses and objectives in optical systems can be thought of as Fourier transformers. For example consider Figure 3.1 where a spatially varying pattern is placed at the

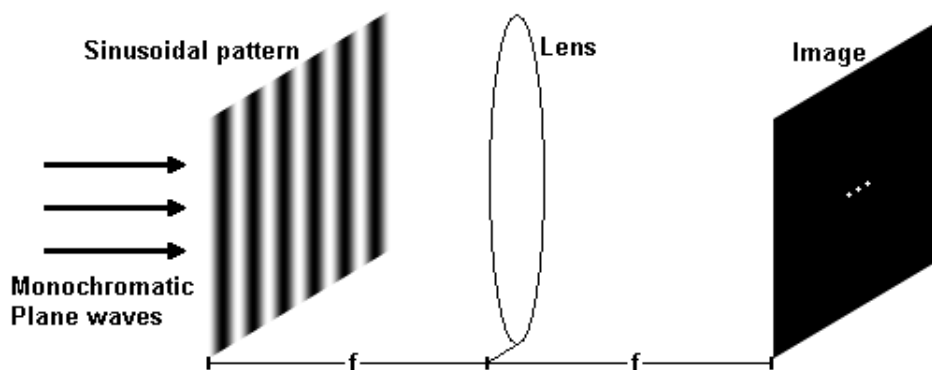


Figure 3.1: *Illustration of how a lens can be thought of as a Fourier transformer. The input pattern on the left applies a spatially varying sinusoidal amplitude modulation onto the incoming plane waves. The image produced at the other focus of the lens will be the Fourier transform of the input pattern. In this case the input image is a single frequency sinusoid therefore the Fourier transform will be a single Dirac delta along the frequency axis. However, the frequency of the sine function can also be negative, so there is a second ‘mirror’ Dirac delta corresponding to the negative frequency, and there is also a third Dirac delta in the middle representing a zero frequency DC term.*

focus of a lens and the corresponding image is shown.

The reason why this happens can be shown mathematically by applying the Huygens-Fresnel principle and calculating the resulting electric field at the image plane of the lens [139]. For the purpose of this thesis it is sufficient to say that the input pattern in Figure 3.1 is acting like a spatial light modulator and that if we were to replace it with a programmable LCD we would have control of the pattern formed at the image plane. Indeed if you think of the pattern in Figure 3.1 as a diffraction grating then you can see why the image pattern consists of a zero order and only a 1st and -1st order (because it is sinusoidal and not square).

What is not clear in Figure 3.1 is the division of intensity between the spots. In its current configuration, most of the light will end up in the zeroth order. Since one possible purpose for a SLM is as a beam steerer then having most of the power in the zeroth order would be wasted since this order cannot be moved from the

optical axis. This, incidentally, is also a hindrance when using diffraction gratings for spectroscopic applications since there is no wavelength spread in the zeroth order. To remedy this most modern diffraction gratings are now manufactured with a ‘blaze’ angle which has the effect of decreasing the intensity in the zeroth order and increasing the intensity in higher orders [139].

Some brief mathematics here are included here to complete the discussion and add justification.

Imagine a wave which is plane in x and y travelling along the z axis. Such a wave can be described by the following function

$$E_{in}(z) = A_o e^{iKz} \quad (3.1)$$

Where A_o is a constant representing the amplitude and K is the wavenumber.

The Fourier transform of this wave is the following

$$E(k_z) = \mathcal{F}\{E(x)\} = A_o \sqrt{2\pi} \delta(k_z + K) \quad (3.2)$$

Where δ is the Dirac delta function and k_z is the Fourier component of z . The solution is a single Dirac delta function. Therefore the electric field at the focal plane of lens due to this input beam will be a single point, i.e. this is exactly what a lens does to an incident plane wave, bringing it to a focus. However, if the incident plane wave is being acted by a diffractive optical element such as a diffraction grating or an aperture then the electric field at the input plane is described by

$$E_{in}(x, y, z) = t(x, y)A_0e^{iKz} \quad (3.3)$$

Where $t(x,y)$ is the spatially varying function describing the diffractive element. If this diffractive element has a sinusoidal function (like the grating in Figure 3.1) such as

$$t(x, y) = \cos(2\pi x/a) \quad (3.4)$$

Where a is the wavelength (or the spacing) of the grating. Then the resulting beam pattern at the focal plane can be calculated by

$$E_f(k_x, k_y, k_z) = \mathcal{F}\{E_{in}(x, y, z)\} = \mathcal{F}\{\cos(2\pi x/a)A_0e^{ikz}\} \quad (3.5)$$

$$\therefore E_f(k_x, k_y, k_z) = A_0\delta(k_z + K)[\delta(k_x \pm \frac{2\pi}{a})] \quad (3.6)$$

As can be seen we have two combinations Dirac delta function which correspond to the positive and negative values of the sinusoidal function. By changing the constant a , the period of the grating is changed and as a consequence so are the positions of the Dirac delta functions in the Fourier transform.

By placing a SLM in the Fourier plane and using it as a programmable diffraction grating and by altering the period and orientation of the grating hologram we can effectively control the position of the beam in the focal plane. The control can be expanded to multiple beams by simply summing the appropriate holograms for each

beam position together as was done in the original study by Reicherter et al [137]. So far this device allows control of multiple independent beams in the image plane, however the control can be extended further into the 3rd dimension. Rather than physically moving the SLM, an appropriate hologram can be used to act as a lens and thus allow for total control of beams in 3 dimensions as demonstrated by Curtis et al [138] and shown in Figures 3.2 and 3.3. Curtis also showed that these multiple independent beams can also be reconfigured at the refresh rate of the SLM (which at the time of writing this thesis is on par with PC display monitors at 60 Hz, though ferroelectric SLMs can operate in the kilohertz regime) i.e. they can be animated to produce dynamic optical patterns. With such practical versatility, it is easy to see why SLMs are attractive to use in optical tweezers setups.

3.2.3 Principle of operation

There are many different types of commercially available SLMs with each type having particular advantages and disadvantages. SLMs can be broadly divided into two groups depending on their principle method of addressing their pixels, namely: electrically addressed SLMs and optically addressed SLMs.

In an electrically addressed liquid crystal (LC) SLM the liquid crystal layer will be sandwiched between a silicon substrate and a transparent electrode just like a LCD as shown in Figure 3.4. Although this is only one possible design for a SLM the operating principles are similar across all designs.

In a nematic LC SLM, the liquid crystal molecules exist in a nematic phase

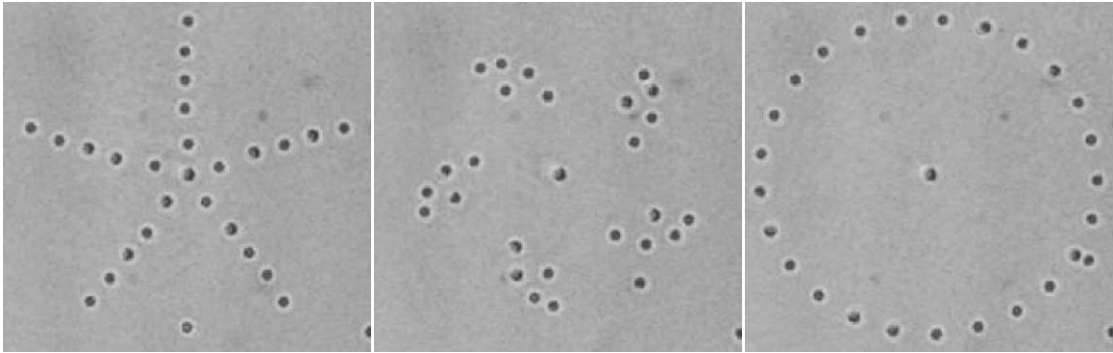


Figure 3.2: Patterns of movable $1\ \mu\text{m}$ silica spheres created by Curtis et al to demonstrate their dynamic HOT. Image reproduced from [138].

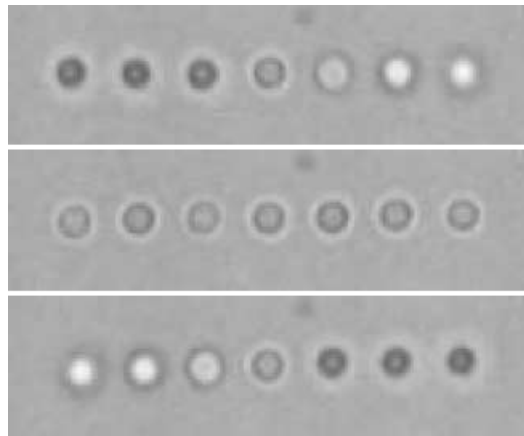


Figure 3.3: Demonstration of the 3D control. A series of silica spheres are held at different depths going from (left to right) $-5\ \mu\text{m}$ to $+5\ \mu\text{m}$ in the top frame, all at the same depth in the middle frame and $+5\ \mu\text{m}$ to $-5\ \mu\text{m}$ in the bottom frame. Image reproduced from [138].

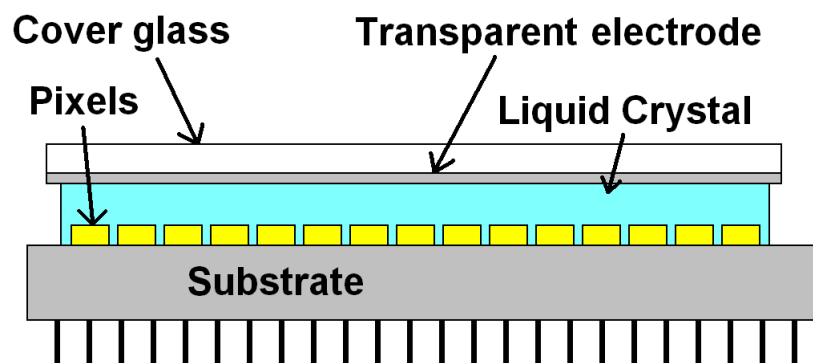


Figure 3.4: Diagram of an electrically addressed LC SLM

with their initial orientation determined by fine micro etching on the substrate during manufacture. When a potential difference is applied between a pixel and the transparent electrode an electric field is setup across the liquid crystal. Because they are polar, the molecules will try to break from their nematic phase alignment and rotate to align themselves with the electric field. The degree of rotation depends upon the strength of the electric field. The refractive index of the LC is affected by their orientation and so applied voltages result in changes in the refractive index. What this means is that light travelling through the LC will experience differing optical path lengths depending on the strength of the electric field across the LC. By controlling the pixels independently, different path lengths between pixels can be setup and this creates a phase difference between light rays incident on one pixel compared to another [140].

So by controlling the voltage to each pixel, it is possible to control the phase of a wavefront incident over the whole SLM. By using crossed polarisers and twisted nematic liquid crystals, it is possible to control the amplitude of the wavefront in exactly the same way a LCD works.

One immediately obvious limitation of this type of device is the pixel resolution. Ideally a SLM would be able to program for an infinite range of frequencies, however this would require an infinite spatial resolution. The pixelisation limits the range of possible frequency components which limits the efficiency of the Fourier transform. This is commonly known as ‘aliasing’ and can be a considerable problem in signal processing and related disciplines. This means that in reality SLMs have an upper

limit on the frequency components they can display which limits the range of usable holograms. For example, a grating hologram used to displace the beam along a single axis consists of a regular wave pattern (e.g. square, sinusoidal) i.e. a series of peaks and troughs. If the 'on' pixels represent peaks and 'off' pixels represent troughs, then the maximum frequency possible is achieved by setting alternating pixels on or off which gives a maximum frequency equal to half the number of pixels in that dimension. In Figure 3.4 the pixels from left to right would alternatively be on or off. Any higher frequencies would require additional pixels to be inserted between the existing ones (i.e. a higher resolution). It should also be noted that this maximum frequency is necessarily a square wave whereas lower frequencies can at least be approximated as sinusoidal to an extent again dependent on the frequency (sinusoids will begin to look square as the frequency is increased).

The other limitation this type of device has is its voltage resolution. The voltage at each pixel is determined by a (typically) 8-bit greyscale value. This means the voltage across the pixel can only have 1 of 256 possible values i.e. you can think of the pixel having a voltage resolution of 256. This means that the relative phase shifts between neighbouring pixels are discontinuous and that any sinusoidal wave represented on the SLM will be composed of a series of discrete digital steps rather than be continuously varying like an ideal sinusoid.

In practice these limitations mean that higher diffraction orders are ever present which reduces the power available to the more useful orders and puts a limit on the range of possible holograms. For example, using a defocus function would ideally

mean you could move a pattern through an infinite range of z , in practice, however, the beam quality will diminish with increasing z putting a limit on the ability of the beam to optically trap in three dimensions.

3.2.4 Beam aberration correction using SLMs

Unfortunately, another limitation of SLMs is that they are very difficult to manufacture with sufficient optical flatness for use in diffraction limited optics. The two types of SLM in common use are either electrically or optically addressed and both types can have severe wavefront distortions associated with them because of their poor optical flatness. These distortions inevitably lead to poor beam quality at focus and can disrupt an otherwise optimal setup. However, the ability of the SLM to modify the Fourier plane means that it should be possible to correct any distortion in the focal plane upon application of an appropriate hologram. In 2006 Wulff et al showed that this is indeed the case [141]. By adding low order Zernike polynomials to their hologram they were able to correct for focal and astigmatic aberrations in their system. They speculated that higher order polynomials would further increase the beam quality but they were unable to quantifiably confirm this.

Wavefront aberrations are most commonly described by a power series expansion where the aberration is expressed as a normalised sum of power terms that are functions of the optical system's coordinates (usually polar). Each term in the series corresponds to a specific aberration e.g. defocus, astigmatism and coma. The Zernike polynomials are this power series for circularly symmetric optical systems

and so are widely used in optics to correct aberrated wavefronts and improve image quality.

When solutions of this type are made into phase masks and added to the SLM, the SLM will essentially act as a lens to any incoming light. This makes it possible to defocus a beam through the z axis just by adding the appropriate phase mask.

Not only can the SLMs correct for their own optical shortcomings, but theoretically any optical aberration in the entire system can be corrected for (e.g. an out of focus lens) using the appropriate Zernike polynomials. An ideal optical system could use an iterative feedback program in conjunction with an SLM to automatically correct any beam aberrations.

3.2.5 Comparison to Acousto-Optic Deflectors

The main alternative of SLMs in the field of beam shaping is the Acousto-Optic Deflector (AOD). Both devices are used to manipulate beam patterns but each uses a different method. As I have explained above, SLMs work by rendering phase masks onto the Fourier plane of the beam and I will now briefly explain the operating principles behind AODs.

AODs make use the Acousto-Optic effect to diffract and change the frequency of incident light rays using sound waves. This is made possible by the photoelastic effect where mechanical stress can alter the permittivity ϵ (and thus, the refractive index) of the medium being stressed. In AODs, this mechanical stress is produced by sound waves in a transparent medium. By applying a periodic modulation of refractive

index then we have effectively created a diffraction grating which is capable of beam deflection. However, unlike SLMs, AODs are only capable of creating simple periodic functions (standing waves of sound) and not more general Fourier components. It can be argued that the operation of an AOD is a special case of the principle behind a SLM.

Where the AOD excels over the SLM however, is in its refresh rate. A typical SLM will refresh at about 60Hz (though ferroelectric SLMs have kilohertz refresh rates) whereas with an AOD, the response time is limited essentially by the speed of sound in the medium relative to the laser beam diameter. For a standard TeO₂ crystal AOD, this response time is on the order of 1.5 μ s/mm of beam diameter [22]. In practice these devices easily operate with refresh rates of several tens of kilohertz.

Because of their high refresh rate, these devices can construct beam shapes by quickly deflecting the beam back and forth in a scanning fashion to create the desired beam shape at focus. This is essentially time sharing the beam at a rate fast enough that we cannot perceive it (much like a CRT monitor scans an electron beam to construct an image) and in contrast to a SLM where the beam shape is physically altered.

Like SLMs, AODs can be used to create arrays of optical traps [142] but what they cannot do is sculpt complicated beam patterns that require a third dimension. This is because the AOD is only capable of deflecting the incoming beam along the x and y axes, it cannot defocus that beam through the z axis or apply any sort of phase mask to alter the beam's shape.

Each device has its merits and limitations and both have found widespread application in optical trapping and Biophotonics. I will focus on SLMs and discuss some of their uses in research from the literature, before proceeding with its application for my neuron growth experiments.

3.3 Spatial Light Modulators for neuron growth

My purpose for integrating a SLM into my optical setup was for two reasons: to beam steer automatically, and to beam sculpt. As previously mentioned, an AOD had already been used for these type of experiments but, due to the nature of the device, was only able to provide beam steering [135]. In this section I will provide details on the implementation of the SLM and of the software used to control it.

3.3.1 Optical train

Figure 2.2 in Chapter 2 shows the optical train used for the line profile experiments. The new setup was basically the same as this but with the cylindrical lens removed (since the SLM can now do all our beam shaping) and with the mirror conjugated to the objective replaced with the SLM. The 1064 nm Nd:YAG laser was also replaced with a 1070 nm Ytterbium fibre laser for these experiments. Figure 3.5 shows the new setup.

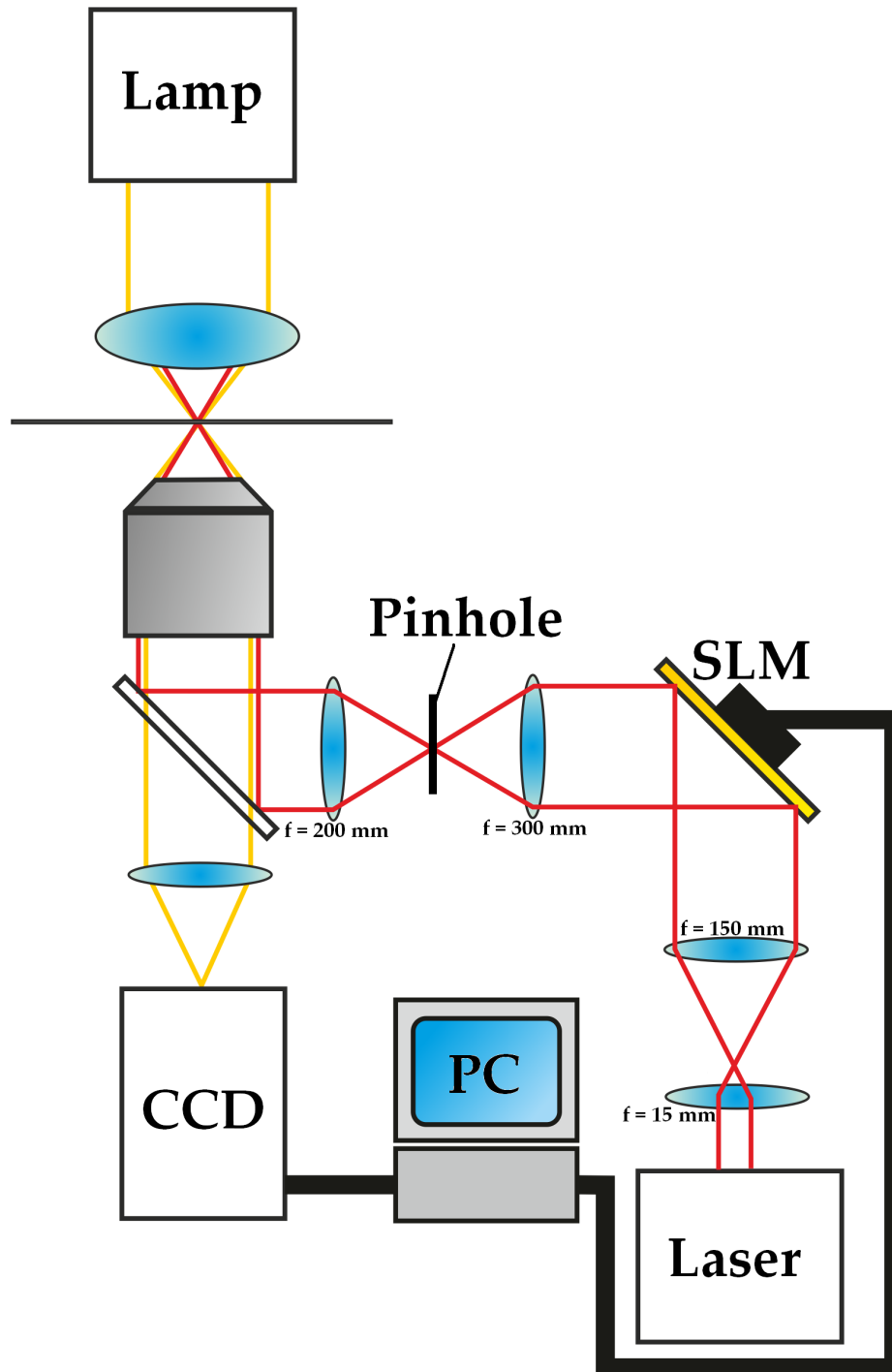


Figure 3.5: Diagram of the optical setup used for beam shaping experiments. This setup is similar to those shown before with the key change being the replacement of a mirror with the SLM. As shown this SLM is controlled by a PC to which the CCD is also connected. The laser is first expanded to 10 mm by the first telescope which is roughly the size of the rectangular SLM. The SLM is then imaged onto the back aperture by another telescope which also reduces the beam size to 6.6 mm which is about the size of the back aperture. The angle the SLM makes with the beam is exaggerated in this diagram, in reality the SLM is kept to as shallow an angle as possible. The pinhole at the focal plane of the SLM is used to filter off any unwanted higher orders resulting from the hologram.



Figure 3.6: Image of the Holoeye HEO 1080 P SLM used for these experiments. Image from the Holoeye website [143].

The SLM used for these experiments was a Holoeye HEO 1080 P phase modulator (Figure 3.6). This is a phase only SLM with a resolution of 1920 x 1080 and a pixel pitch of 8 μm . This model is optimised for the wavelength of the Ytterbium fibre laser (1070 nm) and is capable of providing a complete 2π phase shift.

As mentioned in the previous section, the first order of the SLM is the desired output to use because of the aberrations present in the zero order. Therefore the SLM will always have a default grating function applied that results in the first order being in the centre of the sample plane. All the other orders are removed by a pinhole present at the focus of the second telescope.

The SLM is controlled by a PC via a DVI cable. The PC is setup so that it treats the SLM as an additional display monitor. This essentially allows the operator to ‘drag and drop’ holograms onto this ‘monitor’ using the mouse. In practice, LabVIEW is setup to display the holograms at the appropriate coordinates for this ‘monitor’.

Before experiments can begin the optical distortion present in the SLM must

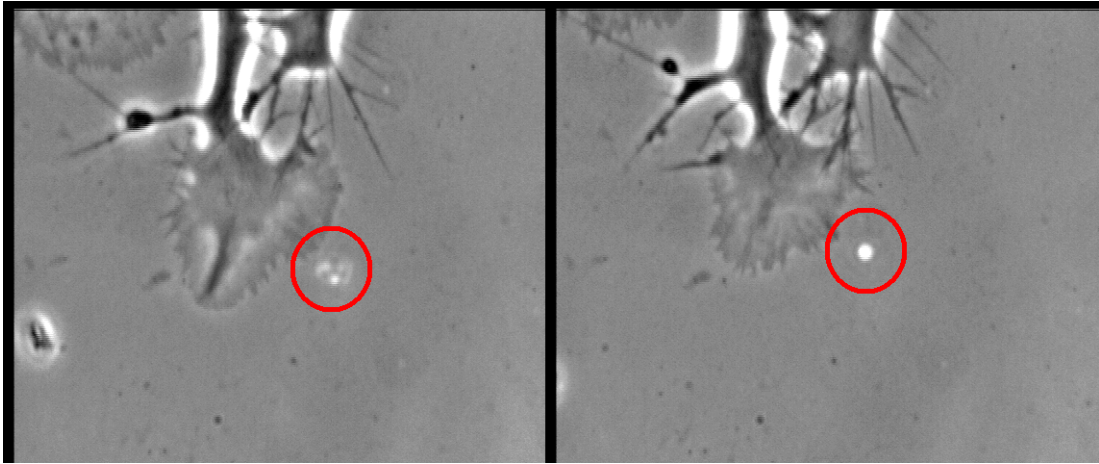


Figure 3.7: *Images of the beam from the SLM before (left) and after (right) the correction hologram was applied.*

be accounted for in order to get high quality beams at the sample. This was done using a Zernike polynomial generating LabVIEW program built by my colleague Dr Tomáš Čižmár. This program was designed to be used iteratively by the operator to produce the hologram necessary to correct for the aberration. By slowly adjusting the degree and orientation of each Zernike polynomial, a beam of sufficient quality for experimentation was produced as shown in Figure 3.7.

It is worth taking the time to explain more about LabVIEW since its use is essential to my experiments.

3.3.2 Introduction to LabVIEW

LabVIEW (short for Laboratory Virtual Instrumentation Engineering Workbench) is a graphical programming language produced and developed by National Instruments.

As a graphical language it differs to other programming languages in that the user physically draws how the data is to be managed and processed by using wires

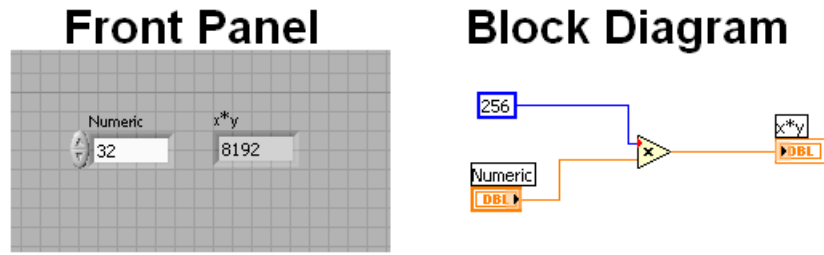


Figure 3.8: An example of an operation in LabVIEW. The Front Panel consists only of inputs and outputs and the Block Diagram shows the processes used to link between them. In this case a Numeric input (set to 32 in this case) is multiplied by a constant (256) and the output is displayed (8192). You can see how wires are used to represent data flow (which is generally left to right) and icons are used to represent processes.

and nodes. The LabVIEW interface is divided into two windows: the front panel and block diagram. The front panel is designed to resemble what you would see on the front panel of a real device, such as controls, inputs and outputs. The block diagram represents the internal circuitry of the virtual instrument and is represented by wires carrying data and icons processing that data. An example of a simple multiplication operation is shown in Figure 3.8. LabVIEW 8.2 was used to build all of the software for my experiments.

3.3.3 Shape detection using LabVIEW

To steer the beam using a SLM, all that is needed is to program LabVIEW to generate a hologram and then display that hologram on the SLM using the fact that MS Windows treats the SLM as an additional monitor. For a simple diffraction grating in the x and y axis this is a simple process.

However, in order to automatically steer the beam, a feedback process is required. This involved taking images from the CCD in the setup (Figure 3.5) using LabVIEW, extracting the necessary information from these images and the render-

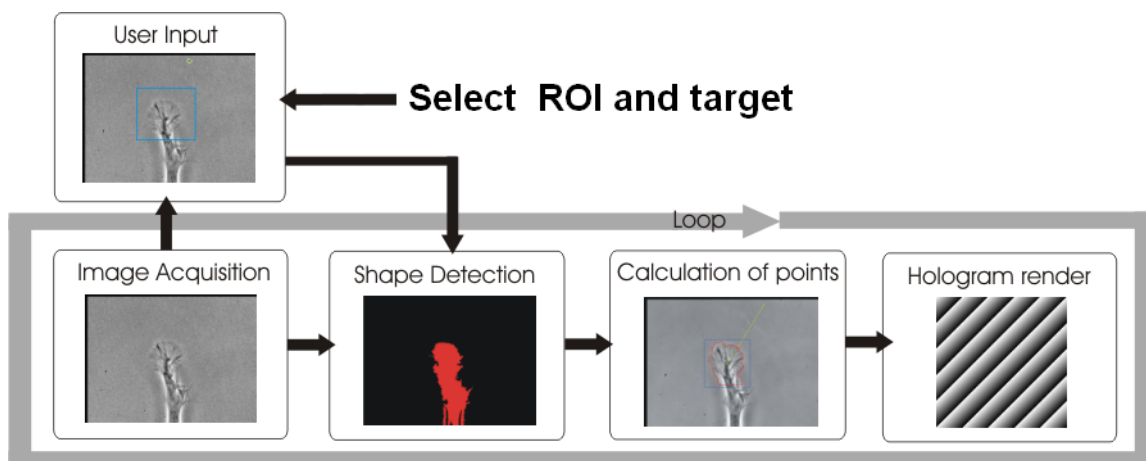


Figure 3.9: Diagram showing the basic process of the LabVIEW program. The first step is to acquire an image from the CCD. The user must then tell the program where the growth cone is (there may be several on the screen at one time and it is important to tell the program which one is to be experimented upon) by defining a region of interest (ROI) and must also select a target point to where the user wants the growth cone to grow towards. From this information, LabVIEW can detect the shape of the growth (and thus the edge) and the “centre of mass” (COM) of the growth cone (which is determined by a simple pixel weighted average). A trajectory is plotted between the COM and the target point (TP), the point where this line crosses the edge is where LabVIEW will direct the laser beam which it does by rendering the appropriate grating hologram. This process is looped so that the hologram is constantly updated (with a rate of about 30Hz on our PC)

ing the appropriate hologram. The goal is to automatically track the advancing growth cone of a neuron and ensure that the beam is constantly on the edge of this growth. The beam cannot just be anywhere along the edge, it must be such that the growth cone will grow in the desired direction I want it to. To this end a user inputted target point is required and the line between this point and what is defined as the “centre of mass” of the whole growth cone, is plotted. Where this line crosses the edge of the growth is where the laser should ideally be. Figure 3.9 shows a graphical representation of this process.

The shape detection algorithm is the most complex part of this program and needs to be described in detail. The algorithm works by taking an image which has come from the CCD, removing all but the user selected ROI and then applying a

series of morphological filters to extract the necessary information. Since Stuhrmann et al [135] had built their AOD program on LabVIEW I began by taking apart their code to design the shape detection part of my program. The operating principles are basically the same since we both use LabVIEW's inbuilt image analysis sub-VI's. Figure 3.10 shows a graphical step by step process of the shape detection process.

All of the morphological filters use an imaging process known as convolution, which is basically the multiplication of two arrays of numbers (one array being the image and the other being what is known as the kernel). The output array of this multiplication is the processed image. An example of this process upon a simple image is shown in Figure 3.11 and an example of a Gaussian filter applied to a real image is shown in Figure 3.12. A Gaussian filter is used in Figure 3.10.1 to remove noise. The Gaussian kernel used in my program is as follows:

| | | |
|---|---|---|
| 1 | 2 | 1 |
| 2 | 4 | 2 |
| 1 | 2 | 1 |

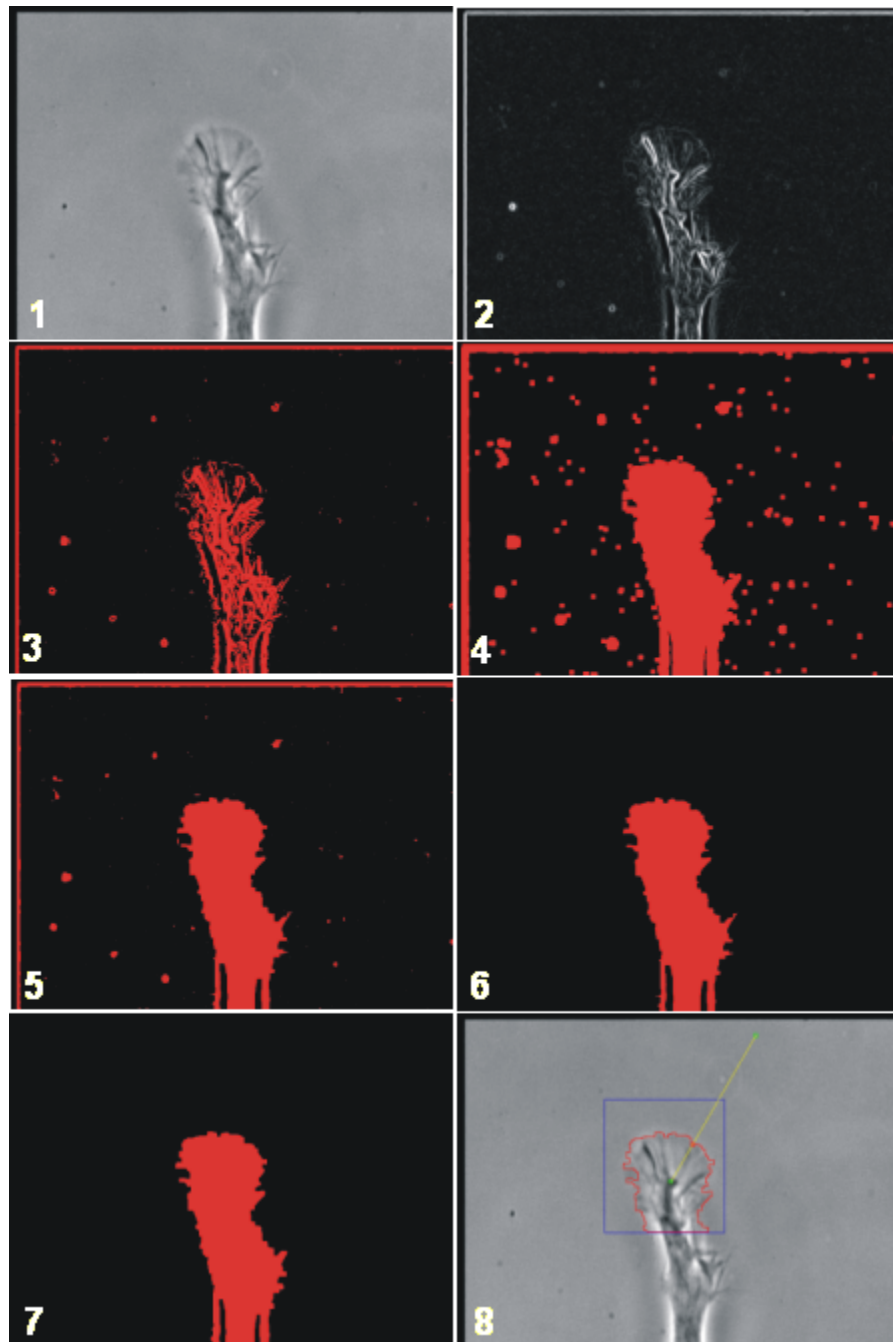


Figure 3.10: Step by step diagram of the shape detection process. For this diagram the whole image rather than an ROI was subject to the shape detection process with the exception of frame 8. 1. Raw image from CCD with Gaussian filter applied. 2. Prewitt filter applied. 3. Image made binary. 4. Dilation and fill operation. 5. Erosion. 6. Particle filter. 7. Smoothing. 8. Shape information overlaid on to original image, this includes the centre of mass, a user inputted target point, the trajectory between the two and the point where this line intersects the edge.

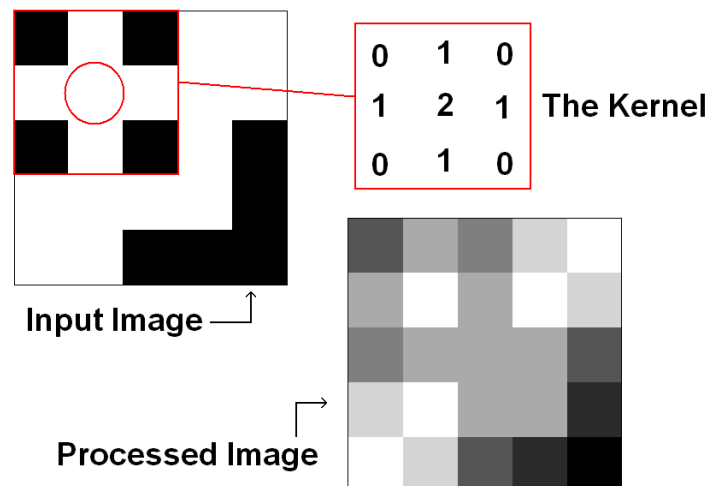


Figure 3.11: Shown here is a simple 5×5 pixel image being operated on by a simple 3×3 kernel. Each pixel in the input image is operated on one at a time by the kernel. For this example, the red circle represents the current pixel being operated on and the red square represents the kernel around this pixel. In the case of a 256 greyscale image a black pixel represents a zero, a white pixel represents 255 and grey pixels are numbers in between. To compute the output from the red circle pixel, the elements from the kernel are first multiplied by the pixels they land on so in this simple case we would have the four black corners being multiplied each by zero, the four white middle pixels being multiplied by one and the centre white being multiplied by two. Summing these answers together yields 1275. 1275 is the value to which the red circle pixel becomes but 1275 is of course greater than the maximum possible value of 255, but the greyscale values loop around so that 256 would actually equal 0 and $260 = 4$ and so on. 1275 will be equal to 255 and so the processed pixel in this case is white. The kernel is then moved onto the next pixel and the process is repeated until all pixels have been operated on and the result is the processed image shown. This particular kernel is an example of a Gaussian kernel (if you imagine the kernel being plotted in 3D then its Gaussian nature becomes obvious) and Gaussian convolutions soften edges as well as reduce noise.

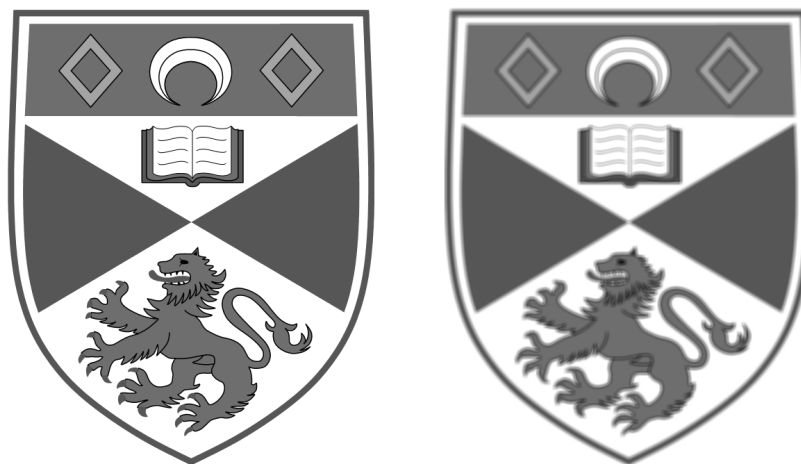


Figure 3.12: Example of Gaussian convolution done on a real image. On the left is the original and on the right is the processed image. As can be seen the image appears blurred.

The next part of the process is to find the edges of the growth cone structure and this is done using a Prewitt filter [144]. A Prewitt filter calculates the response from the image to a series of convolution kernels to find areas of high contrast, such as those that occur at the membranous edge. The Prewitt filter used in this program uses 8 kernels and its application is shown in image 2 of Figure 3.10. The 8 kernels used for the Prewitt convolution are as follows:

| | | | | | | | | | | | |
|----|---|----|----|----|----|----|----|----|----|----|----|
| -1 | 0 | 1 | -1 | -1 | 0 | -1 | -1 | -1 | 0 | -1 | -1 |
| -1 | 0 | 1 | -1 | 0 | 1 | 0 | 0 | 0 | 1 | 0 | -1 |
| -1 | 0 | 1 | 0 | 1 | 1 | 1 | 1 | 1 | 1 | 1 | 0 |
| 1 | 0 | -1 | 1 | 1 | 0 | 1 | 1 | 1 | 0 | 1 | 1 |
| 1 | 0 | -1 | 1 | 0 | -1 | 0 | 0 | 0 | -1 | 0 | 1 |
| 1 | 0 | -1 | 0 | -1 | -1 | -1 | -1 | -1 | -1 | -1 | 0 |

After the Prewitt filter is applied we are left with a ghostly looking image where edges (areas of high contrast) are whitened and everything else is blackened. To extract the structure of the growth cone we need to ‘fill in’ the shape in the middle, but the edges are not perfect and are broken and so any filling operation will fail at this point. In order to complete the edges a few more operations are needed.

This first additional part of this process involves making the image binary. A binary image has pixels of value either 1 or 0, but our greyscale image has values 0 to 255, so in order to make the image binary we need to set a threshold value. Any pixel above this threshold becomes a 1 and any pixel below this value becomes a 0. This threshold value is left as a control for the user to adjust as necessary in order to extract the shape. This is because a set value of threshold may give a nice

shape one day but could fail to detect a shape the next day. This is due to several factors including the background light level in the room, the transparency of the glass and the thickness of the growth cone. Rather than attempt to standardise all these possibilities, it is easier to leave the threshold value as an adjustable control that only needs to be calibrated at the beginning of the experiment. The result of the binary process is shown in image 3 of Figure 3.10.

After thresholding, a binary morphological process known as dilation is applied. This is done using a prebuilt LabVIEW sub-VI which basically inflates the size of any pixels in the binary image. This is enough to close the borders around the shape of the growth cone and then a filling operation can be done as shown in image 4 of Figure 3.10.

The dilation operation will have changed the shape of the growth cone slightly and so to compensate for this the opposite of a dilation operation (known as erosion) is applied. This serves to help return the shape to its previous state before the dilation and also removes some particle noise as seen in image 5 of Figure 3.10.

We now have the complete filled shape of the growth cone and the image in next processed to remove any remaining artifacts. This involves applying a particle filtering operation which removes any object that does not survive 8 successive erosion operations (image 6 of Figure 3.10) and then a dilation operation followed by an erosion operation is applied in order to remove excessively jagged edges for the shape. The result of these operations are shown in image 7 of Figure 3.10.

All dilation and erosion operations use LabVIEW's inbuilt morphology VI's and

use the following 3 x 3 structuring element:

| | | |
|---|---|---|
| 1 | 1 | 1 |
| 1 | 1 | 1 |
| 1 | 1 | 1 |

The shape shown in image 7 of 3.10 is suitable to extract the required information necessary for the automation process. The ‘centre of mass’ of the detected shape is extracted as a coordinate by LabVIEW by means of a pixel weighting average. A straight line between the centre of mass and the user inputted target point is then plotted and the point where this line intersects the edge of the shape is extracted. It is at this point where the laser radiation is to be directed and so a hologram of a grating that will move the laser on to this point is generated into a greyscale numerical array which is then displayed on the SLM by LabVIEW. Previously, a calibration will have been run to allow LabVIEW to identify what period and orientation of grating is needed to move the laser spot to coordinates x and y. This process is then repeated several times a second so that LabVIEW can adjust the beam position as the edge of the growth cone advances.

3.3.4 Application of program

Shown in Figure 3.13 is an image sequence of this program successfully executing automatic optically guided neuronal growth using a Gaussian laser beam.

Since the laser naturally emits a standard Gaussian distribution profile, the SLM is not required to shape the beam in this case but only for steering via the appropriate diffraction grating holograms. However, another beam shape that has

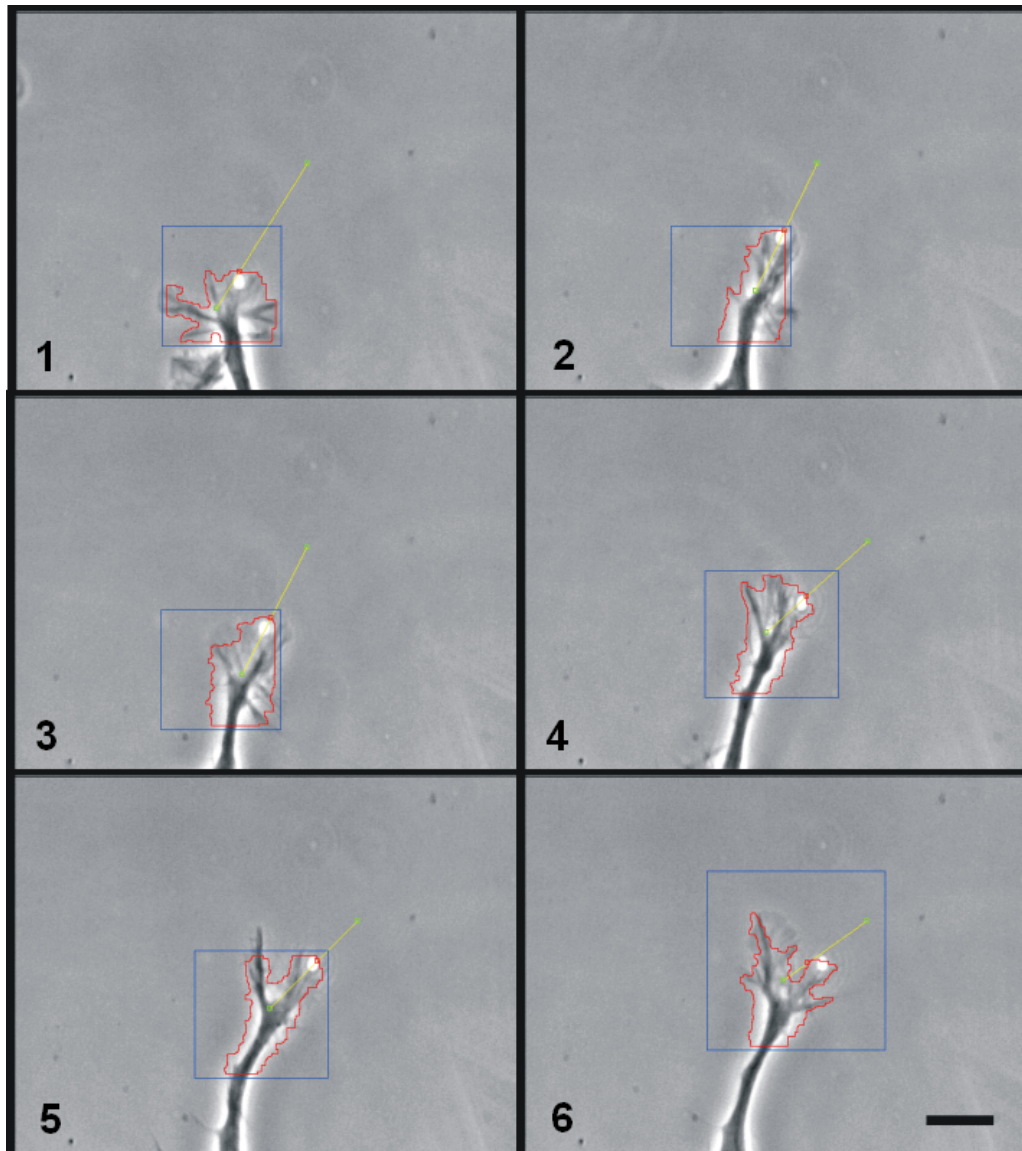


Figure 3.13: Image sequence of automatic neuronal guidance using a Gaussian laser beam (approximately 40 mW). Images are chronologically presented from 1–6 and frames are approximately 2 minutes apart. The growth cone is initially growing in an upper left direction but a clear change of direction is evident as the sequence progresses. Scale bar is 10 μm . A video of this experiment is included in the CD that accompanies this thesis

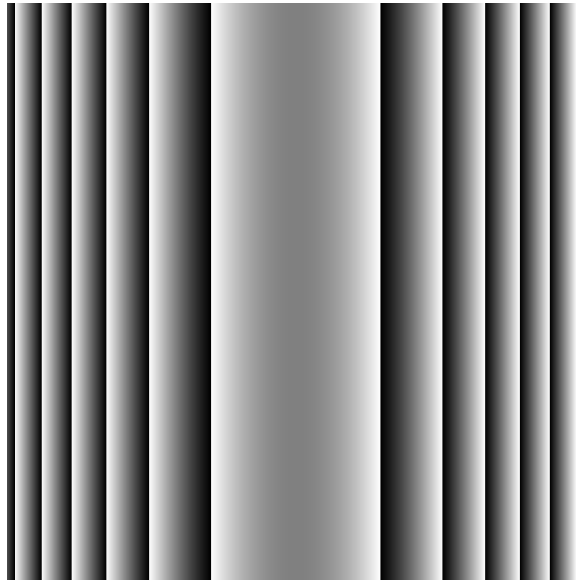


Figure 3.14: *Hologram to generate a line profile. It can be thought of as a one dimensional lens so that the beam is only focused in one dimension to produce a line which is the exact same way a cylindrical lens creates a line profile. The length of the line profile can be altered by adding in focusing in the other dimension (not shown here) and the beam can be rotated simply by rotating the hologram. In order to move this beam in x and y it must be added numerically to the appropriate grating hologram. It is also possible to add asymmetry to this line but it is slightly more complicated and involves numerically adding the holograms of shorter and shorter lines at slightly different spatial positions to each other.*

been reported to successfully guide neuronal growth cones is a line profile [115,116].

Previously, this beam has been generated statically using cylindrical lenses but this beam can also be created using the SLM. The added advantage of the SLM is that the beam can be changed at any moment without having to go through the tedious process of changing the optics. Since a line profile can be thought of as a Gaussian profile that has been elongated in a single dimension, the hologram to generate such a beam is simply a one dimensional lens as shown in Figure 3.14. Using the SLM to generate a line trap suitable for guiding neurons was successful and an example of this is shown in Figure 3.15.

Another type of beam I investigated for neuron growth was a Bessel beam. As previously mentioned, Bessel beams are finding unique roles in the field of biopho-

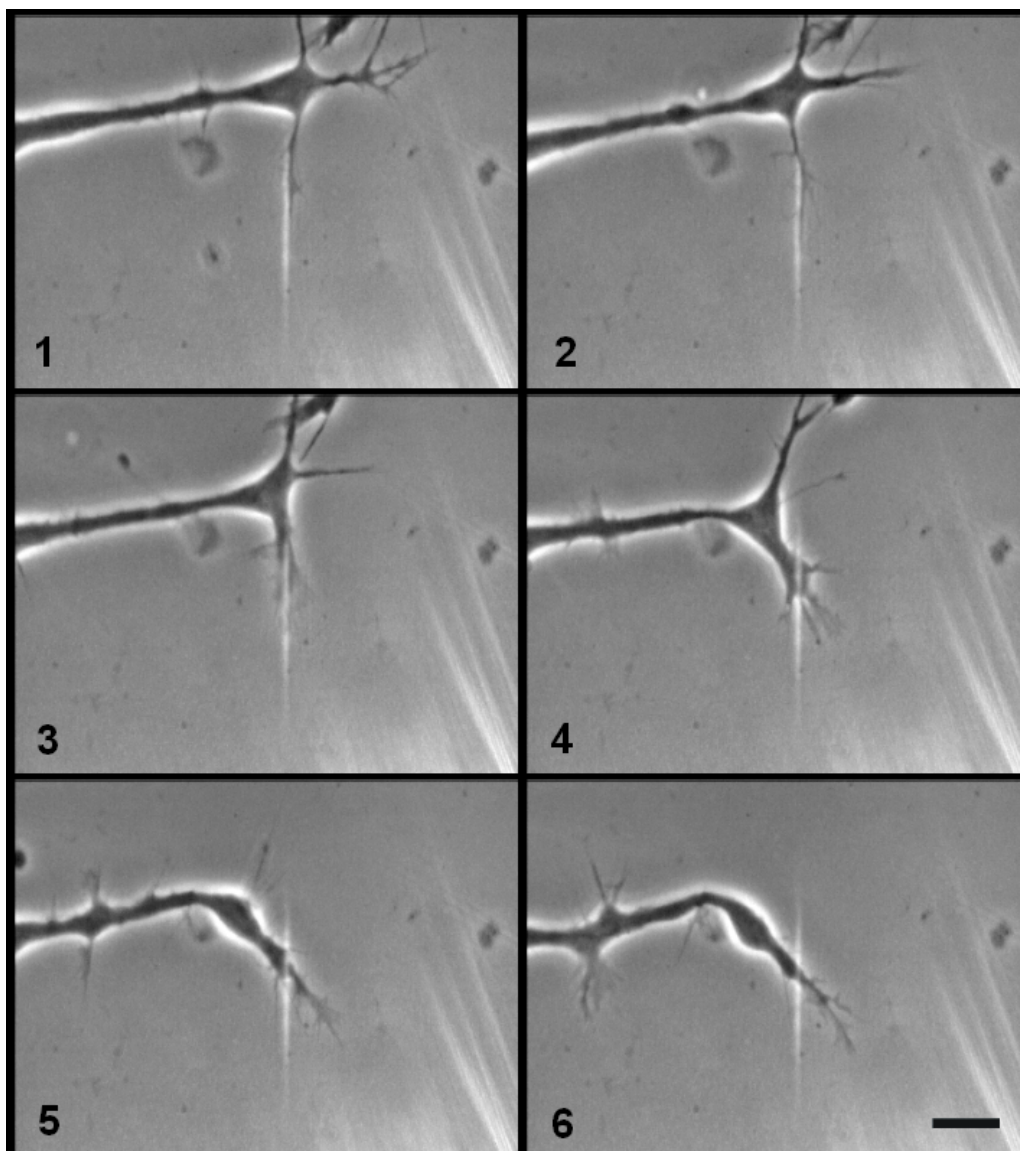


Figure 3.15: *Image sequence of a line profile laser beam guiding a growth cone. Frames are two minutes apart and proceed from 1 to 6. Scale bar is 10 μm . A video of this experiment is included in the CD that accompanies this thesis.*

tonics with specific examples being photoporation [145] and optical cell sorting [27]. The defining characteristic of a Bessel beam is its ability to propagate without diffracting over a longer working distance than a Gaussian beam. As shown in [145] this means a longer effective working distance for the beam in the z axis is possible. Such a thing may be of no apparent benefit to a well aligned and bolted down optical setup, but if one were motivated to move this technology into a clinical environment where bulky optics may not be accommodated and/or *in vivo* procedures were being carried out, then a longer working distance would be of great advantage.

To generate a Bessel beam using a SLM is fairly simple. In traditional optics, a Bessel beam can be created using by illuminating a thin annular ring at the focal plane of a lens or by using an optical component known as an axicon, which is essentially just a cone shaped lens. Where a normal spherical lens will bring incoming plane light to a point of focus on the z -axis, an axicon will bring the incoming light to a line of focus along the z -axis. An ideal Bessel beam would never diffract and is impossible to create because it would require an infinite number of rings (and thus an infinite power) and it would be more appropriate to refer to the Bessel beams generated in laser physics as “Bessel-like” beams. An illustration of this is shown in Figure 3.16.

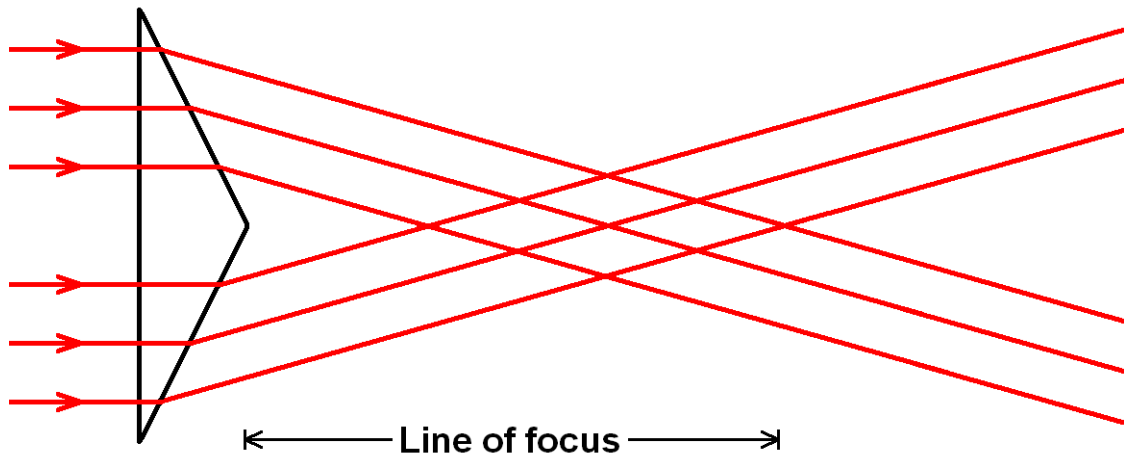


Figure 3.16: *Illustration of incoming light being focused through an axicon. Each ray of light is deflected by exactly the same angle leading a continuous series of focal points i.e. a line of focus. The line is not infinite and is limited by the width and opening angle of the axicon.*

When a Gaussian beam is incident on an axicon, the output interference pattern is described by the zeroth order Bessel function $J_0(x)$ [146]. This beam pattern consists of a central core which does not diffract appreciably as it propagates surrounded by a number of rings of equal power. The distance this beam can propagate without appreciable diffraction is proportional to the beam width of the incident Gaussian and inversely proportional to the opening angle of the axicon.

To create a Bessel beam using a SLM one only needs to add the appropriate phase mask. For a spherical lens we saw that this phase mask is simply a Fresnel lens pattern but for the case of an axicon the hologram resembles a solid ring, the diameter and thickness of which determine the properties of the produced Bessel beam. A diagram of this is shown in Figure 3.17.

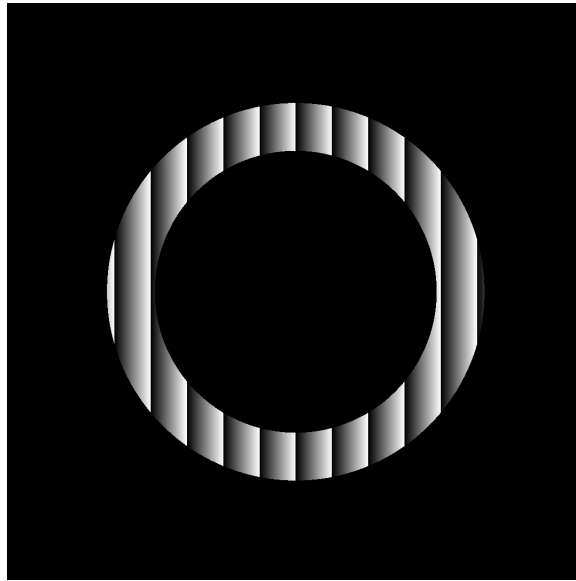


Figure 3.17: *Hologram phase mask for a Bessel beam. In order to isolate the ring from the rest of the beam a diffraction pattern has been added to the ring area. This serves to deflect the ring region away from the bulk of the beam so that the ring can produce the Bessel pattern in the Fourier plane without interference. It would also be possible to reverse the situation and apply the diffraction pattern to the whole SLM excepting the ring, but this would leave us unable to steer the beam. This particular phase mask serves only to illustrate the concept and was not used in any experimental situation.*

Since the SLM operates in the Fourier plane it is the Fourier Transform (FT) of the phase mask that will determine the beam pattern in the image plane. In a two dimensional plane of coordinates x and y the FT of a Delta function will be a Sine function [147]. However, in polar coordinates r and ϑ the FT of a Delta function will be a Bessel function of the zeroth order [148], this form of FT is known as the Hankel transform. Of course, since a Delta function is impractical (no power would get through) then we must use an approximation and so a Rectangular (or “top hat”) function is used instead. In cartesian, the FT of a Rectangular function is a Sinc function [149] but in polar coordinates the FT becomes a series of Bessel functions [150] which will allow limited diffraction (as opposed to no diffraction for the ideal case) over a range of z much larger than that for a Gaussian beam. So a

ring of finite thickness is used as an approximation to the ideal Bessel function with the trade off being the thinner the ring (which will give you a better Bessel beam) the less power that is transmitted.

For my experiments a Bessel beam with a central maximum diameter of $1\ \mu\text{m}$ and a measured propagation length of $15\ \mu\text{m}$ (the depth of focus for a comparable Gaussian beam was just $3\ \mu\text{m}$) was created using the SLM. The phase mask and resulting beam pattern at focus is shown in Figure 3.18.

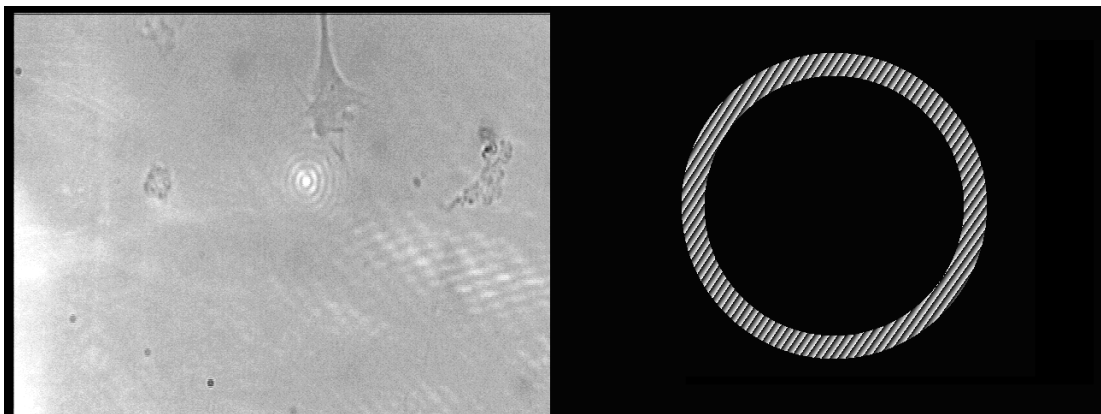


Figure 3.18: *Raw image of the SLM created Bessel beam at focus in a sample chamber (left) and the hologram used to create this beam (right).*

In my 2009 publication I reported for the first time the use of a Bessel beam to artificially guide the developing axon of a neuron [136]. Like all previous experiments, this was done by keeping the beam (in this case the central core) aimed along the leading edge of the neuronal growth cone. Shown in Figure 3.19 is an image sequence demonstrating the ability of the Bessel beam to guide a neuronal growth cone.

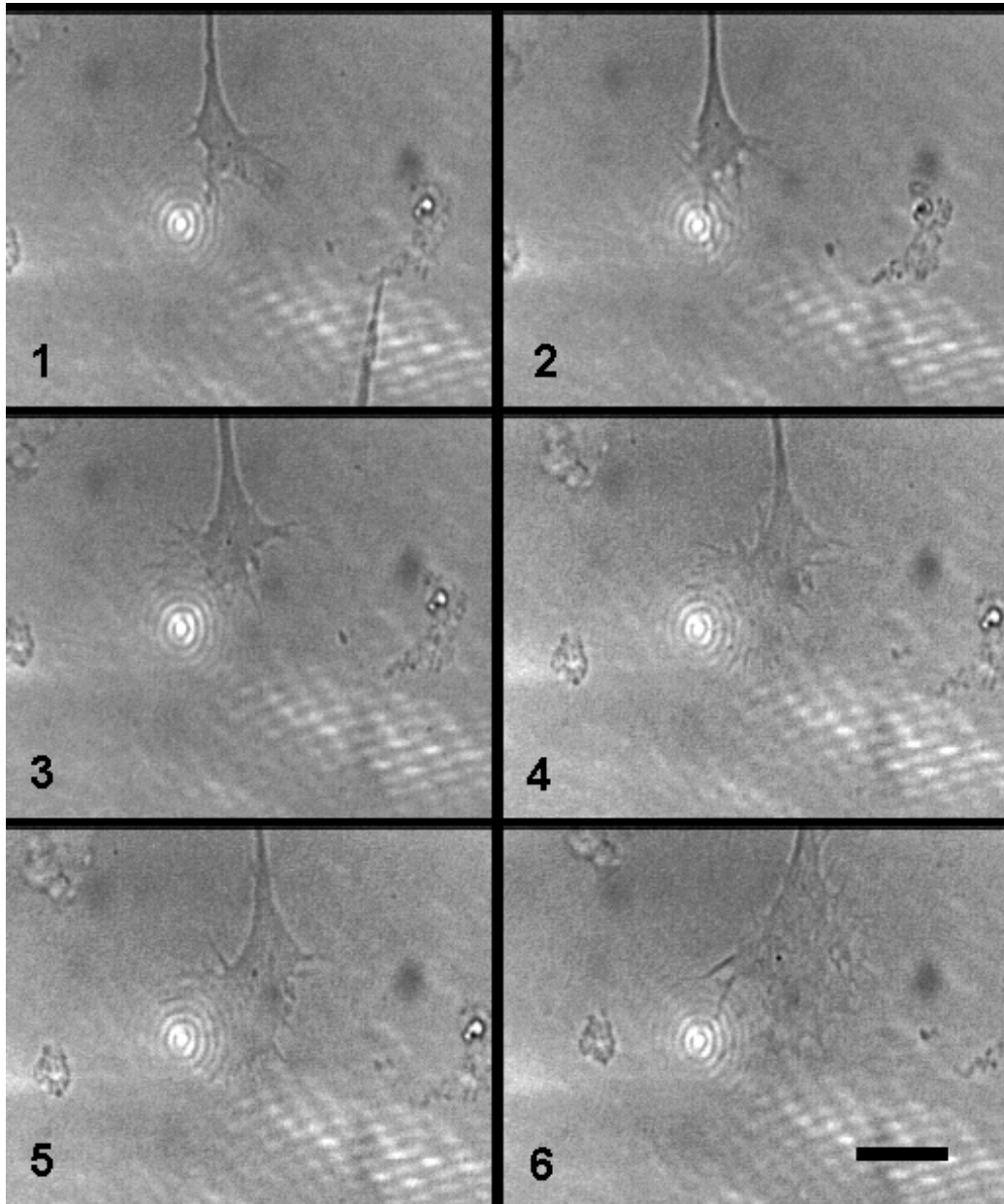


Figure 3.19: *Image sequence of Bessel beam (total power 60 mW) guiding a neuronal growth cone. Frames are two minutes apart and proceed from 1 to 6. Scale bar is 10 μm . In this experiment a standard brightfield objective was used (Nikon 60 1.4NA) since using a phase contrast objective would reduce a selection of accessible sizes of the Bessel beam central core due the presence of the phase ring. Therefore the images in this figure have had their contrast digitally increased slightly to boost the detail and again clear guidance may be observed. A video of this experiment is included in the CD that accompanies this thesis*

3.4 Conclusion

In this chapter I have demonstrated the successful use of spatial light modulators to manipulate laser beams for use in optically guided neuronal growth. I have also shown how this technology may be coupled with reasonably simple software to automatically track developing growth cones. The development of such technology will be invaluable for the expansion of applications that will require a high degree of control over the dynamics of neuronal growth cones such as the production of artificial neural networks or possibly even *in vivo* nerve regeneration.

The software developed for these experiments can also be utilised for other biophotonics applications that require cell tracking. One possible use could be for automating photoporation experiments where this has required a laser to be aimed precisely on individual cells (in some cases distinguishing between the nucleus and the cytoplasm) and is usually done several hundred times for statistical purposes [151]. So far, all these experiments have been performed manually, moving the stage or beam in much the same manner that the original neuronal growth experiments were performed. The software described here could be used to determine the shapes of whole cells instead of just growth cones and could then determine their centre of mass and convert this coordinate into a hologram for a SLM.

Additionally, I have also demonstrated that a SLM can produce novel beam shapes appropriate for neuron growth experiments including line profiles and Bessel beams. The creation and use of a Bessel beam is of particular note because previous experimental setups using AODs are incapable of creating such a beam

[135]. The demonstration of a Bessel beam to guide neuronal growth cones is also an advance in this field towards *in vivo* experiments where any small scale axial motion could now be compensated for due to the elongated nature of the light field.

One of the great difficulties in investigating optically guided neuronal growth is the immense time and precision it can take to achieve successful guidance which as a consequence makes it very difficult to gather statistics. In the field there is a colloquial term “the human factor” which is used to describe how some operators just cannot seem to get successful guidance despite months of careful trying. But, the experimental setup described in this chapter paves the way for a detailed, systematic and unbiased analysis of this phenomenon which would hopefully be free of any human factor due to the increased level of automation.

With some more improvements the functionality of the software could be increased to perform more advanced operations. This could include multiple beam tracking and guiding, perhaps guiding several axons at once on a wide field of view. It may be possible to form synapses using one beam to guide an axon and another to pin or slightly pull a dendrite from the target cell. Multiplexing the beam is a very simple matter for a SLM and the only limiting factor would possibly be the CPU speed of PC. Since CCDs in microscopes for imaging are quite widespread and since also that SLMs are finding increased integration into optical setups, the implementation of this software onto any professional setup is made simple. Because of this ease of integration and its possible utility, software such as the sort developed in this chapter may find increasing roles in biophotonic setups.

Chapter 4

Investigations into the biochemistry of optically guided neuronal growth

4.1 Introduction

In this chapter I will describe a series of experiments to help determine if the laser irradiation in my previous experiments could be inducing cellular stress in the NG-108 cell line or if the neurite can still be guided by the laser in the presence of certain enzyme inhibitors. These experiments will test whether specific signalling pathways are activated in the NG-108 cell line such as the heat shock stress pathway and the mitogen-activated protein (MAP) kinase pathway.

Ehrlicher et al noted that the heating effect due to the laser could influence the chemistry of the cell in this way, but also claimed that the effect was not sufficient enough to explain their observations [114]. It's plausible that disruption to cytosolic proteins is being caused by application of a IR laser beam used in neuron growth

experiments and this may explain why growth cones seem to grow towards a focused laser spot. Stress in cells is responsible for a cascade of chemicals and growth factors being both upregulated or down regulated which can adversely affect the morphology and growth of the cell [152, 153].

The purpose of inhibiting certain proteins in the MAP kinase family will allow me to investigate whether these pathways are necessary for laser guided growth or if the laser can still guide growth cones when these pathways are blocked. These pathways have been chosen because of their effect on the growth and development of the cytoskeleton [154–156]. If these pathways are inhibited and the growth cone still grows towards the laser, then it can be concluded that the laser is not triggering these pathways and mechanism is something else. On the other hand if inhibition of these pathways prevents the growth cone from being guided then it may be that the cell needs the function of these protein pathways in order to be guided or that the laser may be acting as a guidance cue by triggering these pathways.

This chapter will be divided into two sections, the first detailing my investigation into the heat shock response and the second will be about the protein inhibition experiments.

4.2 HSP-70 as an indicator for laser induced cell stress

4.2.1 Introduction

To do the heat shock experiments, I successfully transfected NG-108 cells and CHO-K1 cells with a plasmid containing the mouse promoter of heat shock protein 70 (HSP70) tagged with green fluorescent protein (GFP). When these cells are thermally stressed by heat they upregulate the HSP70 molecule [157] and thus also GFP which will be visible because the cells will fluoresce green under UV light [158]. If these same cells were also to fluoresce after laser irradiation then we can conclude that the laser causing the upregulation of HSP70 promoter which implies that the cell is eliciting a heat shock response. If these cells do not glow after laser irradiation then we can conclude that the HSP70 promoter is not being transcribed which strongly suggests that the stress suffered by the cell (if any) due to the laser is not enough to trigger this particular stress pathway. Activation of cell stress may also explain why growth cones under laser guidance seem to stall after about 30-40 minutes of irradiation as reported in previous studies [114, 115, 117, 159]. Included in this section will be a discussion of transfection, a description of HSP70 and why it was used as well as a discussion of the results from the experiments.

Transfection involves inserting otherwise foreign DNA into an organism so that the organism will read this new code and transcribe as if it were its own. Transfectants can be either transient or stable depending on whether the DNA becomes

integrated into the genome. Transient transfectants do not integrate the DNA into the genome and it is subsequently diluted and lost after a few cell divisions. However if the foreign DNA contains a marker gene, such as a particular antibiotic resistance, then by exposing post transfected cells to this antibiotic, the transient cells will die after a few divisions leaving only those cells which completely integrated the foreign DNA into their genome creating a stable cell line.

4.2.2 Plasmid construction

The aim of this experiment was to determine whether or not cells were being stressed by laser irradiation. Therefore one way to establish this is to analyse the expression of proteins that are activated by stress.

4.2.2.1 Heat Shock Protein

Heat shock proteins (HSPs) are a branch of functionally related proteins in cells which are expressed when the host cell is exposed to thermal or other stress. These proteins are one of the most primitive mechanisms for cellular protection and are found in all forms of life including the simplest bacteria. These proteins can also exist in cells that haven't produced a stress response where they act as translocators and folders of other polypeptides and as such are referred to as molecular "chaperones" [157].

There are several proteins that can be considered as heat shock proteins and Table 4.1 contains details on the most common ones. The protein of interest in this work is HSP70 because, unlike some of the other HSPs, it is transcribed only

| Family | Name | Location | Expression | Level |
|-----------|-----------|-----------------|------------|----------|
| | | | Normal | Stressed |
| HSP100 | HSP110 | Nucleus | + | ++ |
| | HSP104 | Cytosol | + | +++ |
| | GRP100 | ER/Golgi | + | +++* |
| HSP90 | HSP90 | Cytosol/Nucleus | ++ | +++ |
| | GRP94 | ER | + | +++* |
| HSP70 | HSP70 | Cytosol/Nucleus | - | +++ |
| | HSC70 | Cytosol/Nucleus | ++ | ? |
| | GRP78 | ER | ++ | +++* |
| | MTP70 | Mitochondria | + | ++ |
| HSP60 | HSP60 | Cytosol | + | + |
| | HSP58 | Mitochondria | + | + |
| HSP40 | HSP40 | Cytosol/Nucleus | + | ++ |
| HSP30 | HSP32 | Cytosol | + | ++ |
| | HSP35 | Cytosol | + | ++ |
| small HSP | HSP27 | Cytosol/Nucleus | + | ++ |
| | HSP10 | Mitochondria | + | ? |
| Ubiquitin | Ubiquitin | Cytosol | + | ++ |

Table 4.1: Classification of heat shock or stress proteins showing where they are expressed and how their expression changes under stress. Plus signs are used as an arbitrary measure of the level of expression. A minus sign means no expression and a question mark means the level of expression is unknown. The asterisk denotes that the stress is not induced by heating. Data in table from [157].

when the cell elicits a stress response (as shown in Table 4.1). So during a heat shock event, several HSPs will be upregulated, but only HSP70 does not exist in the cytosol before the heat shock event whereas the other HSP's will already be present. Therefore, only HSP70 expression provides an “on/off” signal for thermal stress.

The heat shock proteins are named by their size and so HSP70 has a size of 70 kilodaltons (kDa). When expressed, this protein acts as a repair system to the cell by ensuring that other cytosolic proteins do not denature due to the stress event. This has been observed in the bacteria *Escherichia coli* [160] [161] as well as in mammalian cells [162].

The temperature at which these proteins are induced depends on the organism

but it usually occurs about 5-10 °C above the normal temperature for the organism. For example, expression occurs at approximately 42 °C for mammals (in humans, HSPs are expressed during pyrexia), 37 °C for *Drosophila melanogaster* (normal temperature 25 °C) and arctic fish express them at approximately 10 °C [163]

Perhaps a testament to how important this protein is for cell survival is the fact that the gene for HSP70 is found, not once, but eight times in the human genome [164].

The production of HSP70 is regulated by a group of transcription factors known as Heat Shock Factors (HSF). In mammalian cells, the main factor responsible for responding to environmental stress is HSF1 [165]. HSF1 resides in the cytoplasm as a monomer where, under normal conditions, it cannot bind to DNA. However, when the cell experiences thermal stress by overheating, HSF1 reacts to form a trimer which is phosphorylated and then translocated to the cell nucleus. In its trimeric state HSF1 can bind to DNA, specifically Heat Shock Promoter Elements (HSE) regions which leads to the transcription of these HSP genes. These newly transcribed HSPs then begin refolding the denatured cytosolic proteins. The downregulation of these proteins is caused by the interaction between a protein known as Heat Shock Binding Protein Factor 1 (HSBP1) and HSP70 together with HSF which prevents HSF from binding to the HSE [166–168]. A diagram of this cycle is shown in Figure 4.1.

Therefore, since HSP70 is only expressed when the cell is stressed it can be used as an indicator of stress. In fact, the expression of HSP70 itself is not necessarily

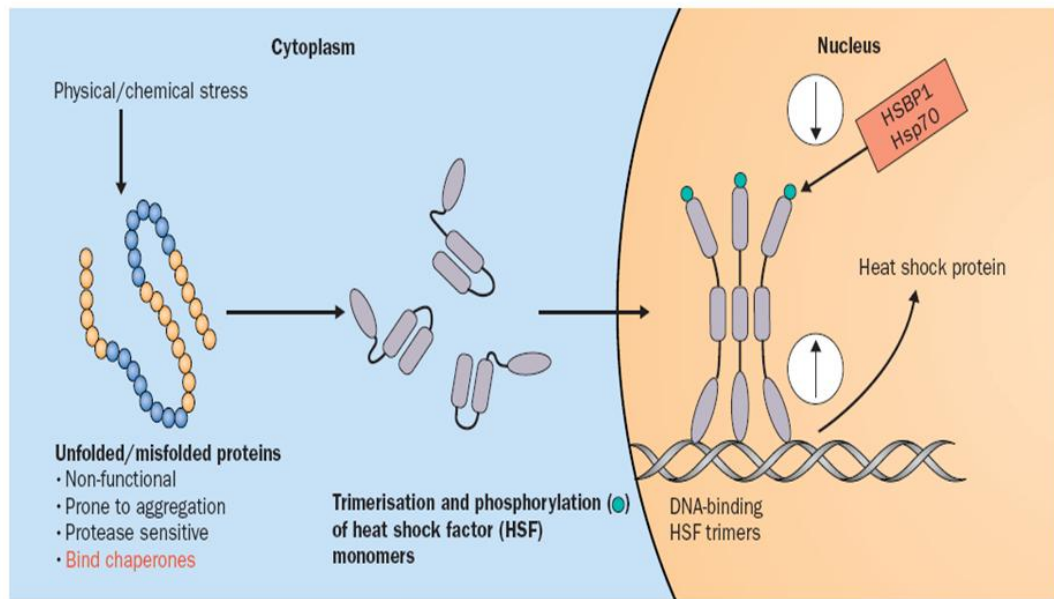


Figure 4.1: Induction and regulation of heat shock protein expression. Physical or chemical stress induces production of unfolded or misfolded proteins. Heat shock factor monomers in the cytoplasm form trimers, are phosphorylated, and translocate into the nucleus. HSF homotrimers bind to heat shock protein gene promoter regions, leading to induction of HSP gene transcription. HSP70 gene transcription is downregulated by interaction of HSP70 or HSBP1 with the HSF trimers. Image and caption reproduced in entirety from [168].

needed, only the detectable activation of its promoter. If a detectable marker could be switched on by the activation of the HSP70 promoter then it could be used as an indicator for activation of the HSP70 stress mechanism.

4.2.2.2 Green fluorescent protein

Green fluorescent protein (GFP) is a 27 kDa bioluminescent protein derived from the jellyfish *Aequorea victoria* that fluoresces green when excited by blue-violet light; it was first isolated in 1962 by Shimomura et al [169].

The wild-type protein (wtGFP) that exists in *Aequorea victoria* is excited by light of wavelength 395 nm (as well as a slight peak at 475 nm) and emits light of wavelength 509 nm. In the jellyfish, the wtGFP is excited by a Förster resonance energy transfer (FRET) from the photoprotein Aequorin which emits light

of wavelength 469 nm upon interaction with Ca^{2+} [170] [171]. Fortunately, wtGFP is not denatured when used at room temperature (but is denatured at 37 °C), but unfortunately it has poor spectral characteristics such as low quantum yield and photostability [172].

Once the coding sequence [173] and the molecular structure [174, 175] of GFP was uncovered and understood, it became possible to engineer a structure more conducive to laboratory conditions and experimental techniques. Chalfie et al [173] also showed that expression of the GFP gene in other organisms also results in fluorescent behaviour. This is significant because it shows that GFP does not need additional jellyfish enzymes or proteins to function. The first artificial improvement to GFP was reported in 1995 with a single point mutation (SPM) that changed the amino acid Serine 65 into Threonine was responsible for an increase in the amplitude of the excitation by 600% as well as a shift of the main excitation peak to 488 nm. [158]. The shift in the excitation peak was particularly useful because the spectral characteristics now matched those of the widely used Fluorescein isothiocyanate (FITC) filter and the molecule could now be excited by the commonly available Argon ion laser. A further SPM changing the amino acid Phenylalanine 64 to Leucine resulted in improved folding at 37 °C making it ideal for use in mammalian cells [176, 177]. This ‘optimised’ form of GFP is known as enhanced green fluorescent protein (EGFP) and it is the form that is most used today by researchers.

The first proposed use for GFP was put forward by Chalfie et al who suggested it could be used as a way to detect gene expression [173]. It is important to distinguish

two ways of achieving this and these are either by promoter tagging or fusion tagging [178]. In the former, GFP is combined with the promoter for the gene of interest, whose expression is to be monitored in the experiment. In this situation, whenever the cell upregulates expression of the gene of interest, a copy of GFP is also expressed which is not attached to the protein of interest and so accumulates in the cytosol where it is easily detected by fluorescent imaging. With this detection method, cells will glow homogeneously if the gene of interest has been upregulated. This method cannot tell you where in the cell the gene of interest is active.

In fusion tagging however, the gene of interest is combined with the GFP so that one molecule (a chimera of the two) is expressed. This means that the GFP will only be present where the active protein is present. For example, a cell with actin tagged GFP will indicate the subcellular localisation of actin. This type of tagging is useful for determining the location and fate of the tagged proteins. However, GFP will not fuse to every gene successfully as the function of the native protein can be inhibited by the addition of an extra 27 kDa molecule on it.

GFP has also be used alongside other fluorescent proteins in a Förster resonance energy transfer (FRET) analysis which can be used to indicate if two fluorescently tagged proteins get close enough to possibly interact with each other in the cell [179].

For my experiments, I used GFP fused to the promoter of HSP70 derived from a mouse. A promoter is a small DNA sequence typically located near the 5' region of an expressed gene and facilitates the transcription of the gene. In this case when the cell is induced to transcribe HSP70 (e.g. as a result of a stress event) then it

will also, separately, transcribe a copy of GFP as well.

4.2.2.3 HSP70-GFP

The first example in the literature of a GFP tagged HSP70 promoter was the 2000 publication titled “Laser-induced gene expression in specific cells of transgenic zebrafish” [180]. In this study, the authors attempted to use a laser source to induce the expression of GFP *in vivo* in a transgenic Zebrafish (*Danio Rerio*) transfected with a GFP tagged HSP70 promoter (also from a Zebrafish) plasmid. In this publication, Halloran et al reported the success of a focused laser beam to cause the expression of GFP within their target cell. Unfortunately, they did not publish the details of the laser they used in their study. Specifically, they did not make known the wavelength, the power or the beam profile of the laser; however, it is well known that lasers *can* be used to increase the temperature of a cell by photon absorption (this is the principle mechanism for the therapeutic use of a CO₂ laser to treat skin cancer [181] and other skin conditions like actinic cheilitis [182]).

The next example in the literature of the use of a GFP tagged HSP70 (promoter) is Vekris et al 2000 [183]. Their work aimed to show how artificial gene expression could be controlled by an externally applied thermal shock. Since HSP70 is expressed during thermal stress, and since it is possible to fuse the HSP70 promoter to other gene, it is therefore possible to artificially induce gene expression by activating the HSP70 stress pathway. The researchers successfully transfected rat C6 glioma cells with their constructed plasmid (known as pHot-Green) and showed that 24 hours after heating at 43 °C for 30 minutes, GFP is expressed (see Figure 4.2).

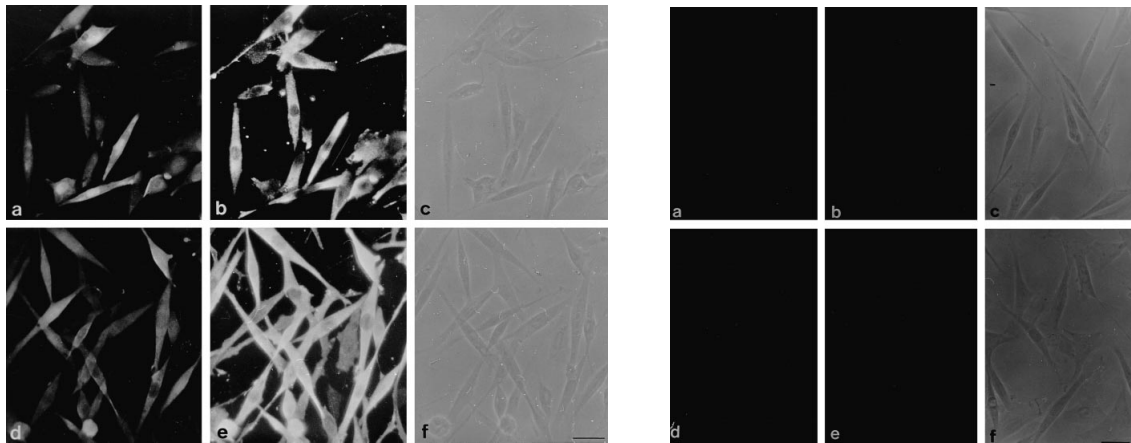


Figure 4.2: *GFP and hsp70 protein expression by the inducible C6 cell line after heat stress (left) and in non-stressed conditions (right). Left: C6 cells transfected with the plasmid pHot-Green were heat shocked at 43 °C for 30 min and observed after 24 h of recovery. (a-c) were taken from a single cell sample. GFP characterization was performed by intrinsic fluorescence (a) or by immunolabeling (b). (c) represents the phase contrast field of (a) and (b). d, e and f were obtained from a second sample. (d) and (e) show the intrinsic GFP fluorescence and the immunocharacterization of the hsp70 proteins, respectively. (f) is the corresponding phase contrast field of (d) and (e). The bar in (f) represents 25 μ m. Right: C6 cells transfected with the plasmid pHot-green expressing no detectable levels of the GFP and the endogenous hsp70 proteins when cultured in normal culture conditions. (a) and (b) show the lack of intrinsic GFP fluorescence and of GFP immunolabeling. (c) is the phase contrast field of (a) and (b). Similarly, no intrinsic GFP fluorescence and no hsp70 immunolabeling were visible in (d) and (e), respectively; (f) is the corresponding phase contrast field. Figure and caption reproduced in entirety from [183].*

Other examples in the literature include Wippersteg et al 2002 [184] who reported the successful transfection and heat induced expression of HSP70 promoter tagged GFP in *Schistosoma mansoni*, a type of flatworm. A study in 2004 used HSP70 tagged GFP (not just the promoter, this time it was the whole HSP70 gene) to discover where HSP70 accumulates in the cell during a stress event. They showed that when HSP70 is transcribed it accumulates mostly in the nucleus and they also showed that HSP70 has a reduced mobility when interacting with organelles in the cytosol [185]. Lipan et al used a GFP tagged HSP70 promoter in 2007 to study and mathematically model the response of the cell to a heat shock. They reported the development of a nonlinear stochastic model to explain the response of the GFP

expression in the CHOK1 cells they were studying [186]. It was from one of the authors on this paper, Dr Lei Haung of the Medical College of Georgia, USA, that I obtained the plasmid that was used for my experiments.

Finally, in 2006 another publication reported the successful expression of GFP by laser in *Drosophila melanogaster* transfected with GFP tagged HSP70 promoter [187]. Fortunately this time, details of the laser source were published and they used a wavelength of 532 nm (frequency doubled Nd:YVO₄) with a continuous wave power of 25 mW and a beam diameter of 2.41 mm. After exposing the wings of their transgenic flies to the laser for about 20 minutes they observed the fluorescent signal of GFP after 16 hours incubation. This shows that direct spatial and temporal control of artificial gene expression is possible using the HSP70 promoter. This implied that the lasers used for my experiments might also be capable of triggering a HSP70 response, especially since this group reported that a very low power density of $\sim 10 \text{ W} \cdot \text{cm}^{-2}$ was required (the power density in neuron growth experiments is $\sim 10^6 \text{ W} \cdot \text{cm}^{-2}$).

4.2.2.4 Plasmid construction and transfection

The plasmid used for my experiments was a generous gift from Dr Huang and is the same one used in Lipan et al 2007 [186]. Figure 4.3 is a diagram made from the relevant information on the plasmid extracted from their publication.

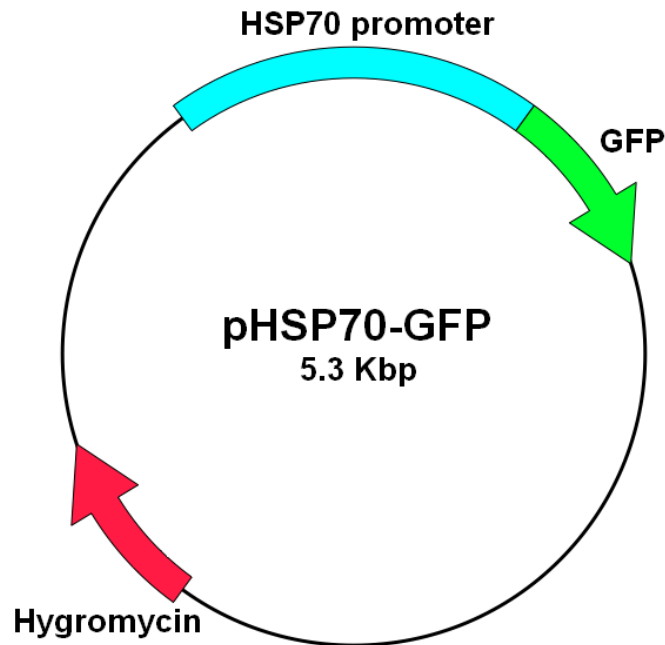


Figure 4.3: A 5.3-kilobase strand of DNA containing promoter and 5'-untranslated region of the mouse *hsp70.1* gene was subcloned from a lambda phage clone carrying an *hsp70.1* gene identified by genomic library screening (Stratagene) using a human *hsp70.1* cDNA as a probe. A cDNA coding for the GFP with a polyA signal from SV40 large T antigen gene was engineered to fuse to the start codon (ATG) of the *hsp70.1* gene. The chimera gene was inserted into a pSP72 vector containing a hygromycin resistance gene in order to select for stable transfectants. Caption reproduced from [186].

The plasmid contains HSP70 promoter tagged GFP and also a hygromycin resistance gene for selection purposes. The plasmid amplification and purification was carried out by my colleague Dr Lissa Rocha Herron who transformed DH5 α cells and then using this strain of bacteria used a QIAprep Spin Miniprep Kit according to manufacturer's instructions. This yielded approximately 100 μ L of DNA at a concentration of 0.22 μ g/ μ L.

I then transfected NG108's using a commercially available lipoplex transfection reagent called GeneJammer (Stratagene). In order to select for stable transfectants, the cell line was cultured in the presence of 0.5 mg/mL Hygromycin B (Invitrogen) 72 hours after transfection. This led to wide spread cell death but left, as expected,

a few cells which had integrated the plasmid into their genome. 48 hours later the cells were plated onto a 96 well plate so that on average only one cell would be in each well. This well plate was then fluorescently imaged to see if any cells were exhibiting a GFP signal. The well plate was then heat shocked at 42 °C for 35 minutes and imaged again 48 hours later. The cell that exhibited no signal before the heat shock and consequently the brightest signal post heat shock was selected and expanded by further cell culture. A large supply of the stably transfected cell line (now referred to as NG-108(pHSP70-GFP)) was cryopreserved to ensure a ready supply for any future experimentation.

4.2.3 Experimental procedure

The aim of this experiment was to determine whether a laser beam with properties (power, wavelength etc) similar to those used for optically guided neuronal growth, would cause sufficient heat or stress on a target cell to activate that cells defenses against stress. The stress indicator being used in this experiment was the GFP tagged HSP70 promoter, such that if a cell reached a point of stress sufficient to express HSP70, it would also express GFP.

In an experiment of this nature it is vital to have proper negative and positive controls as well as a carefully defined procedure.

4.2.3.1 Controls

Since we know from the literature that HSP70 will express in mammalian cells at exposure to temperatures greater than 42 °C, then we should expect to see GFP

expression in the transgenic cells exposed to this stress factor. Of course, continual exposure to 42 °C will kill the cells and too low an exposure may not produce enough GFP and so an exposure time of ~ 30 minutes is the recommended time in the literature for similar experiments [114–117]. Through a few basic experiments done before beginning the data collection I found that an exposure to a temperature of 45 °C for a time of 35 minutes produced the largest GFP response. Exposing cells to these conditions would be the positive control for these experiments.

The NG108 (pHSP70-GFP) cells were grown in an incubator as described in Chapter 2 and plated out onto 35 mm glass petri dishes at least 12 hours before experimentation. Three of these petri dishes were then placed in large petri dish which would then be hermetically sealed with Nescofilm (Alfresa Pharma, Osaka) to maintain a 5% CO₂ atmosphere (and thus pH balance). This large petri dish was then be placed in an oven preheated to 45 °C for a period of 35 minutes after which time the dish would be placed back in the incubator with the Nescofilm removed. After a further period of 48 hours these cells would then be examined in a microscope under the illumination of a mercury (Hg) lamp using a B-2A filter (Nikon).

For the negative control, NG108 (pHSP70-GFP) cells were prepared in an identical way to the positive control but the sealed large petri dish was then left in the incubator for 35 minutes after which time the Nescofilm was removed. Cells were then viewed under Hg illumination after 48 hours.

4.2.3.2 Main experiment

For the main experiment, NG108(pHSP70-GFP) cells were prepared identically to those for the controls except that the seeding density was lower so as to produce samples with sufficiently isolated single cells. After being plated out on to the 35 mm glass bottomed petri dish, it was then hermetically sealed with Nescofilm and placed onto the heated microscope stage setup as described in Chapters 2 and 3. Here, the cells could be kept in incubator-like conditions for long periods of time although for these experiments the cells were only on the stage for 35 minutes to keep the procedure as close to that for the controls as possible and because this was a typical exposure time for a laser guidance experiment. Though several cells were present on each petri dish at a time only one cell was experimented on per dish. A cell was chosen for experimentation if it looked healthy and was sufficiently separated from other cells (defined as roughly two fields of view in any direction) so it could be identified again 48 hours later for the fluorescent imaging. The location of the cell was marked manually using a diamond tipped drill bit to etch a mark on the bottom of the petri dish. This allowed me to be sure that any cell found in the marked region after 24 hours was either the original cell or a daughter or it.

Once on the stage, I simulated a typical neuronal growth experiment by irradiating an edge of an NG108 with a 100 mW 1.5 μm diameter Gaussian beam from a 1070 nm Ytterbium fibre laser for a period of 35 minutes. The laser power used for neuron growth experiments from the literature vary from 8 mW [117] to 120 mW [114,116]. 100 mW was chosen because of the previous literature and to max-

imise the possibility of a heat shock response. The NG108(pHSP70-GFP) cells were then examined 48 hours later for any increase in GFP expression.

4.2.4 Results

Shown in Figure 4.4 are examples of a typical positive control. As can be seen approximately 20% of the cells are showing GFP expression. It is also worth noticing the amount of cells which are dead and not showing GFP expression. This demonstrates that the heat shocking control can be fatal. Also shown in Figure 4.4 are examples of a typical negative control which show no detectable GFP expression

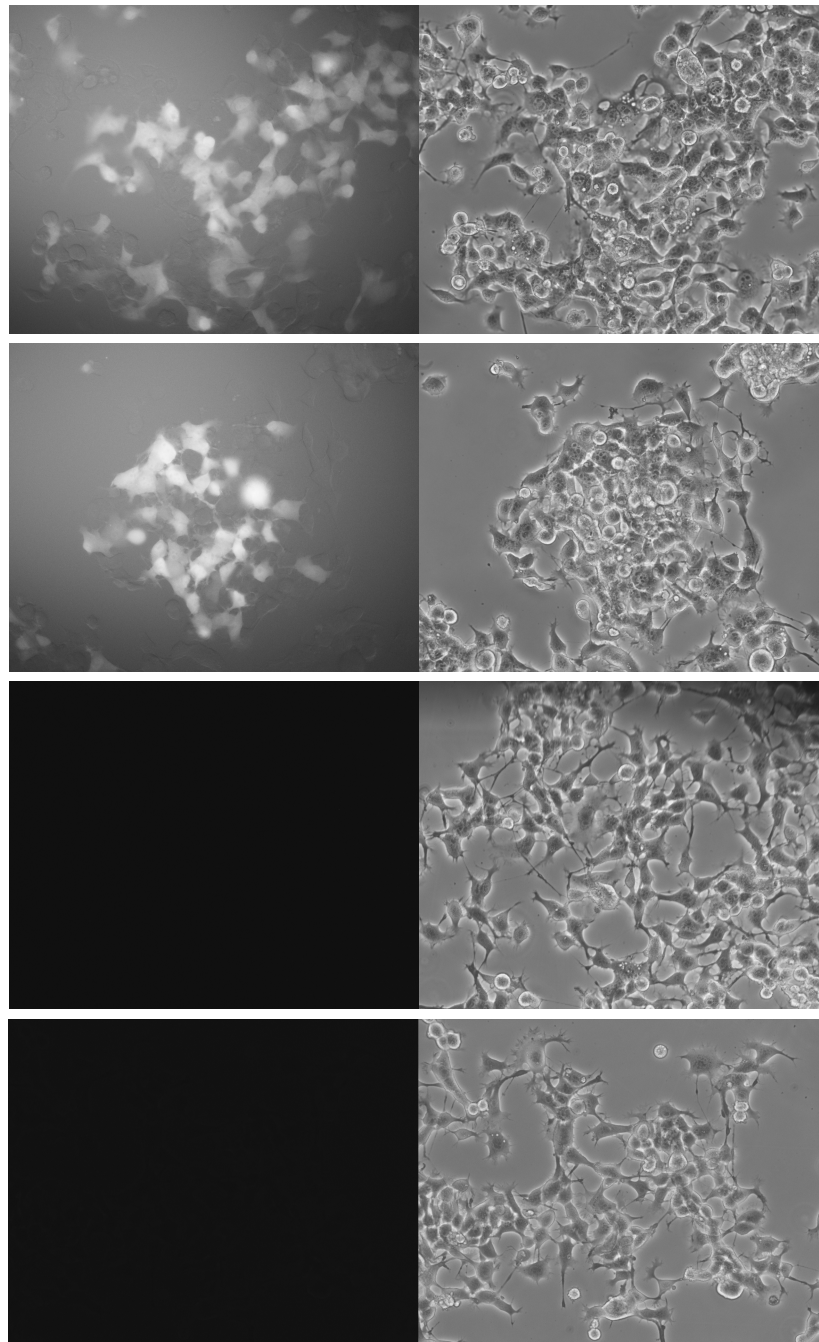


Figure 4.4: *Top two images: Typical results of positive control. On the left is the fluorescent image produced by the GFP in the cells, on the right is a phase contrast image of the same sample without Hg illumination. In both cases, approximately 20% of the NG-108(pHSP70-GFP) are exhibiting a GFP response. Both samples also contain several dead cells. Bottom two images: Example results of the negative control. On the left is the image taken under fluorescent illumination, on the right is a phase contrast image of the same sample without fluorescent illumination. As can be seen, there is no detectable GFP signal from the NG-108(pHSP70-GFP).*

The results of the main experiment were also negative for the induction of GFP

expression. The experiment was repeated 28 times and no fluorescent signal was observed in cells that had been exposed to 100 mW of laser radiation for 35 minutes. The results are tabulated in Table 4.2. and shown in Figure 4.5 are a few examples showing this result. If the cells were being heat shocked then we would expect approximately 20% of the 28 cells to be fluorescent.

| Experiment number | GFP signal | Experiment number | GFP signal |
|-------------------|------------|-------------------|------------|
| #1 | None | #15 | None |
| #2 | None | #16 | None |
| #3 | None | #17 | None |
| #4 | None | #18 | None |
| #5 | None | #19 | None |
| #6 | None | #20 | None |
| #7 | None | #21 | None |
| #8 | None | #22 | None |
| #9 | None | #23 | None |
| #10 | None | #24 | None |
| #11 | None | #25 | None |
| #12 | None | #26 | None |
| #13 | None | #27 | None |
| #14 | None | #28 | None |

Table 4.2: Results of exposing NG-108(pHSP70-GFP) to 100 mW of laser radiation for 35 minutes. After 48 hours no GFP signal was seen in contrast to the positive control.

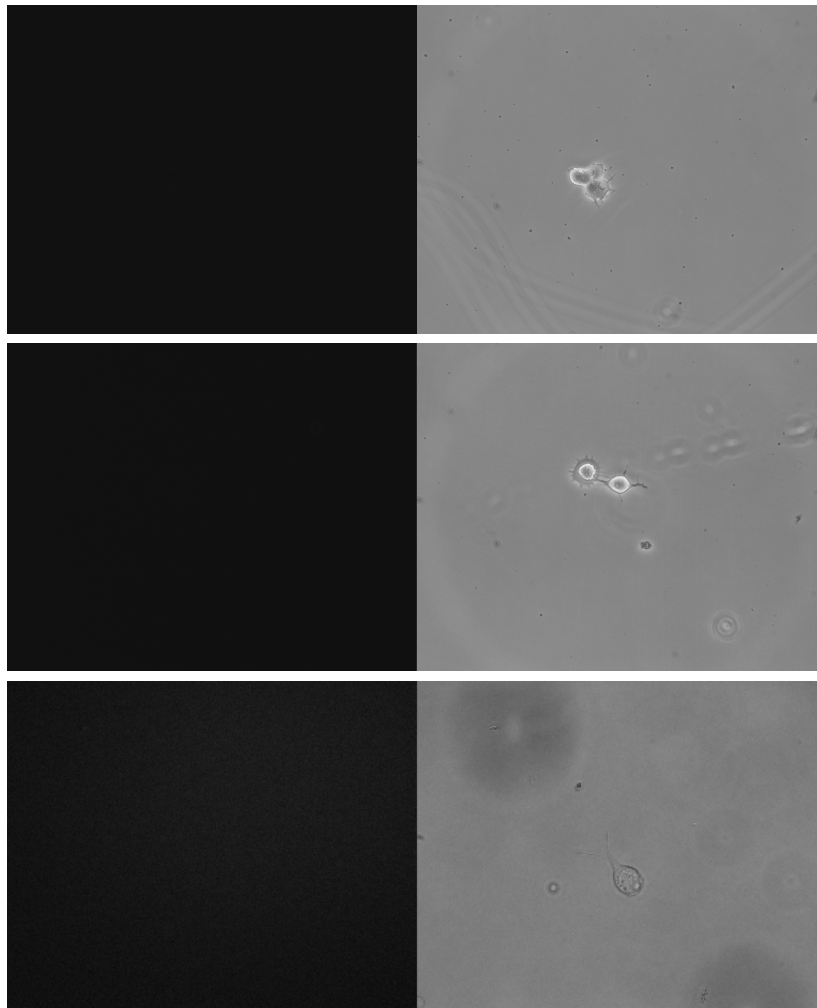


Figure 4.5: *Three examples of main experimental results. The left pane shows is an image of the right pane under fluorescent illumination. As can be seen there is no detectable GFP signal. The right pane shows the same as the left pane under brightfield illumination. In some instances there are two NG-108(pHSP70-GFP) cells visible, this is attributed to cell division of the single cell that was experimented on. The fact that they are dividing can also be used as a measure of how unharmed the laser radiation we are using is.*

As Figure 4.5 clearly shows, there is no increase in GFP signal in NG-108(pHSP70-GFP) after being exposed to laser radiation of power and duration typically used in optically guided neuronal growth experiments.

4.2.5 Conclusion and discussion of heat shock experiments

These experiments indicate that HSP70 expression is not being induced during the neuronal growth experiments under irradiation from a typical laser source.

This study would at first seem to contradict the research done by Ramos et al [187] who showed that a laser of low power could stimulate cells to elicit a heat shock response. However, some crucial differences between this experiment and their work needs to be highlighted. Firstly, they are using a wavelength (532 nm) which has a stronger absorption in organic material (See Chapter 1.3.2 for a discussion on laser wavelengths and biological viability). They also performed the experiments *in vivo* and as such they had multiple layers of cells (as opposed to a monolayer) so that any light that isn't absorbed by the first layer of cells will be absorbed by consecutive ones. They also performed the experiments on *Drosophila melanogaster* which expresses HSP70 at 37 °C whereas mammalian cells express HSP70 at 42 °C.

My results indicate for the first time that HSP70 is not up-regulated during a laser guidance experiments and this study is only the second ever experiment to determine whether or not heating effects are responsible for (or play a part in) optically guided neuronal growth (the previous study being Stevenson et al 2006 [117] which is discussed in chapter 1.5.3). This study clearly shows that cells under laser irradiation, of powers typically used in experiments, are not being stressed sufficiently enough (if at all) to trigger an up-regulation of HSP70 which strongly suggests that HSP70 is not involved in the mechanism for optically guided neuronal growth. While this study cannot completely rule out the possibility of any thermal

effects being involved in optically guided neuronal growth, it at least puts an upper bound on how high the amount of heating is, i.e. less than the minimum to trigger an HSP70 response which, in mammalian cells, is equivalent to a temperature less than 42 °C. This result is in agreement with the previous study which only reported a temperature of $\sim 1-3$ °C [117] (discussed in Chapter 1.5.3).

This study is also the first attempt to directly measure whether or not a laser typically used for optical tweezing could illicit a stress response in a cell. Whilst only HSP70 was tested here it is possible that another stress pathway is being activated. A more comprehensive study using other transgenic cell lines could be used to investigate other stress pathways and the possible stress effects of other laser-cell interactions in the field of biophotonics such as photoporation or caged compound experiments.

4.3 Chemical pathway inhibition

4.3.1 Introduction

In this section, I will detail my investigations into optically guided neuron growth by inhibiting certain key pathways in the cell. As previously discussed in chapter 1, the cell is controlled by complex sequences of chemical events that begin with a stimuli and end in a response. For example, in the previous section I investigated one of the heat shock pathways which is activated by the cell after being heated (stimuli) and then, via a chemical pathway, produces a heat shock protein(s) to protect itself (response). The growth cone is responsive to many chemical stimuli that result in

changes to the cytoskeleton e.g. Netrin, laminin etc (see chapter 1.4.3.1). This is made possible by the existence of a chemical pathway in the growth cone that controls the cytoskeleton (e.g. actin polymerisation/depolymerisation) in response to the presence of a chemical input. If, as I suggested in Chapter 2, the primary mechanism for optically guided neuronal growth is the alignment of filopodia due to optical trapping, and not due to any interference with chemical pathways, then it follows that if certain pathways responsible for the production of actin filaments at the leading edge (and thus filopodial outgrowth) were inhibited then the laser should be incapable of guiding the neuron.

The experiments described in this section show that when under laser irradiation, active growth cones still collapse when certain proteins are inhibited. This suggests that the presence of the laser is not interfering in the normal operation of the chemical machinery of the cell as has been suggested in previous literature [114,117]. Two inhibitors were chosen for experimentation and they were LY294002 and UO126 which inhibit phosphatidylinositol 3-kinase (PI3K) and mitogen-activated protein kinase kinase (MEK1) respectively. The result of using these two protein inhibitors was as expected, filopodia production was crippled and in many cases the growth cone collapsed entirely. This was despite the presence of a laser spot used to initiate guided growth, which suggests that indeed, the phenomenon of optically guided neuronal growth can only work when those chemical pathways are working.

4.3.2 Introduction to chemical pathways

I include here a brief overview of the chemical pathways with emphasis on those relevant to the experiments described in this chapter. The chemical pathways that exist in a cell are collectively called the metabolic network. A metabolic network is the complete set of metabolic and physical processes that determine the physiological and biochemical properties of a cell. As such, these networks comprise the chemical reactions of metabolism as well as the regulatory interactions that guide these reactions. Metabolic pathways are responsible for every chemical process in a cell such as anaerobic respiration, glycolysis, oxidative phosphorylation and the krebs and urea cycles.

With the sequencing of complete genomes now available, it is possible to reconstruct the network of biochemical reactions in many different organisms, from bacteria to humans. Indeed, several of these networks have been published and are available online such as the Kyoto Encyclopedia of Genes and Genomes (KEGG, <http://www.genome.jp/>).

4.3.2.1 The mitogen-activated protein kinases

Mitogen-activated protein kinases (aka MAPK's, MAP kinases or ERK kinases, referred to from here on as MAPK's) are a family of proteins that respond to extracellular stimuli (e.g. mitogens, heat shock, growth factors) and regulate various cellular activities, such as gene expression, mitosis, differentiation, proliferation, and apoptosis [188]. They exhibit a large degree of homology across all Eukaryotic life

and are of particular importance to axon growth and generation [189–191].

The pathway for MAP kinases is complex and Figure 4.6 shows a diagram of some of the paths that have been identified to date in vertebrates. The MAPK pathway is responsible for coupling intracellular responses (such as the growth of the cytoskeleton [154, 155]) to the detection of various growth factors at the cell membrane such as Nerve Growth Factor (NGF) and Netrin-1 [192]. Inhibition of certain MAP kinases has been shown to affect cell growth and proliferation [193, 194]. For example, Pang et al showed that inhibiting MAP kinase kinase (aka MEK1/MAP2K referred to from here onwards as MEK1) in PC-12 cells using the inhibitor PD98059, rendered them unable to differentiate in the presence of NGF [194]. Ming et al showed in 2002 that inhibition of this same protein using PD98059 and UO126 on *Xenopus* spinal neurons led to them being unable to react to the presence of Netrin-1 (a common guidance cue, see Chapter 1.4.3.2) [195]. This is because the receptor Netrin-1 activates (DCC) in turn activates RAC1 (Ras-related C3 botulinum toxin substrate 1) which goes on to activate MEK1. With inhibition of MEK1 the cell becomes insensitive to Netrin-1. In 2000, Sjögreen et al also showed that inhibition of MEK1 using PD98059 blocks axonal outgrowth on mouse dorsal root ganglia (DRG) cells [196]. These studies show that inhibition of the MEK1 blocks the growth cone from developing and another study has shown that it causes the growth cone to collapse entirely [197].

4.3.2.2 Phosphatidylinositol 3-kinases

Phosphatidylinositol 3-kinases (PI 3-kinases) are a family of proteins involved in several vital cellular functions such as growth, motility, differentiation and apoptosis. PI3K's are instrumental in several metabolic pathways including phosphatidylinositol signalling, neurotrophin signalling, focal adhesion and actin cytoskeleton regulation. Their involvement in these last two pathways mean they play important roles in the growth and migration of neuronal cells [156]. PI3K is also indirectly connected to MEK1 via RAC (RAC1) as shown in the pathway diagram in Figure 4.7 and continuing in Figure 4.6.

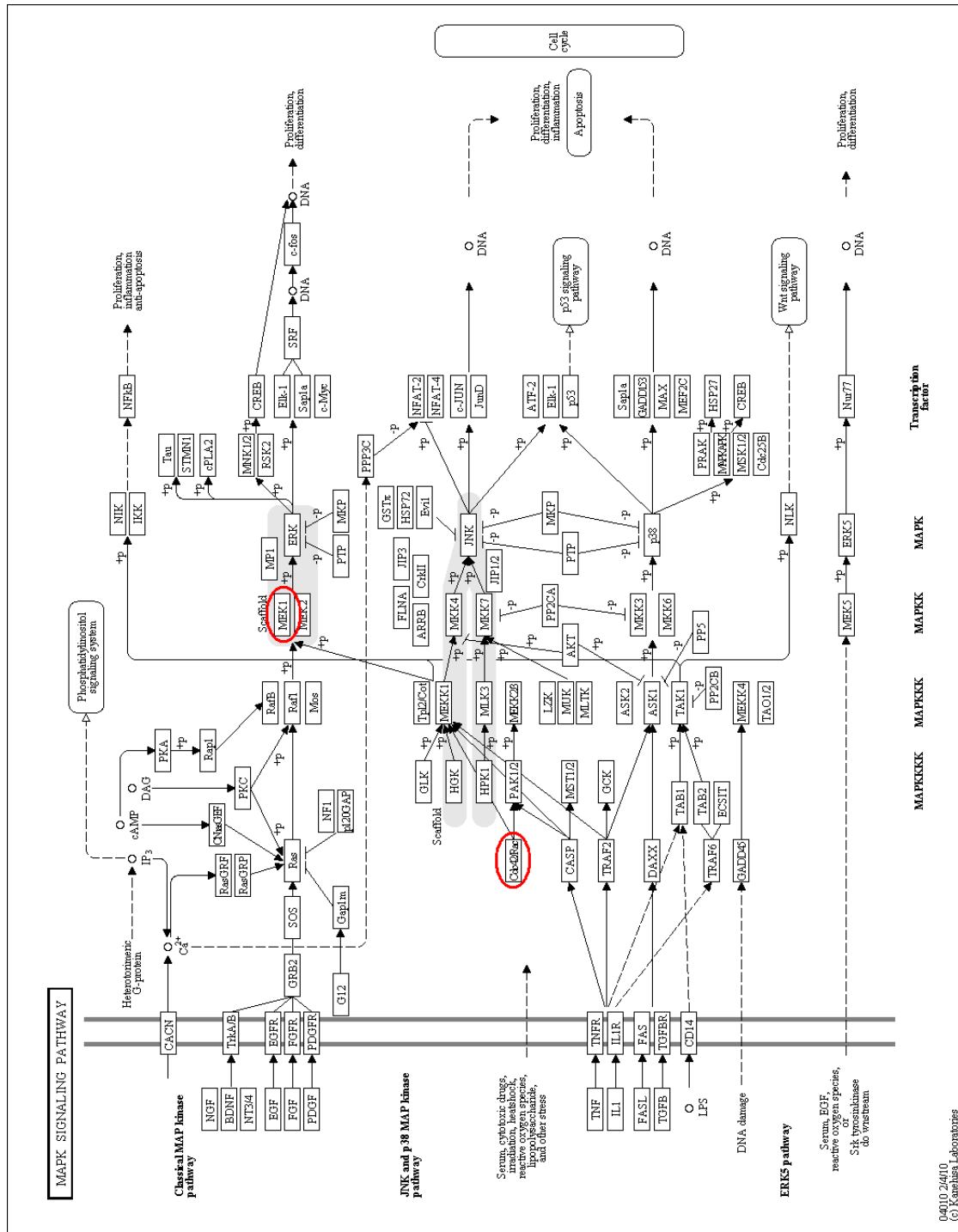


Figure 4.6: Diagram of identified MAP kinase pathways. Diagram shows nuclear and cell membranes and associated transmembrane proteins. Of particular interest is the MAPK/ERK pathway that is responsible for the cell responding to growth factors. A good example of this is the pathway associated with Nerve Growth Factor (NGF) which affects cell growth and proliferation. NGF is important for neuron survival [198]. Image reproduced from KEGG (<http://www.genome.jp>). Highlighted in red circles are MEK1 and RAC1.

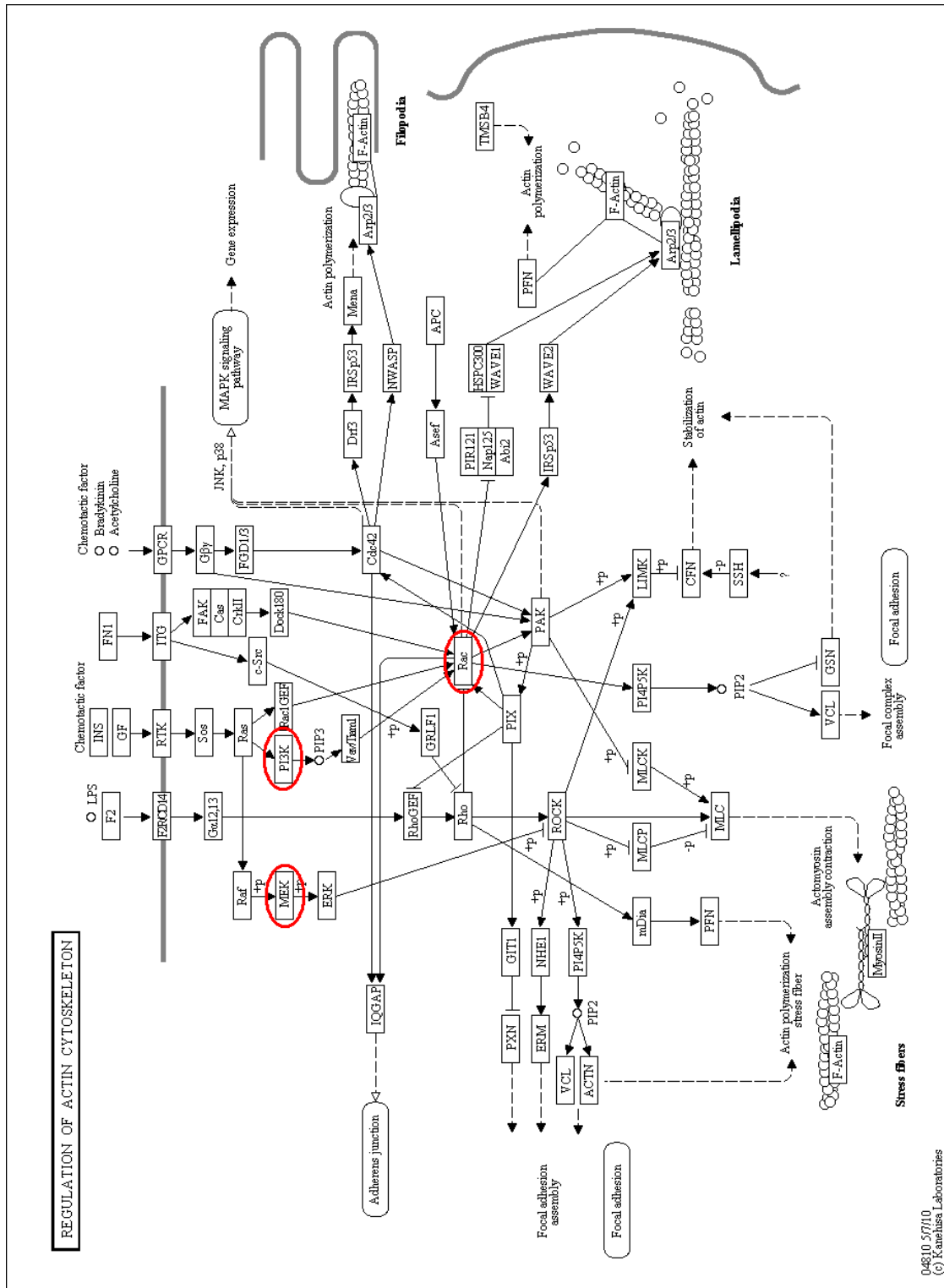


Figure 4.7: Diagram of protein interactions that regulate the actin cytoskeleton. MEK1, PI3K and RAC1 are highlighted with red circles. Image reproduced from KEGG (<http://www.genome.jp>).

Inhibition of PI3K in neuronal cells has been shown to arrest the expansion of

the membrane at neuronal growth cones [199]. A subunit of PI3K has also been linked to actin formation via interaction with the CDC42 protein [200]. Inhibition of PI3K with LY294002 has been shown to result in growth cone collapse [201]. From the literature, it is obvious that the MEK1 and PI3K pathways are prerequisite for growth cone development and when they are inhibited, growth cones are adversely affected and even collapse. For these reasons it was interesting to know that under these conditions if the growth cones would still collapse whilst in the presence of a laser designed to guide it. If, as the model in chapter 2 supposes, the existence of extending filopodia are necessary for guided growth to take place then in the presence of these inhibitors guided growth should not be possible. However, if the laser is affecting the biochemistry of the cell then it's plausible that the inhibitors may not be effective and guided growth may still occur.

PI3K and MEK1 protein were inhibited under experimentation by the compounds LY294002 and UO126 respectively.

4.3.3 Inhibitors used

4.3.3.1 UO126

UO126 is a highly selective inhibitor of MEK1 and MEK2 with an IC_{50} of 72 nM for MEK1 and 58 nM for MEK2. A diagram of UO126 is shown in Figure 4.8. For my experiments I used UO126 purchased from Sigma-Aldrich (product code U120-5MG) which has the chemical formula 1,4-Diamino-2,3-dicyano-1,4-bis(o-aminophenylmercapto)butadiene monoethanolate or $C_{18}H_{16}N_6S_2 \cdot C_2H_5OH$ and a

molecular weight of 426.56 g/mol [202]. This inhibitor was made soluble using 100% dimethyl sulfoxide (DMSO) and stored at 2 °C for no more than one month.

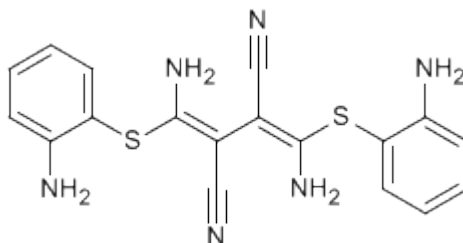


Figure 4.8: *Molecular structure of UO126.*

4.3.3.2 LY294002

LY294002 is an inhibitor of phosphatidylinositol 3-kinases (PI3K/PI 3-kinases) with an IC₅₀ of 1.4 μM. A diagram of LY294002 is shown in Figure 4.9. For my experiments I used LY294002 purchased from Calbiochem (product code 440202-5MG) which has the chemical formula 2-(4-Morpholinyl)-8-phenyl-4H-1-benzopyran-4-one C₁₉H₁₇NO₃ and a molecular weight of 307.4 g/mol [203]. This inhibitor was made into solution using H₂O (>5 MΩ ionic purity) and stored at -20 °C for no more than four months.

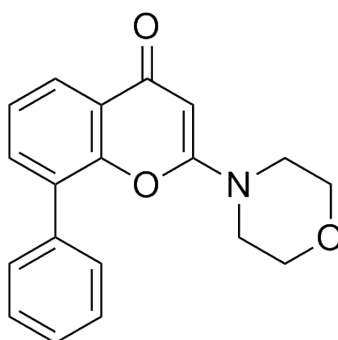


Figure 4.9: *Molecular structure of LY294002.*

4.3.4 Experimental procedure and results

The procedure for this experiment was to expose neurons to key protein inhibitors whilst under the irradiation of a laser for guiding growth cones and then observe if the laser could still guide the growth cone. The experimental setup was as described in chapter 3 and is shown in Figure 3.5.

The key difference about this new setup was the procedure of adding a chemical mid-way through an experiment. All my other experiments have been performed using sealed modified Carrel flasks (see Figure 2.1) to maintain sterility and the pH balance. To maintain these conditions whilst also allowing for the addition of a small volume of liquid proved to be a technical challenge.

The Carrel flask that I had assisted my colleague Dr David Stevenson in designing was modified to allow the exchange of fluids between the main sample chamber and an attached syringe. This was made possible by the addition of two holes drilled into the cap that allowed the attachment of plastic tubes that could be attached to a syringe. The tubes could be closed by use of a plastic peg. A photograph of this device is shown in Figure 4.10. This innovative design was published in *Microscopy and Analysis* [121].

Using this modification, an inhibitor could be added whilst the sample chamber was on the heated microscope stage with minimum disruption and with sterility maintained.

The experimental procedure was as follows: first, a suitable growth cone was located. Suitable was defined as a growth cone that was actively growing for more

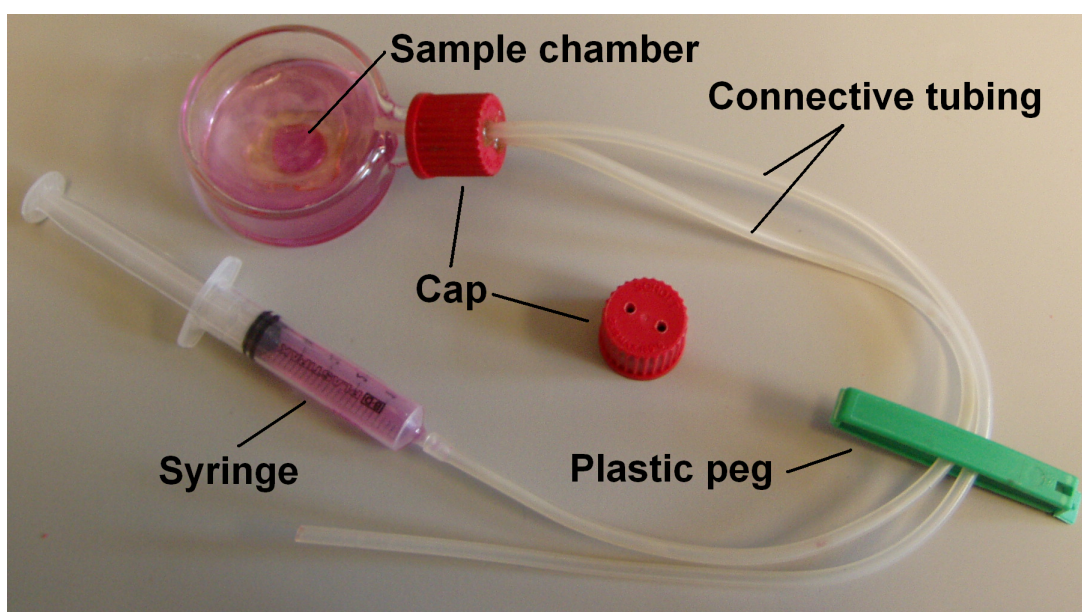


Figure 4.10: *Photograph of the modified Carrel flask with chemical injection system attached. The flask is as shown in Figure 2.1 but with a modified cap attached. This cap has two holes drilled in it as can be seen on the top down view of one in the picture above. Plastic tubing is fed through these holes and sealed with epoxy-resin to produce an air-tight seal. One of these tubes is connected to a syringe with a chemical preloaded in it. The other tube is used as an exhaust so that the pressure in the sample chamber remains constant. The plastic peg is removed only during the injection and is replaced immediately afterward forming an air-tight seal.*

than 10 minutes (as previously described in chapter 2.2.2). The laser spot would then be applied to the leading edge of the growth cone. This would be maintained for a few minutes to make sure the growth cone did not collapse, only then would the inhibitor be added. This was done by unfastening the plastic peg in Figure 4.10 and closing the syringe gently until all of the liquid was in the sample chamber. The peg was then immediately fastened and the experiment would continue as normal (see chapter 2.2.2).

The inhibitor was stored in 2 ml of cell media in the syringe which, when added to the sample chamber, brought the concentration of the total volume to that desired by the experiment. For example, for a final LY294002 concentration of 3 μM in the sample chamber, 2.14 μL of stock (concentration 7 mM) would be added to 2 mL cell media and loaded into the syringe. This would then be injected into the sample chamber which already contained 3 mL of media (bringing the total volume to 5 mL) giving a final concentration of 3 μM (twice the IC_{50} [204]).

The concentrations chosen for use were derived from examples used in the literature. The IC_{50} of LY294002 is 1.4 μM [204] and similar levels of this concentration have been used in previous experiments in blocking PI3K [205, 206]. A concentration of 3 μM was also chosen for experimentation on because of previous usage in the literature [207, 208]. It was observed that these concentrations were more than sufficient to severely impair the ability of the NG-108 cell line to grow and higher concentrations were not used.

The reported IC_{50} of UO126 is 72 nM for MEK1 and 58 nM for MEK2 [209]. 60

nm was chosen for use so as to be close to both IC_{50} levels and because of usage in the literature [210, 211]. The concentration of 10 μ M was also used because of the previous usage in the literature [212–215] and concentrations of 120 nm and 1.2 μ M were also used so as provide a range between 60 nm and 10 μ M. Since an effect was clearly observable for these experiments no higher concentrations were used.

As in the previous section, appropriate controls were necessary to make sure the effect being observed was attributable to the inhibitor compounds. The negative control involved performing optically guided neuron growth and injecting a “placebo” (2 mL of cell media without inhibitor) from the syringe into the sample chamber. The positive control was done by observing the cells growing without the presence of a laser and then injecting the inhibitor. As expected, in controls with the inhibitor cell growth was adversely affected and in controls without inhibitor there was no observable change.

4.3.4.1 Results

The effect of adding either inhibitor at concentrations equal to or greater than the IC_{50} was a visible reduction in the outgrowth of filopodia and often a complete collapse of the growth cone regardless of the presence of the laser.

In 12 experiments, addition of LY294002 caused the active growth cone to stall and sometime collapse entirely. UO126 showed the same result in 8 experiments. Shown in Table 4.3 is the collated results of these experiments and shown in Figure 4.11 is an example sequence of the effects of adding LY294002 or UO126 to NG-108 cells in the presence of a laser.

| Inhibitor | Concentration | Growth cone stall? |
|-----------|---------------|--------------------|
| LY294002 | 1.4 μ M | Yes |
| | 3 μ M | Yes |
| | 3 μ M | Yes |
| | 3 μ M | Yes |
| | 3 μ M | Yes |
| | 3 μ M | Yes |
| | 3 μ M | Yes |
| UO126 | 60 nM | Yes |
| | 120 nM | Yes |
| | 1.2 μ M | Yes |
| | 10 μ M | Yes |
| | 10 μ M | Yes |

Table 4.3: Collated results of inhibitor experiments.

Positive controls showed the same behaviour at similar concentrations and at higher concentrations, and neurite growth was inhibited within a shortened timespan and there was a higher occurrence of full neurite retraction. Shown in Figure 4.12 is an example of inhibitor addition without the presence of a laser at the same concentrations as those shown in Figure 4.11.

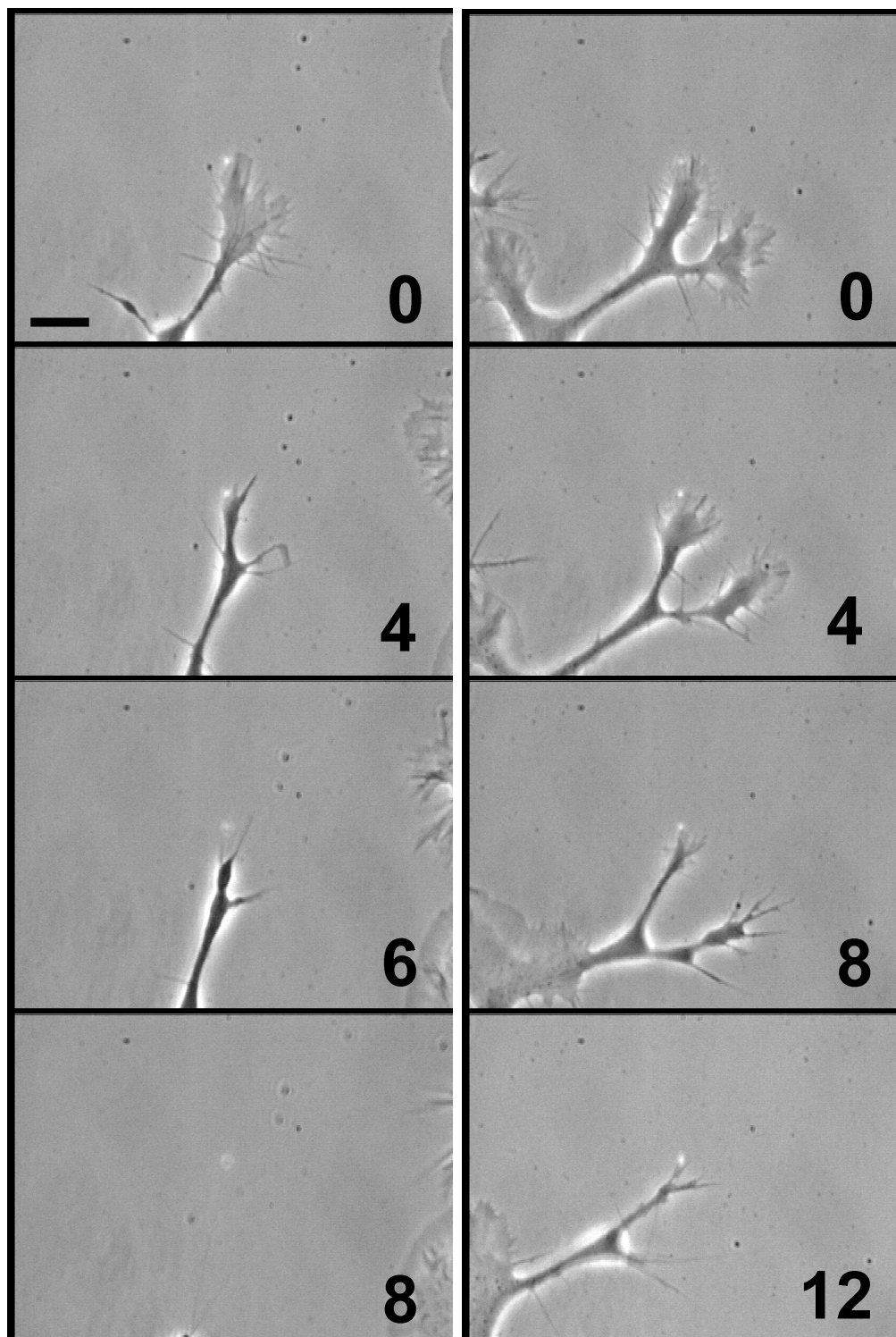


Figure 4.11: Example of results of inhibitor addition. Images progress from top to bottom, the number represents the time in minutes. The inhibitors were added in the second frame of each sequence. Left: LY294002 at a concentration 3 μM . Right: UO126 at a concentration 60 nM. Scale bar is 10 μm . A video of these experiments is included in the CD accompanying this thesis.

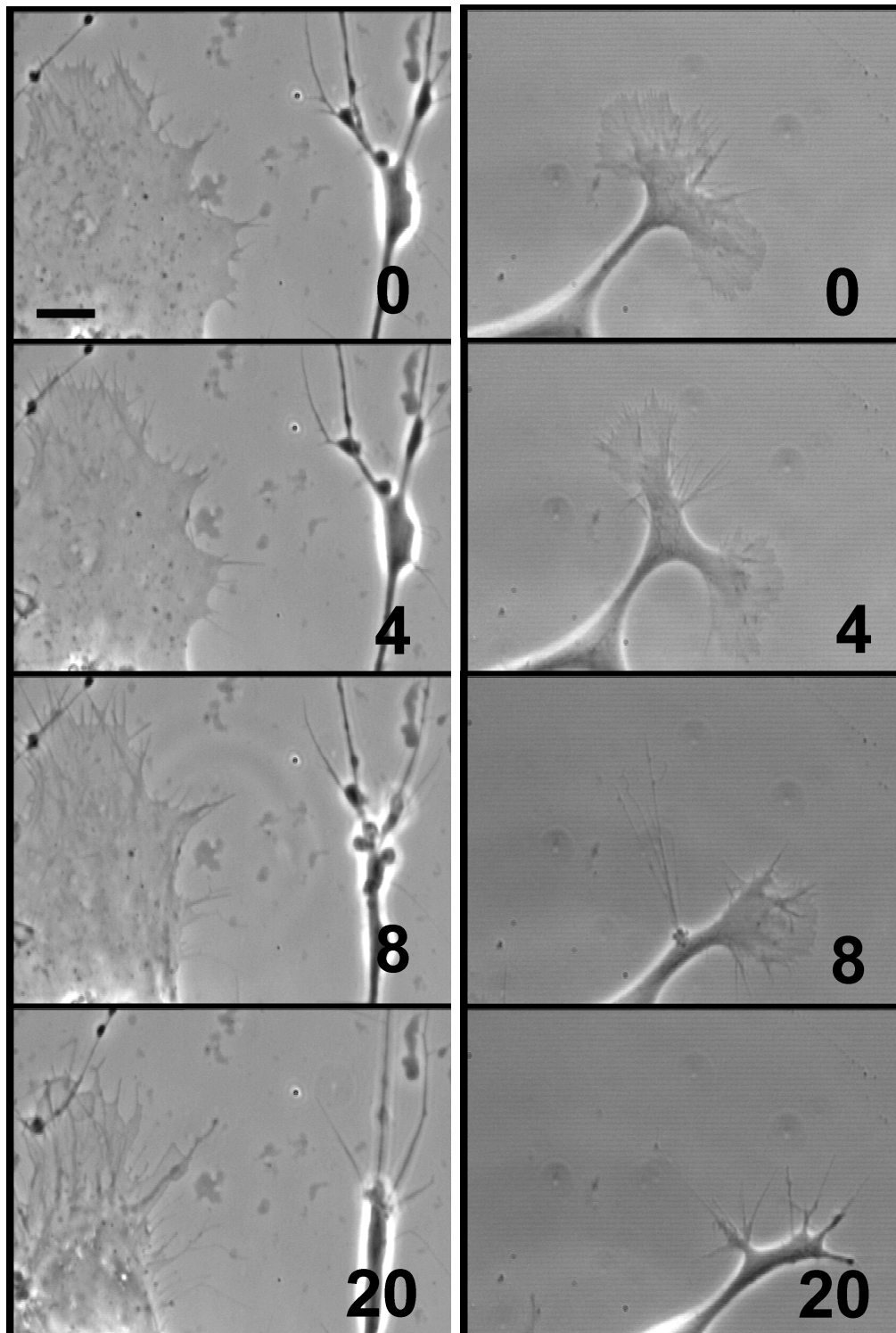


Figure 4.12: *Effect of adding inhibitor without laser. Images progress from top to bottom, the number represents the time in minutes. The inhibitors were added in the second frame of each sequence. Left: LY294002 at a concentration of 3 μ M. Right: UO126 at a concentration of 60 nM. Scale bar is 10 μ m.*

As can be seen in Figure 4.11, the developing growth cones are observably re-

tarded and collapse entirely once the inhibitor had been added. The same result is also seen in the absence of the laser in Figure 4.12.

4.3.5 Conclusion and discussion of protein inhibition experiments

These results confirm that the presence of a laser beam of the sort used for optical guidance experiments does not prevent growth cone collapse and retraction due to the addition of chemical inhibitors LY294002 and UO126.

My results here are in keeping with the results of previous studies done on growth cones using these inhibitors. In particular, the work of Chadborn et al [201] and Laurino et al [199] who showed that inhibition of PI3K with LY294002 led to growth cone collapse at similar concentrations. The results of inhibiting of MEK1 also echoes the work of Atwal et al [197] and Sjögreen et al [196] who showed that growth cone development is adversely affected and can collapse entirely.

Initially, I had chosen PD98059 for inhibition of MEK1 since it is more established in the literature. However after several preliminary experiments it was discovered that the concentration of DMSO required to dissolve PD98059 proved to be sufficient to adversely affect the NG-108 growth cones. Because of this it could not be determined if the growth cones were collapsing due to the inhibition of MEK1 or the presence of DMSO. UO126 is also soluble in DMSO but much more readily and so the amount of DMSO being added to the sample was much less than what was needed to observe an adverse reaction.

The aim of this experiment was to eliminate a possible chemical pathway that was possibly being affected by the presence of the laser beam. The results show that the laser is not adversely affecting these pathways to the point where their inhibition does not preclude growth cone development. These experiments are further evidence that the mechanism for optically guided neuronal growth is not due to the laser interfering with the cellular machinery of the cell. The choice to inhibit MEK1 and PI3K was because of their demonstration in the literature to be necessary for growth cone development and that inhibition of these proteins did not lead to cell death. There are many other proteins that could also be studied in this way (far too many to list them all) for example cAMP-dependent protein kinase A (PKA) which when inhibited has also been shown to retard growth cone development [216]. Another example for a protein worthy of investigation would be Cell division control protein 42 homolog (CDC42). This is another protein important to nerve growth which has been shown to affect the proliferation of PC-12 neurite cells via interaction with NGF [217] (see Figure 4.6 and Figure 4.7 for more potential examples).

The original model proposed by Ehrlicher et al suggested that individual actin monomers were being pooled by the optical potential well of the laser. Ehrlicher et al also suggested that perhaps other cytosolic proteins were being pooled in this manner and that this was a possible cause for optically guided neuronal growth, even though their own mathematical calculations predicted very weak forces (see Chapter 2.3.1). If the lasers used are too weak to pull actin monomers then it suggests they are also too weak to be pooling other cytosolic proteins. Indeed, only microstructures

such as filopodia are large enough to experience a strong enough optical force to be affected (see Chapter 2.3.2). If the laser is not pooling these cytosolic proteins then perhaps they are affecting them in other ways such as altering them photochemically. Though this would seem to be in contrast to the work of Neuman et al [45] who conducted experiments on the sensitivity of cells to laser wavelengths and reported relatively lower sensitivities (as measured by LD₅₀ and cloning efficiency) for the wavelength used in my experiments (1070 nm) compared to other wavelengths in the NIR range (790-1100 nm).

Taken together, these considerations strongly suggest that further experiments into inhibiting other proteins involved in growth cone dynamics will not result in any unexpected observations due to the presence of the laser.

Chapter 5

Conclusions and discussion

This thesis began with a brief introduction to optical trapping and its application to the growing field of Biophotonics and a review of selected publications in this area. This also included a discussion on the considerations of laser wavelength to the viability of cells and a discussion of laser sources appropriate for biological use. A brief introduction to the biological cell was also included here with specific interest paid to the cytoskeleton and actin treadmilling. Because of their importance to the work in this thesis, particular emphasis was paid to a discussion of neuronal cells and included the role of the cytoskeleton and action potentials in their development. Finally, a discussion of key publications on optically guided neuronal growth completed the introduction chapter to this thesis. These publications included the original work by Ehrlicher et al in 2002 [114] which was to form the foundation of the mathematical model of filopodia in an optical potential well explored in Chapter 2 of this thesis and the work of Mohanty et al in 2005 [116] which inspired our investigation of beam shape on neuronal growth.

Chapter 2 detailed my experiments into line optical tweezers on neuron growth. As mentioned, the motivation for this study came from the work of Mohanty et al who in 2005 reported a bias in the ability of line tweezers to guide growth cones depending on the line profile [116]. They attributed this bias to a proposed model of actin flow that involved the line profile acting as a ‘sling-shot’ and propelling actin monomers out of the optical potential well. This meant that the flow of actin could be directed by the laser as opposed to just being attracted to the laser as per Ehrlicher et al’s explanation [114]. This implied that if actin could be directed towards the leading edge by a certain orientation of line profile, then presumably actin could also be directed away from the leading edge by reversing the beam. My experiments directly compared the ability of three different line configurations (forward bias, reverse bias and symmetrical see Chapter 2.2.1 and Figure 2.3 for an explanation of these configurations) to guide the growth cones of the NG-108 cell line and found that they all achieved similar rates of success including turning angle and increase in growth rate (Table 2.1). This was in contrast to the results and conclusions of Mohanty et al who stated that only a forward biased line profile was capable of guiding growth cones.

The results of my experiments led to the formation of a new model of how actin behaves in an optical field. Working with my colleague Dr Michael Mazilu, a model of actin as a Rayleigh regime dielectric sphere (which was used by Ehrlicher et al before us in 2002 [114]) was expanded upon to model F-actin as a filament of these spheres. A mathematical description of a filopodia was then constructed using

information on their composition and structure from the literature. This filopodia was then modelled as a rod fixed at one end and free to rotate in the optical field of a Gaussian and a line profile laser beam. The result of these calculations suggest that filopodia experience an significant optical force orientating them towards the beam centre that is strong enough to optically trap them. This new approach strongly suggests that it is the filopodia and not the actin monomers that are the principle biological component involved in optically guided neuronal growth.

In Chapter 3 I described my technical efforts to automate the process of optically guided neuron growth using a computer controlled spatial light modulator. This chapter included background science on spatial light modulators as well as a review of their use in selected Biophotonics literature. Previously, acousto-optic deflectors had been implemented with a computer program by Sturhmann et al to automate the process of optically guided neuronal growth [135]. For this reason I included a comparison between these two devices with the conclusion that the spatial light modulator allows a greater variety of beam sculpting which places it perfectly for use in a detailed study investigating the effects of several beam shapes on optically guided neuronal growth.

I also detailed the use of LabVIEW to create a program based on the one used by Sturhmann et al to automatically track the advancing edge of a growth cone and use this information to automatically direct the laser spot to the appropriate area of the cell for growth towards a user inputted target point. This chapter included information on how the image analysis worked and a demonstration of its success in

guiding neuronal growth cones using three different beam configurations (Gaussian, line and Bessel). The publication that resulted from this work reported for the first time the use of a Bessel beam to optically guide neuronal growth cones. The Bessel beam is interesting because of its long working distance which makes it an ideal candidate for any *in vivo* experiments where depth control may be an issue. The automatic platform developed here paves the way for a comprehensive study into optically guided neuronal growth that could investigate any arbitrary beam shape as well as provide a consistent setup free from operator bias for other experiments into optically guided neuronal growth. The tracking software itself may also find use in other fields of biophotonics where precise and consistent information about a cell's shape or movements are required.

In Chapter 4 I discussed experiments I carried out into the possible biological components of optically guided neuronal growth. Whereas previous chapters had primarily dealt with the physics of optical trapping, this chapter involved the use of heat shock proteins and protein inhibitors and was divided into two sections. The first section dealt with my experiments into the use of a HSP70-GFP chimera gene as an indicator of stress in the NG-108 cell line. This section included a review of the relevant biochemistry including the heat shock family of proteins with particular emphasis on HSP70. HSP70 was chosen for experimentation because, of all the other HSP's, HSP70 is only expressed during stress. A brief introduction to green fluorescent protein was also included because of its use in these experiments. Particular attention was paid to previous use of the HSP70-GFP chimera gene in

the literature. Groups involved in laser driven gene activation have suggested the use of HSP70 as the trigger and have been experimenting on HSP70-GFP in efforts towards this [180,187]. For my experiments I used a gene that combined GFP to the promoter region of HSP70 that had previously been used to model the heat shock response of CHO cells [186]. This gene was successfully inserted into a stable cell line of NG108's that were used for experimentation. Using appropriate controls I reported that irradiation from a laser of typical power and wavelength used in similar experiments was incapable of eliciting a stress response from the HSP70 pathway. This is in agreement with previous studies which reported that the temperature rise due to an IR laser is on the order of $\sim 1-3$ °C [119, 151] which is not enough to trigger a heat shock response. The results of this experiment suggest that HSP70 is not being expressed during a typical growth experiment and is thus not involved in the mechanism. It also suggests that the reason that optical guidance of neurons is only sustainable for around 30 minutes of irradiation is not due to a heat shocking response stopping growth. This experiment is further evidence against heating as the primary mechanism for optically guided neuronal growth.

The second part of this chapter reported on my experiments into the use of protein inhibitors in optical guidance experiments. One of the plausible mechanisms for optically guided neuronal growth that has been mentioned in the literature since the beginning has been the possibility of the laser interfering with key biochemistry within the neuron [114,117]. If certain pathways were inhibited in a neuron that prevented the growth cone from growing but growth was then observed in the

presence of an optical field then this would suggest a new mechanism previously unconsidered. If, on the other hand, the mechanism of filopodia aligning in the presence of an optical field was the dominant mechanism, then we shouldn't expect to see any optical guidance of neurons being inhibited. Two inhibitors were chosen for experimentation, these were LY294002 and UO126. LY294002 is a PI-3 kinase inhibitor and UO126 is a MEK1 inhibitor. These inhibitors were chosen because they inhibit important pathways in cell growth and motility and previous literature has demonstrated that their use can adversely affect the growth of neurons [194–197, 199–201]. A range of different concentrations of these inhibitors were used and during experiments designed to guide neurons no guidance was observed. Several collapses of growth cones were also observed which is consistent with previous literature [197, 199, 201]. The presence of a laser beam did not affect this behaviour and so it can be concluded the optically guided neuronal growth needs the function of the PI-3 kinase and MEK1 pathways to operate. It must be noted that the pathways inhibited here, though important, are only two of many within the cell and so these experiments do not rule out the possibility of the biochemistry reacting to the presence of the laser completely. Though the original reason for Ehrlicher et al [114] suggesting this as a mechanism was because they reasoned that if the laser was pooling actin monomers (as they believed) then it follows that other cytosolic proteins may be getting affected as well. However, their own calculations suggested that optical forces on proteins of that order of size was minuscule and insufficient to trap them. If the laser is not trapping these proteins then perhaps

they are being altered photochemically by the laser but this would contrast with work by Neuman et al [45] and Liang et al [46] who reported on the sensitivity of cells to different laser wavelengths and reported low sensitivities for the wavelengths used in neuron growth experiments.

The work presented in this thesis contributes to the growing field of optically guided neuronal growth. The mechanism of filopodia being optically trapped represents the best explanation to date for the behaviour of growth cones to grow towards an IR laser spot. The model could be refined and improved by including other cytosolic proteins involved in filopodia in its construction as well as possibly generate one that can work with growing and shrinking filopodia and not just static filopodia. The use of beam shaping optics such as spatial light modulators as well as tracking software will almost certainly increase in this field and in Biophotonics in general. The software and hardware used in the automatic setup described in Chapter 3 represents what could be a precursor towards increasingly complex computer controlled biophotonic experiments and medical applications. With the ever increasing power and decreasing costs of these devices, their capabilities grow exponentially and powerful software that makes use of this advancing computing power will increasingly be desirable for any scientific experiment. The experiments into stress pathways and protein inhibition are also examples of the increasing interdisciplinary nature of the field of biophotonics. The result that lasers do not activate the HSP70 stress pathway was a welcome one for the neuronal growth field but it remains possible that other experiments in biophotonics (e.g. photoporation, nanoparticle injection) are

inadvertently triggering these stress pathways and the work presented here shows how such possibilities can be tested.

There is great potential to the field of medicine in this work. Spinal injuries that result in the severing of nerves are a source of severe disability in the humans and other mammals. The ultimate treatment for such an injury would be the reconnection of these nerves and, while some progress has been made using scaffolds and chemicals, the optical methods layed out in this thesis could yeild such a treatment. The use of a laser also has the added benefit of being completely sterile since no physical contact is needed. The next stages of work in this field must begin to move into more clinical environments through the use of primary cells and *in vivo* experiments for progress towards a practical medical tool to be made.

Bibliography

- [1] Einstein, A. *Physikalische Zeitschrift* **18**, 121–128 (1917).
- [2] Maiman, T. H. *Nature* **187**, 493–494 (1960).
- [3] Ashkin, A., Dziedzic, J. M., Bjorkholm, J. E., and Chu, S. *Opt. Lett.* **11**(5), 288–290 (1986).
- [4] Ashkin, A. and Dziedzic, J. M. *Science* **235**, 1517–1520 (1987).
- [5] Ashkin, A., Dziedzic, J. M., and Yamane, T. *Nature* **330**, 769–771 (1987).
- [6] Bhatt, D. H., Otto, S. J., Depoister, B., and Fetcho, J. R. *Science* **305**(5681), 254–258 (2004).
- [7] Feinerman, O., Rotem, A., and Moses, E. *Nature Physics* **4**, 967–973 (2008).
- [8] Planck, M. *Ann. Phys.* **4**, 553–563 (1901).
- [9] Einstein, A. *Ann. Phys.* **17**, 132 (1905).
- [10] Ashkin, A. *Phys. Rev. Lett.* **24**(4), 156–159 Jan (1970).
- [11] Ashkin, A. *Biophys J.* **61**, 569–582 (1992).
- [12] Jess, P. *Advanced Techniques In Raman Tweezers Microspectroscopy For Applications In Biomedicine*. PhD thesis, University of St Andrews, (2007).

-
- [13] Gordon, J. P. *Phys. Rev. A* **8**(1), 14–21 Jul (1973).
- [14] Harada, Y. and Asakura, T. *Optics Communications* **124**(5-6), 529 – 541 (1996).
- [15] Hansen, P. M., Bhatia, V. K., Harrit, N., and Oddershede, L. *Nano Lett.* **5**, 1937–1942 (2005).
- [16] Chaumet, P. C. and Nieto-Vesperinas, M. *Opt. Lett.* **25**(15), 1065–1067 (2000).
- [17] Rodrigo, P. J., Perch-Nielsen, I. R., Alonzo, C. A., and Glückstad, J. *Opt. Express* **14**(26), 13107–13112 (2006).
- [18] Gouesbet, G. and Mees, L. *J. Opt. Soc. Am. A* **16**(6), 1333–1341 (1999).
- [19] Gouesbet, G. and Gréhan, G. *Journal of Optics A: Pure and Applied Optics* **1**(6), 706 (1999).
- [20] Zemánek, P., Jonáš, A., and Liška, M. *J. Opt. Soc. Am. A* **19**(5), 1025–1034 (2002).
- [21] Han, Y., Gréhan, G., and Gouesbet, G. *Appl. Opt.* **42**(33), 6621–6629 (2003).
- [22] Neuman, K. C. and Block, S. M. *Review of Scientific Instruments* **75**(9), 2787–2809 (2004).
- [23] Kuo, S. C. *J. Microscopy Soc. Amer.* **1**, 65–74 (1995).
- [24] Berns, M. and Greulich, K., editors. *Laser Manipulation of Cells and Tissue*. Academic Press, (2007).
- [25] Guck, J., Ananthakrishnan, R., Mahmood, H., Moon, T. J., Cunningham, C. C., and Käs, J. *Biophys J.* **81**, 767–784 (2001).
- [26] Simpson, N. B., Dholakia, K., Allen, L., and Padgett, M. J. *Opt. Lett.* **22**(1), 52–54 (1997).

- [27] Paterson, L., Papagiakoumou, E., Milne, G., Garcés-Chávez, V., Tatarkova, S. A., Sibbett, W., Gunn-Moore, F. J., Bryant, P. E., Riches, A. C., and Dholakia, K. *Applied Physics Letters* **87**(12), 123901 (2005).
- [28] McDougall, C., Stevenson, D. J., Brown, C. T. A., Gunn-Moore, F., and Dholakia, K. *J. Biophot.* **2**, 736–743 (2009).
- [29] Svoboda, K., Schmidt, C., Schnapp, B., and Block, S. *Nature* **365**, 721–727 (1993).
- [30] Huxley, H. E. *Science* **164**(3886), 1356–1366 (1969).
- [31] http://news.stanford.edu/news/2003/december10/gifs/Kinesin_underscore_Proof2.jpg .
- [32] Yin, H., Wang, M. D., Svoboda, K., Landick, R., Block, S. M., and Gelles, J. *Science* **270**(5242), 1653–1657 (1995).
- [33] Abbondanzieri, E. A., Greenleaf, W. J., Shaevitz, J. W., Landick, R., and Block, S. M. *Nature* **438**, 460–465 (2005).
- [34] Wuite, G. J., Smith, S. B., Young, M., Keller, D., and Bustamante, C. *Nature* **404**, 103–106 (2000).
- [35] Bustamante, C., Bryant, Z., and Smith, S. B. *Nature* **421**, 423–427 (2003).
- [36] Matsumoto, A. and Olson, W. K. *Multiscale Model Simul.* **5**, 1227–1247 (2006).
- [37] König, K., Svaasand, L., Liu, Y., Sonek, G., Patrizio, P., Tadir, Y., Berns, M. W., and Tromberg, B. J. *Cell Mol. Biol.* **42**, 501–509 (1996).
- [38] Nascimento, J., Botvinick, E., Shi, L., Durrant, B., and Berns, M. *J. Biomed. Opt.* **11**, 044001–8 (2006).
- [39] Ashkin, A. *Proc. Nat. Acad. Sci* **94**, 4853–4860 (1997).

- [40] Wright, G., Tucker, M. J., Morton, P. C., Sweitzer-Yoder, C. L., and Smith, S. E. *Curr. Opin. Obstet. Gynecol.* **10**, 221–226 (1998).
- [41] Weber, M. J., editor. *Handbook of laser wavelengths*. CRC Press LLC, (1999).
- [42] Kielbassa, C., Roza, L., and Epe, B. *Carcinogenesis* **18**(4), 811–816 (1997).
- [43] Friedburg, E. C., Walker, G. C., Siede, W., Wood, R. D., Schultz, R. A., and Ellenberger, T. *DNA Repair and Mutagenesis*. ASM Press, (2006).
- [44] Svoboda, K. and Block, S. M. *Annual Review of Biophysics and Biomolecular Structure* **23**(1), 247–285 (1994).
- [45] Neuman, K. C., Chadd, E. H., Liou, G. F., Bergman, K., and Block, S. M. *Biophysical Journal* **77**(5), 2856 – 2863 (1999).
- [46] Liang, H., Vu, K. T., Krishnan, P., Trang, T. C., Shin, D., Kimel, S., and Berns, M. W. *Biophys J.* **70**, 1529–1533 (1996).
- [47] Liu, Y., Sonek, G. J., Berns, M. W., and Tromberg, B. J. *Biophys J.* **71**, 2158–2167 (1996).
- [48] Calmettes, P. P. and Berns, M. W. *Proceedings of the National Academy of Sciences of the United States of America* **80**(23), 7197–7199 (1983).
- [49] König, K., Liang, H., Berns, M. W., and Tromberg, B. J. *Opt. Lett.* **21**(14), 1090–1092 (1996).
- [50] <http://www.cartage.org.lb/en/themes/Sciences/Zoology/AnimalPhysiology/Anatomy/Anatomy/animalcell.jpg> .
- [51] Gray, H. *Anatomy of the Human Body 20th Edition*, chapter IX. Neurology, 6e The Sacral and Coccygeal Nerves. Lea & Febiger (1918).

- [52] Waxman, S. G. *Arch Neurol* **34**(10), 585–589 (1977).
- [53] Hodgkin, A. L. and Huxley, A. F. *J. Physiol.* **116**, 449–472 (1952).
- [54] http://upload.wikimedia.org/wikipedia/commons/b/bc/Neuron_Hand-tuned.svg .
- [55] Valiron, O., Caudron, N., and Job, D. *Cell. Mol. Life Sci.* **58**, 2069–2084 (2001).
- [56] <http://www.math.iupui.edu/mtc/Biology/tubulin.gif> .
- [57] Pollard, T. D. and Cooper, J. A. *Annual Review of Biochemistry* **55**(1), 987–1035 (1986).
- [58] Brenner, S. L. and Korn, E. D. *Journal of Biological Chemistry* **254**(20), 9982–9985 (1979).
- [59] Bentley, D. and Toroian-Raymond, A. *Nature* **323**, 712–715 (1986).
- [60] Small, J. V., Geiger, B., Kaverina, I., and Bershadsky, A. *Nat. Rev. Mol. Cell. Biol.* **3**, 957–964 (2002).
- [61] Fuchs, E. and Weber, K. *Annual Review of Biochemistry* **63**(1), 345–382 (1994).
- [62] Theriot, J. A. and Mitchison, T. J. *Nature* **352**, 126–131 (1991).
- [63] Svitkina, T. M. and Borisy, G. G. *The Journal of Cell Biology* **145**(5), 1009–1026 (1999).
- [64] Drachman, D. A. *Neurology* **64**(12), 2004–2005 (2005).
- [65] Baylor, D., Lamb, T., and Yau, K. *Journal of Physiology* **288**, 613–634 (1979).
- [66] Kater, S. B., Mattson, M. P., Cohan, C., and Connor, J. *Trends in Neurosciences* **11**(7), 315 – 321 (1988).

- [67] Neely, M. D. and Nicholls, J. G. *J. Exp. Biol.* **198**, 1433–1446 (1995).
- [68] Jun Song, H. and Ming Poo, M. *Current Opinion in Neurobiology* **9**(3), 355 – 363 (1999).
- [69] Hirase, H., Nikolenko, V., Goldberg, J. H., and Yuste, R. *J. Neurobiol.* **51**, 237–247 (2002).
- [70] Eriksson, P. S., Perfilieva, E., Björk-Eriksson, T., Alborn, A.-M., Nordborg, C., Peterson, D. A., and Gage, F. H. *Nature Medicine* **4**, 1313–1317 (1998).
- [71] Purves, D., Augustine, G. J., Fitzpatrick, D., Hall, W. C., LaMantia, A.-S., McNamara, J. O., and White, L. E. *Neuroscience 4th Edition*, chapter 22 Early Brain Development: The Initial Differentiation of Neurons and Glia. Sinauer Associates Inc. (2008).
- [72] Mitchison, T. J. and Cramer, L. P. *Cell* **84**(3), 371 – 379 (1996).
- [73] Vactor, L. A. L. . D. V. *Nature Reviews Molecular Cell Biology* **10**, 332–343 (2009).
- [74] Purves, D., Augustine, G. J., Fitzpatrick, D., Hall, W. C., LaMantia, A.-S., McNamara, J. O., and White, L. E. *Neuroscience 4th edition*, chapter 23 Construction of Neural Circuits: The Axonal Growth Cone. Sinauer Associates Inc. (2008).
- [75] Sherwood, L. *Human Physiology: From Cells to Systems 7th Edition*, chapter 7 The Peripheral Nervous System. Brooks/Cole (2010).
- [76] Tessier-Lavigne, M., Placzek, M., Lumsden, A. G. S., Dodd, J., and Jessell, T. M. *Nature* **336**, 775–778 (1988).
- [77] Ishii, N., Wadsworth, W. G., Stern, B. D., Culotti, J. G., and Hedgecock, E. M. *Neuron* **9**, 873–881 (1992).

- [78] KEYNES, R. and COOK, G. M. W. *Cell* **83**, 161–169 (1995).
- [79] Tessier-Lavigne, M. and Goodman, C. S. *Science* **274**(5290), 1123–1133 (1996).
- [80] Dent, E. W. and Gertler, F. B. *Neuron* **40**, 209–227 (2003).
- [81] Dickson, B. J. *Science* **298**(5600), 1959–1964 (2002).
- [82] Song, H. and Poo, M. *Nat. Cell. Biol.* **3**, E81–E88 (2001).
- [83] Schwamborn, J. C., Fiore, R., Bagnard, D., Kappler, J., Kaltschmidt, C., and Püschel, A. W. *Journal of Biological Chemistry* **279**(30), 30923–30926 (2004).
- [84] Flanagan, J. G. and Vanderhaeghen, P. *Annual Review of Neuroscience* **21**(1), 309–345 (1998).
- [85] Ranscht, B. *International Journal of Developmental Neuroscience* **18**(7), 643 – 651 (2000).
- [86] Farmer, W. T., Altick, A. L., Nural, H. F., Dugan, J. P., Kidd, T., Charron, F., and Mastick, G. S. *Development* **135**(22), 3643–3653 (2008).
- [87] Serafini, T., Kennedy, T. E., Gaiko, M. J., Mirzayan, C., Jessell, T. M., and Tessier-Lavigne, M. *Cell* **78**(3), 409 – 424 (1994).
- [88] de la Torre, J. R., Häpker, V. H., Li Ming, G., Ming Poo, M., Tessier-Lavigne, M., Hemmati-Brivanlou, A., and Holt, C. E. *Neuron* **19**(6), 1211 – 1224 (1997).
- [89] Hong, K., Hinck, L., Nishiyama, M., Ming Poo, M., Tessier-Lavigne, M., and Stein, E. *Cell* **97**(7), 927 – 941 (1999).
- [90] Fiore, R. and Puschel, A. *Front. Biosci.* **8**, 484–499 (2003).
- [91] Luo, Y., Raible, D., and Raper, J. A. *Cell* **75**, 217–227 (1993).

- [92] Chedotal, A., Rio, J. A. D., Ruiz, M., He, Z., Borrell, V., Castro, F. D., Ezan, F., Goodman, C. S., Tessier-Lavigne, M., and Sotelo, C. *Development* **125**, 4313–4323 (1998).
- [93] Taniguchi, M., Yuasa, S., Fujisawa, H., Naruse, I., Saga, S., Mahina, M., and Yagi, T. *Neuron* **19**, 519–530 (1997).
- [94] Kitsukawa, T., Shimizu, M., Sanbo, M., Hirata, T., Taniguchi, M., Bekku, Y., Yagi, T., and Fujisawa, H. *Neuron* **19**(5), 995 – 1005 (1997).
- [95] Schwarting, G. A., Kostek, C., Ahmad, N., Dibble, C., Pays, L., and PÄEschel, A. W. *J. Neurosci.* **20**, 7691–7697 (2000).
- [96] Wong, J. T., Wong, S. T., and O’Connor, T. P. *Nat. Neurosci.* **2**, 798–803 (1999).
- [97] Tamagnone, L., Artigiani, S., Chen, H., He, Z., li Ming, G., jun Song, H., Chedotal, A., Winberg, M. L., Goodman, C. S., ming Poo, M., Tessier-Lavigne, M., and Comoglio, P. M. *Cell* **99**, 71–80 (1999).
- [98] Uemura, T. *Cell* **93**(7), 1095 – 1098 (1998).
- [99] Miner, J. H. and Yurchenco, P. D. *Annual Review of Cell and Developmental Biology* **20**(1), 255–284 (2004).
- [100] Edgar, D., Timpl, R., and Thoenen, H. *EMBO J.* **3**, 1463–1468 (1984).
- [101] Dertinger, S. K. W., Jiang, X., Li, Z., Murthy, V. N., and Whitesides, G. M. *Proceedings of the National Academy of Sciences of the United States of America* **99**(20), 12542–12547 (2002).
- [102] Welle, A., Horn, S., Schimmelpfeng, J., and Kalka, D. *Journal of Neuroscience Methods* **142**(2), 243 – 250 (2005).

- [103] Smalheiser, N. R., Crain, S. M., and Reid, L. M. *Developmental Brain Research* **12**(1), 136 – 140 (1984).
- [104] Domogatskaya, A., Rodin, S., Boutaud, A., and Tryggvason, K. *Stem Cells* **26**, 2800–2809 (2008).
- [105] Shekarabi, M., Moore, S. W., Tritsch, N. X., Morris, S. J., Bouchard, J.-F., and Kennedy, T. E. *J. Neurosci.* **25**, 3132–3141 (2005).
- [106] Ingvar, S. *Proceedings of the Society for Experimental Biology and Medicine* **17**, 198–199 (1920).
- [107] McCaig, C. D., Rajnicek, A. M., Song, B., and Zhao, M. *Physiol. Rev.* **85**(3), 943–978 (2005).
- [108] McCaig, C. D., Rajnicek, A. M., Song, B., and Zhao, M. *Trends in Neurosciences* **25**(7), 354 – 359 (2002).
- [109] Erskine, L., Stewart, R., and McCaig, C. D. *J. Neurobiol.* **26**, 523–536 (1995).
- [110] Rajnicek, A. M., Robinson, K. R., and McCaig, C. D. *Developmental Biology* **203**(2), 412 – 423 (1998).
- [111] McCaig, C. D. *The Journal of Physiology* **375**(1), 55–69 (1986).
- [112] Moore, M. J., Friedman, J. A., Lewellyn, E. B., Mantila, S. M., Krych, A. J., Ameenuddin, S., Knight, A. M., Lu, L., Currier, B. L., Spinner, R. J., Marsh, R. W., Windebank, A. J., and Yaszemski, M. J. *Biomaterials* **27**(3), 419 – 429 (2006).
- [113] Albrecht-Buehler, G. *J. Cell. Biol.* **114**, 493–502 (1991).
- [114] Ehrlicher, A., Betz, T., Stuhmann, B., Koch, D., Milner, V., Raizen, M. G., and Kas, J. *Proc. Nat. Acad. Sci.* **99**, 16024–16028 (2002).

- [115] Carnegie, D. J., Stevenson, D. J., Mazilu, M., Gunn-Moore, F., and Dholakia, K. *Opt. Express* **16**(14), 10507–10517 (2008).
- [116] Mohanty, S. K., Sharma, M., Panicker, M. M., and Gupta, P. K. *Opt. Lett.* **30**(19), 2596–2598 (2005).
- [117] Stevenson, D. J., Lake, T. K., Agate, B., Garcés-Chávez, V., Dholakia, K., and Gunn-Moore, F. *Opt. Express* **14**(21), 9786–9793 (2006).
- [118] Mao, H., Arias-Gonzalez, J. R., Smith, S. B., Tinoco, I., and Bustamante, C. *Biophys J.* **89**, 1308–1316 (2005).
- [119] Liu, Y., Cheng, D. K., Sonek, G. J., Berns, M. W., Chapman, C. F., and Tromberg, B. J. *Biophys J.* **68**, 2137–2144 (1995).
- [120] Dasgupta, R., Mohanty, S. K., and Gupta, P. K. *Biotechnology Letters* **25**, 1625–1628 (2003).
- [121] Stevenson, D. J., Carnegie, D. J., and Dholakia, K. *Microscopy Anal.* **22**, 9–11 (2008).
- [122] Howard, M. K., Burke, L. C., Mailhos, C., Gilbert, A. P. C. S., Lawson, W. D., Collins, M. K., Thomas, N. S., and Latchman, D. S. *J. Neurochem.* **60**, 1783–1791 (1993).
- [123] Yu, T., Cheong, F.-C., and Sow, C.-H. *Nanotechnology* **15**, 1732–1736 (2004).
- [124] Ehrlicher, A., Betz, T., Stuhmann, B., Gögler, M., Koch, D., Franze, K., Lu, Y., and Käs, J. *Methods Cell Biol.* **83**, 495–520 (2007).
- [125] Huglin, M. B. *Light Scattering from Polymer Solutions*, 204. Academic, London (1972).

- [126] Kratochvil, P. *Classical Light Scattering from Polymer Solutions*, 79–83. Elsevier, Amsterdam (1987).
- [127] Wagner, O., Zinke, J., Dancker, P., Grill, W., and Bereiter-Hahn, J. *Biophys J.* **76**, 2784–2796 (1999).
- [128] Drezek, R., Dunn, A., and Richards-Kortum, R. *Appl. Opt.* **38**(16), 3651–3661 (1999).
- [129] Rohrbach, A. and Stelzer, E. H. K. *J. Opt. Soc. Am. A* **18**(4), 839–853 (2001).
- [130] Popov, S. and Poo, M. M. *J. Neurosci.* **12**(1), 77–85 (1992).
- [131] Draine, B. T. *Astrophys. J.* **333**, 848–872 (1988).
- [132] Mogilner, A. and Rubinstein, B. *Biophys. J.* **89**, 782–795 (2005).
- [133] Lan, Y. and Papoian, G. A. *Biophys. J.* **94**, 3839–3852 (2008).
- [134] Cong, Y., Topf, M., Sali, A., Matsudaira, P., Dougherty, M., Chiu, W., and Schmid, M. F. *Journal of Molecular Biology* **375**(2), 331 – 336 (2008).
- [135] Stuhrmann, B., Gögler, M., Betz, T., Ehrlicher, A., Koch, D., and Käs, J. *Review of Scientific Instruments* **76**(3), 035105 (2005).
- [136] Carnegie, D. J., Čižmár, T., Baumgartl, J., Gunn-Moore, F. J., and Dholakia, K. *J. Biophotonics* **2**, 682–692 (2009).
- [137] Reicherter, M., Haist, T., Wagemann, E. U., and Tiziani, H. J. *Opt. Lett.* **24**(9), 608–610 (1999).
- [138] Curtis, J. E., Koss, B. A., and Grier, D. G. *Optics Communications* **207**(1-6), 169 – 175 (2002).
- [139] Hecht, E. *Optics*. Addison Wesley, (2002).

- [140] Wilson, J. and Hawkes, J. *Optoelectronics: An introduction*, chapter Diplsay devices, 158–163. Prentice Hall (1998).
- [141] Wulff, K. D., Cole, D. G., Clark, R. L., DiLeonardo, R., Leach, J., Cooper, J., Gibson, G., and Padgett, M. J. *Opt. Express* **14**(9), 4169–4174 (2006).
- [142] Vossen, D. L. J., van der Horst, A., Dogterom, M., and van Blaaderen, A. *Review of Scientific Instruments* **75**(9), 2960–2970 (2004).
- [143] http://www.holoeye.com/pics/Phase_modulator_HEO1080P_big.jpg.
- [144] Prewitt, J. M. S. *Picture Processing and Psychopictorics*, chapter Object Enhancement and Extraction, 75–149. Academic Press (1970).
- [145] Tsampoula, X., Gárcés-Chávez, V., Comrie, M., Stevenson, D. J., Agate, B., Brown, C. T. A., Gunn-Moore, F., and Dholakia, K. *Applied Physics Letters* **91**(5), 053902 (2007).
- [146] Durnin, J., Miceli, J. J., and Eberly, J. H. *Phys. Rev. Lett.* **58**(15), 1499–1501 Apr (1987).
- [147] Bracewell, R. *The Fourier Transform and Its Applications*, 106–110. McGraw-Hill (1999).
- [148] Cormack, A. M. *Acta Crystallographica* **10**(5), 354–358 May (1957).
- [149] Bracewell, R. *The Fourier Transform and Its Applications*, 105–107. McGraw-Hill (1999).
- [150] Bracewell, R. *The Fourier Transform and Its Applications*, 336–337. McGraw-Hill (1999).

- [151] Stevenson, D., Agate, B., Tsampoula, X., Fischer, P., Brown, C. T. A., Sibbett, W., Riches, A., Gunn-Moore, F., and Dholakia, K. *Opt. Express* **14**(16), 7125–7133 (2006).
- [152] Lindquist, S. *Annual Review of Biochemistry* **55**(1), 1151–1191 (1986).
- [153] Parsell, D. A. and Lindquist, S. *Annu. Rev. Genet.* **27**, 437–496 (1993).
- [154] Reszka, A. A., Seger, R., Diltz, C. D., Krebs, E. G., and Fischer, E. H. *Proceedings of the National Academy of Sciences of the United States of America* **92**(19), 8881–8885 (1995).
- [155] Paliga, A. J., Natale, D. R., and Watson, A. J. *Biol. Cell.* **97**, 629–640 (2005).
- [156] Polleux, F., Whitford, K. L., Dijkhuizen, P. A., Vitalis, T., and Ghosh, A. *Development* **129**(13), 3147–3160 (2002).
- [157] Maio, A. D. *Shock* **11**, 1–12 (1999).
- [158] Heim, R., Cubitt, A. B., and Tsien, R. Y. *Nature* **373**, 663–664 (1995).
- [159] Mathew, M., Amat-Roldan, I., Andr s, R., Cormack, I. G., Artigas, D., Soriano, E., and Loza-Alvarez, P. *Cytotechnology* **58**, 103–111 (2008).
- [160] Skowyra, D., Georgopoulos, C., and Zyllicz, M. *Cell* **62**(5), 939 – 944 (1990).
- [161] Ziemienowicz, A., Skowyra, D., Zeilstra-Ryalls, J., Fayet, O., Georgopoulos, C., and Zyllicz, M. *Journal of Biological Chemistry* **268**(34), 25425–25431 (1993).
- [162] Freeman, B. and Morimoto, R. *EMBO J.* **15**, 2969–2979 (1996).
- [163] Lindquist, S. and Craig, E. A. *Annual Review of Genetics* **22**(1), 631–677 (1988).
- [164] Wu, B., Hunt, C., and Morimoto, R. *Mol. Cell. Biol.* **5**(2), 330–341 (1985).

- [165] Sarge, K., Murphy, S., and Morimoto, R. *Mol. Cell. Biol.* **13**, 1392–1407 (1993).
- [166] Morimoto, R. I. *Science* **259**, 1409–1410 (1993).
- [167] Morimoto, R. I. *Genes and Dev.* **12**, 3788–3796 (1998).
- [168] Pockley, A. G. *The Lancet* **362**, 469–476 (2003).
- [169] Shimomura, O., Johnson, F. H., and Saiga, Y. *J. Cell. Comp. Physiol.* **59**, 223–239 (1962).
- [170] Morin, J. G. and Hastings, J. W. *J. Cell. Physiol.* **77**, 313–318 (1971).
- [171] Morise, H., Shimomura, O., Johnson, F. H., and Winant, J. *Biochem.* **13**, 2656–2662 (1974).
- [172] Inouye, S. and Tsuji, F. I. *FEBS Letters* **341**(2-3), 277 – 280 (1994).
- [173] Chalfie, M., Tu, Y., Euskirchen, G., Ward, W., and Prasher, D. *Science* **263**(5148), 802–805 (1994).
- [174] Ormö, M., Cubitt, A. B., Kallio, K., Gross, L. A., Tsien, R. Y., and Remington, S. J. *Science* **273**(5280), 1392–1395 (1996).
- [175] Yang, F., Moss, L. G., and Phillips, G. N. *Nat. Biotech.* **14**, 1246–1251 (1996).
- [176] Yang, T., Cheng, L., and Kain, S. R. *Nucleic Acids Res.* **24**, 4592–4593 (1996).
- [177] Zolotukhin, S., Potter, M., Hauswirth, W. W., Guy, J., and Muzyczka, N. *J. Virol.* **70**, 4646–4654 (1996).
- [178] Tsien, R. Y. *Annual Review of Biochemistry* **67**(1), 509–544 (1998).
- [179] Sekar, R. B. and Periasamy, A. *J. Cell. Biol.* **160**, 629–633 (2003).

- [180] Halloran, M. C., Sato-Maeda, M., Warren, J. T., Su, F., Lele, Z., Krone, P. H., Kuwada, J. Y., and Shoji, W. *Development* **127**, 1953–1960 (2000).
- [181] Strobbe, L. J., Nieweg, O. E., and Kroon, B. B. *European Journal of Surgical Oncology* **23**, 435–438 (1997).
- [182] Zelickson, B. D. and Roenigk, R. K. *Surgical Oncology* **65**, 1307–1311 (2006).
- [183] Vekris, A., Maurange, C., Moonen, C., Mazurier, F., Verneuil, H. D., Canioni, P., and Voisin, P. *J. Gene. Med.* **2**, 89–96 (2000).
- [184] Wippersteg, V., Kapp, K., Kunz, W., Jackstadt, W., Zahner, H., and Grevelding, C. G. *Molecular and Biochemical Parasitology* **120**(1), 141 – 150 (2002).
- [185] Zeng, X.-C., Bhasin, S., Wu, X., Lee, J.-G., Maffi, S., Nichols, C. J., Lee, K. J., Taylor, J. P., Greene, L. E., and Eisenberg, E. *J. Cell. Sci.* **117**(21), 4991–5000 (2004).
- [186] Lipan, O., Navenot, J.-M., Wang, Z., Huang, L., and Peiper, S. C. *PLoS Comput Biol* **3**(10), 1859–1870 10 (2007).
- [187] Ramos, D. M., Kamal, F., Wimmer, E. A., Cartwright, A. N., and Monteiro, A. *Dev. Biol.* **6** (2006).
- [188] Pearson, G., Robinson, F., Beers Gibson, T., Xu, B.-e., Karandikar, M., Berman, K., and Cobb, M. H. *Endocr Rev* **22**(2), 153–183 (2001).
- [189] Fukunaga, K. and Miyamoto, E. *Mol. Neurobiol.* **16**, 79–95 (1998).
- [190] Sweatt, J. D. *J. Neurochem.* **76**, 1–10 (2001).
- [191] Hammarlund, M., Nix, P., Hauth, L., Jorgensen, E. M., and Bastiani, M. *Science* **323**(5915), 802–806 (2009).

- [192] Forcet, C., Stein, E., Pays, L., Corset, V., Llambi, F., Tessier-Lavigne, M., and Mehlen, P. *Nature* **417**, 443–447 (2002).
- [193] Newton, R., Cambridge, L., Hart, L. A., Stevens, D. A., Lindsay, M. A., and Barnes, P. J. *Br J Pharmacol.* **130**, 1353–1361 (2000).
- [194] Pang, L., Sawada, T., Decker, S. J., and Saltiel, A. R. *Journal of Biological Chemistry* **270**(23), 13585–13588 (1995).
- [195] li Ming, G., Wong, S. T., Henley, J., bing Yuan, X., jun Song, H., Spitzer, N. C., and ming Poo, M. *Nature* **417**, 411–418 (2002).
- [196] Sjögren, B., Wiklund, P., and Ekström, P. A. R. *Neuroscience* **100**(2), 407 – 416 (2000).
- [197] Atwal, J. K., Singh, K. K., Tessier-Lavigne, M., Miller, F. D., and Kaplan, D. R. *J. Neurosci.* **23**(20), 7602–7609 (2003).
- [198] Freeman, R. S., Burch, R. L., Crowder, R. J., Lomb, D. J., Schoell, M. C., Straub, J. A., and Xie, L. In *NGF and Related Molecules in Health and Disease*, Aloe, L. and Calza, L., editors, volume 146 of *Progress in Brain Research*, 111 – 126. Elsevier (2004).
- [199] Laurino, L., Wang, X. X., de la Houssaye, B. A., Sosa, L., Dupraz, S., Caceres, A., Pfenninger, K. H., and Quiroga, S. *J Cell Sci* **118**(16), 3653–3662 (2005).
- [200] Jimenez, C., Portela, R. A., Mellado, M., Rodriguez-Frade, J. M., Collard, J., Serano, A., Martínez-A, C., Avila, J., and Carrera, A. C. *J. Cell. Biol.* **151**, 249–261 (2000).
- [201] Chadborn, N. H., Ahmed, A. I., Holt, M. R., Prinjha, R., Dunn, G. A., Jones, G. E., and Eickholt, B. J. *J. Cell. Sci.* **119**, 951–957 (2005).

- [202] Sigma-Aldrich. *U0126 ethanolate Product Information* (Accessed 2010).
- [203] Calbiochem. *LY294002 Product Data Sheet* (Accessed 2010).
- [204] Vlahos, C. J., Matter, W. F., Hui, K. Y., and Brown, R. F. *J. Biol. Chem.* **18**, 5241–5248 (1994).
- [205] Kovacsovics, T., Bachelot, C., Toker, A., Vlahos, C., Duckworth, B., Cantley, L., and Hartwig, J. *Journal of Biological Chemistry* **270**(19), 11358–11366 (1995).
- [206] Bar, J., Lukaschuk, N., Zalcnstein, A., Wilder, S., Seger, R., and Oren, M. *Cell Death Differ.* **12**, 1578–1587 (2005).
- [207] Portnoy, J., Curran-Everett, D., and Mason, R. J. *Am. J. Respir. Cell Mol. Biol.* **30**(6), 901–907 (2004).
- [208] Lu, B. *U.S. Army Medical Research and Materials Annual Report* (2005).
- [209] Favata, M. F., Horiuchi, K. Y., Manos, E. J., Daulerio, A. J., Stradley, D. A., Feeser, W. S., Van Dyk, D. E., Pitts, W. J., Earl, R. A., Hobbs, F., Copeland, R. A., Magolda, R. L., Scherle, P. A., and Trzaskos, J. M. *Journal of Biological Chemistry* **273**(29), 18623–18632 (1998).
- [210] Duncia, J. V., Santella, J. B., Higley, C. A., Pitts, W. J., Wityak, J., Fietze, W. E., Rankin, F. W., Sun, J.-H., Earl, R. A., Tabaka, A. C., Teleha, C. A., Blom, K. F., Favata, M. F., Manos, E. J., Daulerio, A. J., Stradley, D. A., Horiuchi, K., Copeland, R. A., Scherle, P. A., Trzaskos, J. M., Magolda, R. L., Trainor, G. L., Wexler, R. R., Hobbs, F. W., and Olson, R. E. *Bioorganic & Medicinal Chemistry Letters* **8**(20), 2839 – 2844 (1998).
- [211] DeSilva, D. R., Jones, E. A., Favata, M. F., Jaffee, B. D., Magolda, R. L., Trzaskos, J. M., and Scherle, P. A. *J. Immunol.* **160**, 4175–4181 (1998).

- [212] Zhang, J., Fu, M., Myles, D., Zhu, X., Du, J., Cao, X., and Chen, Y. E. *FEBS Letters* **521**(1-3), 180 – 184 (2002).
- [213] Centre, F. C. C. *Defense Technical Information Center* (2004).
- [214] Bullard, A. J., Govewalla, P., and Yellon, D. M. *Basic Research in Cardiology* **100**, 397–403 (2005). 10.1007/s00395-005-0537-4.
- [215] Seguin, C. A., Pilliar, R. M., Madri, J. A., and Kandel, R. A. *Spine* **33**, 356–365 (2008).
- [216] li Ming, G., jun Song, H., Berninger, B., Holt, C. E., Tessier-Lavigne, M., and ming Poo, M. *Neuron* **19**, 1225–1235 (1997).
- [217] Seo, J. Y., Kim, J. S., JH, J. H. G., Kang, T. C., Suh, J. G., Kim, E. G. K. J. I., Kim, J., Lee, J. Y., and Park, J. B. *Neuroreport* **14**, 1277–1281 (2003).

Appendix

5.1 Appendix 1: Data in Table 2.1

Included here is the full set of data used to construct Table 2.1 in chapter 2.

| Beam configuration | Cell reference number | Rate of growth during guidance($\mu\text{m}/\text{h}$) | Change in initial direction due to guidance($^{\circ}$) |
|--------------------|-----------------------|--|---|
| Forward bias | 4A | 41 | 23 |
| | 5A | 36 | 29 |
| | 5F | 27 | 5 |
| | 6B | 56 | 52 |
| | 9B | 123 | 76 |
| | 11F | 86 | 15 |
| | 12C | 90 | 6 |
| | 12G | 63 | 5 |
| Reverse Bias | 19A | 100 | 21 |
| | 19J | 122 | 5 |
| | 20A | 46 | 5 |
| | 20L | 66 | 38 |
| | 10B | 66 | 16 |
| | 14J | 72 | 19 |
| | 14B | 52 | 31 |
| | 21G | 100 | 16 |
| Symmetric control | 28A | 100 | 25 |
| | 26A | 135 | 33 |
| | 26C | 53 | 42 |
| | 24A | 133 | 30 |
| | 25A | 135 | 40 |
| | 15A | 85 | 20 |
| | 22B | 136 | 56 |

The errors in Table 2.1 are standard errors of the mean (SEM) calculated by:

$$SEM = \frac{SD}{\sqrt{n}}$$

Where n is the sample size and SD is standard deviation given by:

$$SD = \sqrt{\frac{1}{n} \sum_{i=1}^n (x_i - \bar{x})^2}$$

Where x_i is the i^{th} element and \bar{x} is the mean of element x .

5.2 Appendix 2: Mathematica code

The following text is the raw Mathematica 5.2 (Wolfram) code that was used to model the behaviour of a filopodia in an optical field which was discussed in Chapter 2.

One period of the filament

```

ract = 3;
hact = 37./7;
act = \[Pi]/7.;
dact = 2.7;
act0 = 0;
pos = Drop[
Flatten[Table[{{i hact, dact Cos[act0 + i act],
dact Sin[act0 + i act]}, {(i + 1/2) hact,
dact Cos[act0 + i act + \[Pi]],
dact Sin[act0 + i act + \[Pi]]}}, {i, 0, 14}], 1], 2];
Dimensions[pos]
Show[Graphics3D[

```

```
Table[TranslateShape[Sphere[ract, 18, 18], pos[[i]], {i,
Length[pos]}]]];
```

A bundle of 25 filaments

```
ract = 3;
hact = 37./7;
act = \[Pi]/7.;
dact = 2.7;
act0 = 0;
pos = Flatten[
Table[{{i hact, xp + dact Cos[act0 + i act],
yp + dact Sin[act0 + i act]}, {(i + 1/2) hact,
xp + dact Cos[act0 + i act + \[Pi]],
yp + dact Sin[act0 + i act + \[Pi]]}}, {i, 0, 378,
1}, {xp, -20, 20, 10}, {yp, -20, 20, 10}}, 3];
Show[Graphics3D[
Table[Translateshape[Sphere[ract,18,18], pos[[i]],
{i, Length[pos]}]]];
```

Torque as a function of the angle of the bundle of filaments (symmetric line trap)

```
<< Graphics'MultipleListPlot'
<< Graphics'PlotField'
<< Graphics'Colors'
<< Graphics'Legend'
<< Calculus'VectorAnalysis'
SetCoordinates[Cartesian[x, y, z]];
n0 = 1.33;
n1 = 1.59;
w0x = 45.*^-6/2;
w0y = 0.5*^-6;
mu0 = 4 \[Pi] 1*^-7;
epsilon0 = 8.854187817*^-12;
lam = 1064*^-9;
```

```

k0 = 2 \[Pi]/lam;
p0 = 0.07;
zrx = n0 k0 w0x^2/2;
zry = n0 k0 w0y^2/2;
amp = Sqrt[4*p0/\[Pi]/w0x/w0y*Sqrt[mu0/epsilon0]/n0];
u0 := amp*Exp[-I*n0*k0*(z)]*Sqrt[(I*zrx/(z + I*zrx))]
Sqrt[(I*zry/(z + I*zry))]*
Exp[-I*n0*k0*((x)^2/2/(z + I*zrx) + (y)^2/2/(z + I*zry))];
uv = {0, u0, 0};
e0 = 1/n0^2/k0^2*Grad[Div[uv]] + uv;
h0 = I/k0 Curl[uv] Sqrt[epsilon0/mu0];
e0 = {0, u0, 0};
h0 = n0 {-u0, 0, 0} Sqrt[epsilon0/mu0];
poi = 1/2 Re[Cross[e0, Conjugate[h0]]] // Chop;
aa0 = 4 \[Pi] rad^3 (n1^2 - n0^2)/(n1^2 + 2 n0^2);
aa = aa0/(1 + 2/3 I n0^3 k0^3 aa0/(4 \[Pi]));
cscat = n0^4 k0^4/6/\[Pi]*Abs[aa]^2;
cabs = n0 k0 Im[aa0];
fsc = (cscat + cabs) n0 Sqrt[epsilon0 mu0] poi;
fgr = 1/4 epsilon0 n0^2 Re[
aa] 2 Re[{e0.Conjugate[D[e0, x]], e0.Conjugate[D[e0, y]],
e0.Conjugate[D[e0, z]]}];
fray = epsilon0 n0^2/2 Re[
aa {e0.Conjugate[D[e0, x]], e0.Conjugate[D[e0, y]],
e0.Conjugate[D[e0, z]]}];
ract = 3;
hact = 37./7;
act = \[Pi]/7.;
dact = 2.7;
act0 = 0;
pos = Flatten[
Table[{i hact, xp + dact Cos[act0 + i act],
yp + dact Sin[act0 + i act]}, {(i + 1/2) hact,
xp + dact Cos[act0 + i act + \[Pi]],
yp + dact Sin[act0 + i act + \[Pi]]}], {i, 0, 378,
1}, {xp, -20, 20, 10}, {yp, -20, 20, 10}], 3];

```

```

Length[pos]
ffr[xx0_, yy0_, zz0_, \[Alpha]_] :=
Sum[(Re[(fray)] /. {x -> xx0 + 1*^-9 xx, y -> yy0 + 1*^-9 yy,
z -> zz0 + 1*^-9 pos[[i, 3]], rad -> 1*^-9 ract}) /. {xx ->
Cos\[Alpha] pos[[i, 1]] - Sin\[Alpha] pos[[i, 2]],
yy -> Cos\[Alpha] pos[[i, 2]] + Sin\[Alpha] pos[[i, 1]]}, {i,
Length[pos]}}
tz[xx0_, yy0_, zz0_, \[Alpha]_] :=
Sum[(Cross[{x - xx0, y - yy0, 0}, Re[(fray)]][[3]] /. {x ->
xx0 + 1*^-9 xx, y -> yy0 + 1*^-9 yy,
z -> zz0 + 1*^-9 pos[[i, 3]], rad -> 1*^-9 ract}) /. {
xx -> Cos\[Alpha] pos[[i, 1]] - Sin\[Alpha] pos[[i, 2]],
yy -> Cos\[Alpha] pos[[i, 2]] + Sin\[Alpha] pos[[i, 1]]}, {i,
Length[pos]}}]
ffr[1*^-6, 0, 0, 0]
ffr[1*^-6, 0, 0, \[Pi]/2]
ffg[xx0_, yy0_, zz0_, \[Alpha]_] :=
Sum[(Re[(fsc + fgr)] /. {x -> xx0 + 1*^-9 xx,
y -> yy0 + 1*^-9 yy, z -> zz0 + 1*^-9 pos[[i, 3]],
rad -> 1*^-9 ract}) /. {xx ->
Cos\[Alpha] pos[[i, 1]] - Sin\[Alpha] pos[[i, 2]],
yy -> Cos\[Alpha] pos[[i, 2]] + Sin\[Alpha] pos[[i, 1]]}, {i,
Length[pos]}}]
ffg[1*^-6, 0, 0, 0]
ffg[1*^-6, 0, 0, \[Pi]/2]
Plot[1*^-21 tz[w0x, w0y, 0, \[Alpha] Degree], {\[Alpha], 0, 360}, Frame -> True];

```

Torque as a function of the angle of the bundle of filaments (gaussian beam)

```

<< Graphics'MultipleListPlot'
<< Graphics'PlotField'
<< Graphics'Colors'
<< Graphics'Legend'
<< Calculus'VectorAnalysis'
SetCoordinates[Cartesian[x, y, z]];

```



```

e0.Conjugate[D[e0, z]]];

ract = 3;

hact = 37./7;

act = \[Pi]/7.;

dact = 2.7;

act0 = 0;

pos = Flatten[
Table[{{i hact, xp + dact Cos[act0 + i act],
yp + dact Sin[act0 + i act]}, {(i + 1/2) hact,
xp + dact Cos[act0 + i act + \[Pi]],
yp + dact Sin[act0 + i act + \[Pi]]}}, {i, 0, 378,
1}, {xp, -20, 20, 10}, {yp, -20, 20, 10}], 3];

Length[pos]

ffr[xx0_, yy0_, zz0_, \[Alpha]_] :=
Sum[(Re[fray]) /. {x -> xx0 + 1*^-9 xx, y -> yy0 + 1*^-9 yy,
z -> zz0 + 1*^-9 pos[[i, 3]], rad -> 1*^-9 ract}) /. {xx ->
Cos\[Alpha] pos[[i, 1]] - Sin\[Alpha] pos[[i, 2]],
yy -> Cos\[Alpha] pos[[i, 2]] + Sin\[Alpha] pos[[i, 1]]}, {i,
Length[pos]}]

tz[xx0_, yy0_, zz0_, \[Alpha]_] :=
Sum[(Cross[{x - xx0, y - yy0, 0}, Re[fray]]][[3]] /. {x ->
xx0 + 1*^-9 xx, y -> yy0 + 1*^-9 yy,
z -> zz0 + 1*^-9 pos[[i, 3]], rad -> 1*^-9 ract}) /. {
xx -> Cos\[Alpha] pos[[i, 1]] - Sin\[Alpha] pos[[i, 2]],
yy -> Cos\[Alpha] pos[[i, 2]] + Sin\[Alpha] pos[[i, 1]]}, {i,
Length[pos]}]

ffr[1*^-6, 0, 0, 0]

ffr[1*^-6, 0, 0, \[Pi]/2]

ffg[xx0_, yy0_, zz0_, \[Alpha]_] :=
Sum[(Re[fsc + fgr]) /. {x -> xx0 + 1*^-9 xx,
y -> yy0 + 1*^-9 yy, z -> zz0 + 1*^-9 pos[[i, 3]],
rad -> 1*^-9 ract}) /. {xx ->
Cos\[Alpha] pos[[i, 1]] - Sin\[Alpha] pos[[i, 2]],
yy -> Cos\[Alpha] pos[[i, 2]] + Sin\[Alpha] pos[[i, 1]]}, {i,
Length[pos]}]

ffg[1*^-6, 0, 0, 0]

```

```
ffg[1*^-6, 0, 0, \[Pi]/2]
Plot[1*^21 tz[w0x, w0y, 0, \[Alpha] Degree], {\[Alpha], 0, 360}, Frame -> True];
```

Filopodia equilibrium position for line trap

```
<< Graphics'MultipleListPlot'
<< Graphics'PlotField'
<< Graphics'Colors'
<< Graphics'Legend'
<< Calculus'VectorAnalysis'
SetCoordinates[Cartesian[x, y, z]];
n0 = 1.33;
n1 = 1.59;
w0x = 45*^-6/2;
w0y = 0.5*^-6;
mu0 = 4 \[Pi] 1*^-7;
epsilon0 = 8.854187817*^-12;
lam = 1064*^-9;
k0 = 2 \[Pi]/lam;
p0 = 0.07;
zrx = n0 k0 w0x^2/2;
zry = n0 k0 w0y^2/2;
amp = Sqrt[4*p0/\[Pi]/w0x/w0y*Sqrt[mu0/epsilon0]/n0];
u0 := amp*Exp[-I*n0*k0*(z)]*Sqrt[(I*zrx/(z + I*zrx))]
Sqrt[(I*zry/(z + I*zry))*
Exp[-I*n0*k0*((x)^2/2/(z + I*zrx) + (y)^2/2/(z + I*zry))];
uv = {0, u0, 0};
e0 = 1/n0^2/k0^2*Grad[Div[uv]] + uv;
h0 = I/k0 Curl[uv] Sqrt[epsilon0/mu0];
e0 = {0, u0, 0};
h0 = n0 {-u0, 0, 0} Sqrt[epsilon0/mu0];
poi = 1/2 Re[Cross[e0, Conjugate[h0]]] // Chop;
aa0 = 4 \[Pi] rad^3 (n1^2 - n0^2)/(n1^2 + 2 n0^2);
aa = aa0/(1 + 2/3 I n0^3 k0^3 aa0/(4 \[Pi]));
cscat = n0^4 k0^4/6/\[Pi]*Abs[aa]^2;
cabs = n0 k0 Im[aa0];
```

```

fsc = (cscat + cabs) n0 Sqrt[epsilon0 mu0] poi;
fgr = 1/4 epsilon0 n0^2 Re[
aa] 2 Re[{e0.Conjugate[D[e0, x]], e0.Conjugate[D[e0, y]],
e0.Conjugate[D[e0, z]]}];
fray = epsilon0 n0^2/2 Re[
aa {e0.Conjugate[D[e0, x]], e0.Conjugate[D[e0, y]],
e0.Conjugate[D[e0, z]]}];
ract = 3;
hact = 37./7;
act = \[Pi]/7.;
dact = 2.7;
act0 = 0;
pos = Flatten[
Table[{i hact, xp + dact Cos[act0 + i act],
yp + dact Sin[act0 + i act], {(i + 1/2) hact,
xp + dact Cos[act0 + i act + \[Pi]],
yp + dact Sin[act0 + i act + \[Pi]]}}, {i, 0, 378,
1}, {xp, -20, 20, 10}, {yp, -20, 20, 10}], 3];
Length[pos]
ffr[xx0_, yy0_, zz0_, \[Alpha]_] :=
Sum[(Re[fray]) /. {x -> xx0 + 1*^-9 xx, y -> yy0 + 1*^-9 yy,
z -> zz0 + 1*^-9 pos[[i, 3]], rad -> 1*^-9 ract}) /. {xx ->
Cos[\[Alpha] pos[[i, 1]] - Sin[\[Alpha] pos[[i, 2]],
yy -> Cos[\[Alpha] pos[[i, 2]] + Sin[\[Alpha] pos[[i, 1]]}, {i,
Length[pos]}]
tz[xx0_, yy0_, zz0_, \[Alpha]_] :=
Sum[(Cross[{x - xx0, y - yy0, 0}, Re[fray]]][[3]] /. {x ->
xx0 + 1*^-9 xx, y -> yy0 + 1*^-9 yy,
z -> zz0 + 1*^-9 pos[[i, 3]], rad -> 1*^-9 ract}) /. {
xx -> Cos[\[Alpha] pos[[i, 1]] - Sin[\[Alpha] pos[[i, 2]],
yy -> Cos[\[Alpha] pos[[i, 2]] + Sin[\[Alpha] pos[[i, 1]]}, {i,
Length[pos]}]
ffr[1*^-6, 0, 0, 0]
ffr[1*^-6, 0, 0, \[Pi]/2]
ffg[xx0_, yy0_, zz0_, \[Alpha]_] :=
Sum[(Re[(fsc + fgr)] /. {x -> xx0 + 1*^-9 xx,

```

```

y -> yy0 + 1*^-9 yy, z -> zz0 + 1*^-9 pos[[i, 3]],
rad -> 1*^-9 ract}) /. {xx ->
Cos\[Alpha] pos[[i, 1]] - Sin\[Alpha] pos[[i, 2]],
yy -> Cos\[Alpha] pos[[i, 2]] + Sin\[Alpha] pos[[i, 1]]}, {i,
Length[pos]}]
ffg[1*^-6, 0, 0, 0]
ffg[1*^-6, 0, 0, \[Pi]/2]
alpha = \[Pi];
rrr = 0.5;
rot1 =
Table[px = rrr w0x Cos\[Tau];
py = rrr w0y Sin\[Tau];
root =
FindRoot[tz[px, py, 0, \[Alpha]], {\[Alpha], alpha, 1.01 alpha}];
alpha = \[Alpha] /. root // Chop;
Print{\[Tau]/Degree, alpha/Degree};
{px, py, alpha}, {\[Tau], 0., 2 \[Pi], \[Pi]/30};
ParametricPlot[{w0x Cos\[Tau], w0y Sin\[Tau]}, {\[Tau], 0,
2 \[Pi]}, AspectRatio -> Automatic,
PlotRange -> {.25 {-w0x, w0x}, 12 {-w0y, w0y}},
Epilog -> {Table[{GrayLevel[0], Point[rot1[[i, {1, 2}]]], Hue[1],
AbsoluteThickness[2],
Line[{rot1[[i, {1, 2}]],
rot1[[i, {1, 2}]] +
2*^-6 {Cos[rot1[[i, 3]], Sin[rot1[[i, 3]]]}}, {i,
Length[rot1]}]};
ContourPlot[
Abs[u0^2 /. {z -> 0, x -> 1*^-6 xx,
y -> 1*^-6 yy}], {xx, -0.15 w0x 1*^-6,
0.15 w0x 1*^-6}, {yy, -2 w0y 1*^-6, 2 w0y 1*^-6},
AspectRatio -> Automatic,
Epilog -> {Table[{Hue[5], Point[1*^-6 rot1[[i, {1, 2}]]], Hue[1],
AbsoluteThickness[3],
Line[{1*^-6 rot1[[i, {1, 2}]],
1*^-6 rot1[[i, {1, 2}]] +
1*^-6*2*^-6 {Cos[rot1[[i, 3]], Sin[rot1[[i, 3]]]}}, {i,

```

```
Length[rot1]]];
```

Potential calculation for line profile

```
n0 = 1.33;
n1 = 1.59;
w0x = 45*^-6/2;
w0y = 0.5*^-6;
mu0 = 4 \[Pi] 1*^-7;
epsilon0 = 8.854187817*^-12;
lam = 1064*^-9;
k0 = 2 \[Pi]/lam;
p0 = 0.07;
zrx = n0 k0 w0x^2/2;
zry = n0 k0 w0y^2/2;
amp = Sqrt[4*p0/\[Pi]/w0x/w0y*Sqrt[mu0/epsilon0]/n0];
u0 := amp*Exp[-I*n0*k0*(z)]*Sqrt[(I*zrx/(z + I*zrx))]
Sqrt[(I*zry/(z + I*zry))]
Exp[-I*n0*k0*((x)^2/2/(z + I*zrx) + (y)^2/2/(z + I*zry))];
uv = {0, u0, 0};
e0 = 1/n0^2/k0^2*Grad[Div[uv]] + uv;
h0 = I/k0 Curl[uv] Sqrt[epsilon0/mu0];
e0 = {0, u0, 0};
h0 = n0 {-u0, 0, 0} Sqrt[epsilon0/mu0];
poi = 1/2 Re[Cross[e0, Conjugate[h0]]] // Chop;
aa0 = 4 \[Pi] rad^3 (n1^2 - n0^2)/(n1^2 + 2 n0^2);
aa = aa0/(1 + 2/3 I n0^3 k0^3 aa0/(4 \[Pi]));
cscat = n0^4 k0^4/6/\[Pi]*Abs[aa]^2;
cabs = n0 k0 Im[aa0];
fsc = (cscat + cabs) n0 Sqrt[epsilon0 mu0] poi;
fgr = 1/4 epsilon0 n0^2 Re[
aa] 2 Re[{e0.Conjugate[D[e0, x]], e0.Conjugate[D[e0, y]],
e0.Conjugate[D[e0, z]]}];
fray = epsilon0 n0^2/2 Re[
aa {e0.Conjugate[D[e0, x]], e0.Conjugate[D[e0, y]],
e0.Conjugate[D[e0, z]]}];
```

```

ract = 3;
hact = 37./7;
act = \[Pi]/7.;
dact = 2.7;
act0 = 0;
pos = Flatten[
Table[{{i hact, xp + dact Cos[act0 + i act],
yp + dact Sin[act0 + i act]}, {(i + 1/2) hact,
xp + dact Cos[act0 + i act + \[Pi]],
yp + dact Sin[act0 + i act + \[Pi]]}}, {i, 0, 378,
1}, {xp, -20, 20, 10}, {yp, -20, 20, 10}], 3];
Length[pos]
potential = epsilon0 n0^2/2 Re[aa *(e0.Conjugate[e0])];
ppr[xx0_, yy0_, zz0_, \[Alpha]_] := Sum[(Re[(potential)
/. {x -> xx0 + 1*^-9 xx, y -> yy0 + 1*^-9 yy, z -> zz0
+ 1*^-9 pos[[i, 3]], rad -> 1*^-9 ract}) /. {xx ->
Cos[\[Alpha] pos[[i, 1]] - Sin[\[Alpha] pos[[i, 2]],
yy -> Cos[\[Alpha] pos[[i, 2]] + Sin[\[Alpha] pos[[i, 1]]}
, {i, Length[pos]}
Plot[ ppr[w0x, w0y, 0,
\[Alpha] ^], {\[Alpha], 0, 360}, Frame -> True,
PlotRange -> All, BaseStyle -> {FontWeight -> "Bold",
FontSize -> 16}]

```

Potential calculation for Gaussian profile

```

n0 = 1.33;
n1 = 1.59;
w0x = 0.75*^-6;
w0y = 0.75*^-6;
mu0 = 4 \[Pi] 1*^-7;
epsilon0 = 8.854187817*^-12;
lam = 1064*^-9;
k0 = 2 \[Pi]/lam;
p0 = 0.02;
zrx = n0 k0 w0x^2/2;

```

```

zry = n0 k0 w0y^2/2;
amp = Sqrt[4*p0/\[Pi]/w0x/w0y*Sqrt[mu0/epsilon0]/n0];
u0 := amp*Exp[-I*n0*k0*(z)]*Sqrt[(I*zrx/(z + I*zrx))]
Sqrt[(I*zry/(z + I*zry))*
Exp[-I*n0*k0*((x)^2/2/(z + I*zrx) + (y)^2/2/(z + I*zry))];
uv = {0, u0, 0};
e0 = 1/n0^2/k0^2*Grad[Div[uv]] + uv;
h0 = I/k0 Curl[uv] Sqrt[epsilon0/mu0];
e0 = {0, u0, 0};
h0 = n0 {-u0, 0, 0} Sqrt[epsilon0/mu0];
poi = 1/2 Re[Cross[e0, Conjugate[h0]]] // Chop;
aa0 = 4 \[Pi] rad^3 (n1^2 - n0^2)/(n1^2 + 2 n0^2);
aa = aa0/(1 + 2/3 I n0^3 k0^3 aa0/(4 \[Pi]));
cscat = n0^4 k0^4/6/\[Pi]*Abs[aa]^2;
cabs = n0 k0 Im[aa0];
fsc = (cscat + cabs) n0 Sqrt[epsilon0 mu0] poi;
fgr = 1/4 epsilon0 n0^2 Re[
aa] 2 Re[{e0.Conjugate[D[e0, x]], e0.Conjugate[D[e0, y]],
e0.Conjugate[D[e0, z]]}];
fray = epsilon0 n0^2/2 Re[
aa {e0.Conjugate[D[e0, x]], e0.Conjugate[D[e0, y]],
e0.Conjugate[D[e0, z]]}];
ract = 3;
hact = 37./7;
act = \[Pi]/7.;
dact = 2.7;
act0 = 0;
pos = Flatten[
Table[{{i hact, xp + dact Cos[act0 + i act],
yp + dact Sin[act0 + i act]}, {(i + 1/2) hact,
xp + dact Cos[act0 + i act + \[Pi]],
yp + dact Sin[act0 + i act + \[Pi]]}}, {i, 0, 378,
1}, {xp, -20, 20, 10}, {yp, -20, 20, 10}], 3];
Length[pos]
potential = epsilon0 n0^2/2 Re[aa *(e0.Conjugate[e0])];
ppr[xx_, yy_, zz_, \[Alpha_] := Sum[(Re[potential]

```

```
/. {x -> xx0 + 1*^-9 xx, y -> yy0 + 1*^-9 yy, z -> zz0
+ 1*^-9 pos[[i, 3]], rad -> 1*^-9 rad} /. {xx ->
Cos[\[Alpha] pos[[i, 1]] - Sin[\[Alpha] pos[[i, 2]],
yy -> Cos[\[Alpha] pos[[i, 2]] + Sin[\[Alpha] pos[[i, 1]]}
, {i, Length[pos]}
Plot[ ppr[w0x, w0y, 0,
\[Alpha] °], {\[Alpha], 0, 360}, Frame -> True,
PlotRange -> All, BaseStyle -> {FontWeight -> "Bold", FontSize -> 16}]
```